Splashing drops

Marise Gielen

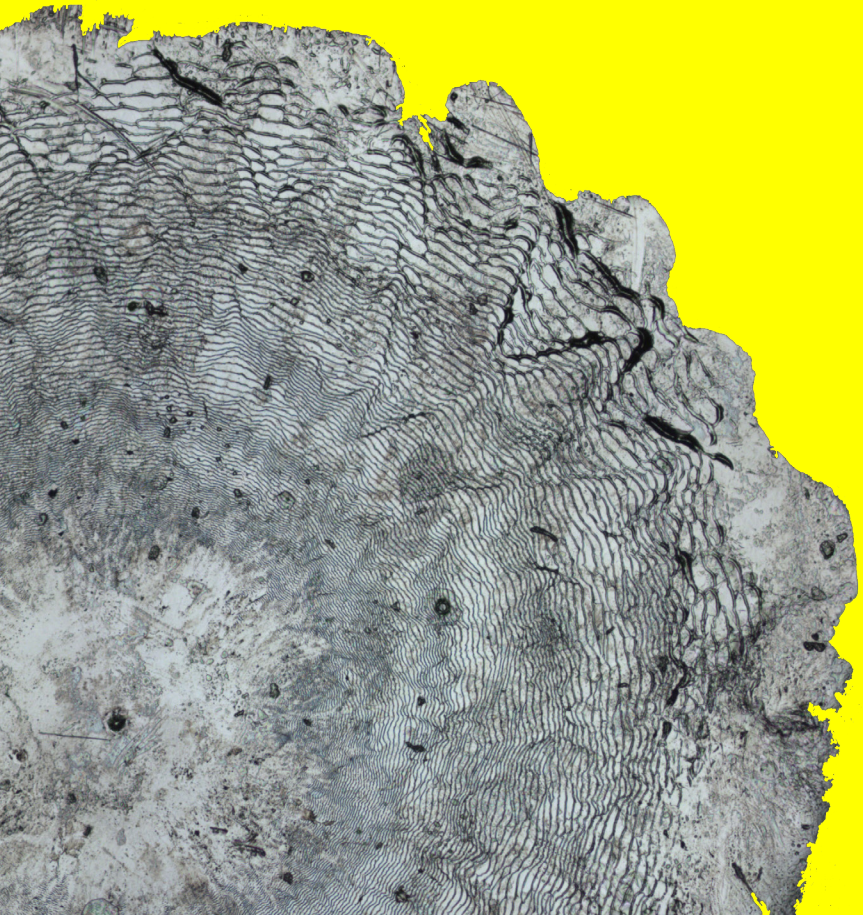

Splashing drops

Marise Vera Gielen

PROMOTIE COMMISSIE:

Prof. dr. ir. Hans Hilgenkamp (voorzitter)	Universiteit Twente
Prof. dr. ir. Jacco H. Snoeijer (promotor)	Universiteit Twente Technische Universiteit Eindhoven
Prof. dr. rer. nat. Detlef Lohse (promotor)	Universiteit Twente
Dr. ir. Hanneke Gelderblom (co-promotor)	Universiteit Twente
Prof. dr. ir. Cees H. Venner	Universiteit Twente
Prof. dr. Serge G. Lemay	Universiteit Twente
Prof. dr.-ing. Cameron Tropea	Technische Universität Darmstadt
Prof. dr. Anton A. Darhuber	Technische Universiteit Eindhoven
Ir. Michel Riepen	ASML

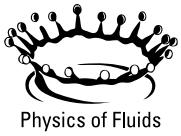

UNIVERSITY OF TWENTE.

The work in this thesis was carried out at the Physics of Fluids group of the Faculty of Science and Technology of the University of Twente. This work is part of an Industrial Partnership Program of the Netherlands Organization for Scientific Research (NWO). This research program is co-financed by ASML.

Nederlandse titel:
Uiteenspattende druppels

Publisher:
Marise Vera Gielen, Physics of Fluids, University of Twente,
P.O. Box 217, 7500 AE Enschede, The Netherlands
pof.tnw.utwente.nl

ISBN: 978-90-365-4495-5
DOI: 10.3990/1.9789036544955

SPLASHING DROPS

PROEFSCHRIFT

ter verkrijging van
de graad van doctor aan de Universiteit Twente,
op gezag van de rector magnificus,
prof. dr. T. T. M. Palstra,
volgens besluit van het College voor Promoties
in het openbaar te verdedigen
op vrijdag 6 april 2018 om 12.45 uur

door

Marise Vera Gielen
geboren op 18 januari 1989
te Eindhoven

Dit proefschrift is goedgekeurd door de promotoren

Prof. dr. ir. Jacco H. Snoeijer

en

Prof. dr. rer. nat. Detlef Lohse

en de co-promotor

Dr. ir. Hanneke Gelderblom

Contents

1 Introduction

Looking outside on a rainy day reveals some of the fascinating aspects of drop impact. Due to wind, rain drops may be blown against the windows and move downwards after contact with the window. When a raindrop impacts onto a puddle, one might observe small secondary droplets breaking off after impact. Leafs of trees and plants also feel the impact of a raindrop, causing the position of the leaf to move under the influence of the force applied by the impacting drop. These are examples of natural drop impacts, but also in industrial applications drop impacts are omnipresent. One of these industrial applications of drop impact which occurs in the nanolithography machines produced by ASML The Netherlands B.V., is the motivation of the work done in this thesis.

In 1876, Worthington [1] made the first advances in revealing the different stages of drop impact, as shown in Fig. 1.1. Here, observations by eye of a boiled milk drop impacting onto a smoked glass substrate are sketched. To visualize the different stages of drop impact, a flash light was used to illuminate the impacting drop for a short time. It is already observed that fingers form at the edges of the drop (I-IV) and that the drop may eject small secondary droplets (II and III). At later stages in time, the drop may recede (V and VI). Since these first advances, high speed imaging is further developed [2], resulting in numerous studies of the intriguing aspects of drop impact, such as bouncing, deposition and splashing. This high speed imaging makes the study of drop impact a relatively new field in fluid dynamics.

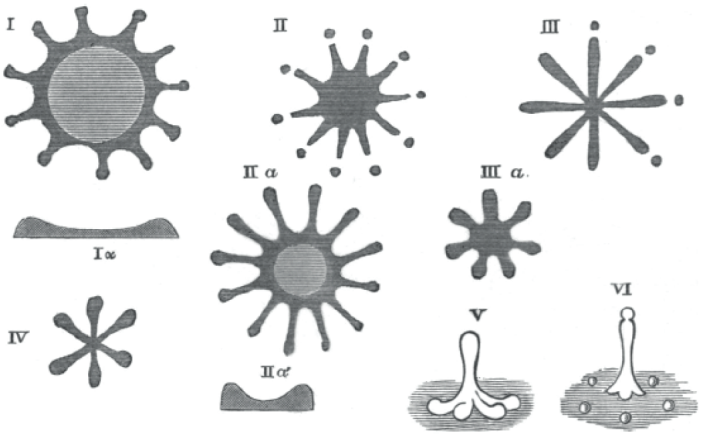

Figure 1.1: Sketches of the impact behavior of a 6-mm boiled milk drop impacting onto a smoked glass substrate as observed by Worthington [1] in 1876. The drop is generated 100 mm above the substrate. During impact, the formation of fingers is observed in I-IV. Next to that, at some impact events (II and III), small secondary droplets break off from these fingers. At later times, the drop is collecting again (IV), and it comes off the substrate (V), leaving behind some small droplets (VI).

1.1 Drop impact

Drop impact is influenced by many parameters. Properties of the drop that influence the impact event are its impact velocity U, diameter D, impact angle α, surface tension γ, kinematic viscosity ν, and density ρ. Most of these drop properties are captured by the dimensionless Weber number $\mathrm{We} = \rho D U^2/\gamma$, which is the ratio of kinetic and surface energy, and Reynolds number $\mathrm{Re} = DU/\nu$, giving the ratio of fluid inertia and viscous forces. In addition, the substrate properties such as the roughness or structures on the substrate, the wettability, the elasticity, or thickness of a liquid film coating the substrate are of importance. Next to the drop and substrate properties, the properties of the surrounding air play an important role in the outcome of a drop impact events, via the pressure or the viscosity of the surrounding air. All of these factors together determine what happens when a drop impacts a substrate: (partial) bouncing, deposition or splashing. These different outcomes are described in the following sections, and are shown in Fig. 1.2.

1.1.1 Bouncing

One of the possible outcomes of drop impact is that the drop spreads out over the substrate. When the maximum spreading is reached, the drop retracts and lifts off

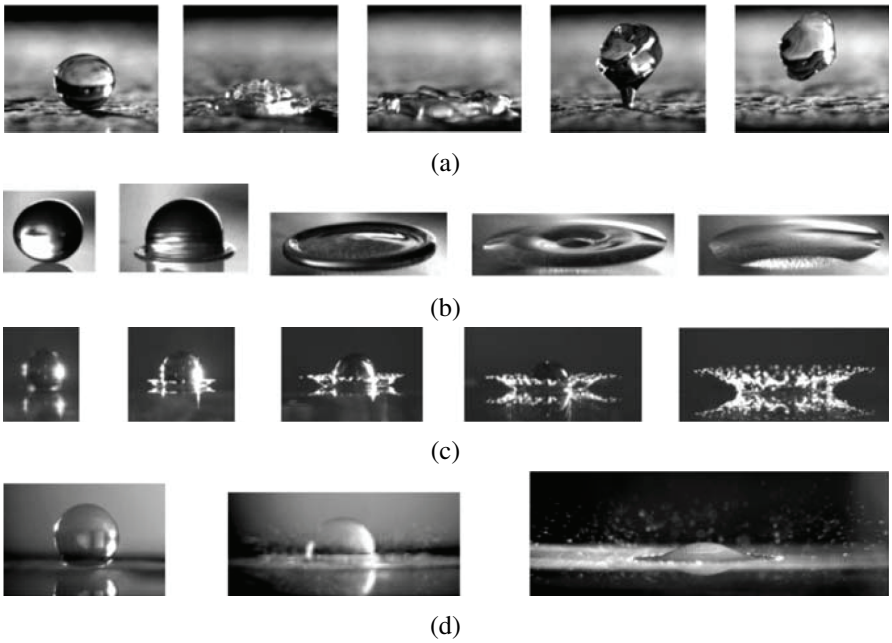

Figure 1.2: Different outcomes of a drop impact events. Generally speaking, the kinetic energy of the impacting drop increases from (a) to (c), but a change of properties of the drop, substrate, and surrounding may also lead to a different outcome. (a) Bouncing: After impact the drop spreads over the substrate. The spreading stops when surface tension forces overcome the inertia of the drop. After maximal spreading, the drop retracts. When this retraction goes fast enough, the drop may lift off the substrate. (b) Deposition: After impact the drop spreads over the substrate. At maximal spreading the drop sticks to the substrate and remains deposited on the substrate. (c) Corona splashing: After impact the spreading lamella (with ligaments) of the drop lift off from the substrate. The lamella moves outwards with a high velocity. When this outwards velocity is high enough surface tension is unable to retract the drop and the ends of the lamella break up into small secondary droplets. (d) Prompt splashing: Secondary droplets detach parallel to the substrate during the early stages of impact, when the lamella expands with high velocity. Again, surface tension is not able to keep the drop together, resulting in the secondary splashed droplets. Images are taken from Ref. [3], experiments are done by Ref. [4].

from the substrate, as shown in Fig. 1.2(a). This behavior is called bouncing. The entire drop can bounce off the substrate, or part of the drop bounces back, the latter being referred to as partial bounce. Drop bouncing is observed for low impact We, but the exact value of We depends on substrate properties.

A bounce occurs when the drop spreads much further than expected given its static receding contact angle. This large drop spread causes the drop to retract, which can lead to rebound [4]. Another mechanism for bouncing is that the drop is cushioned by a thin air layer that is trapped between the substrate and the drop [5]. This air layer prevents contact between the drop and the substrate. Therefore the drop retracts to minimize its surface energy. To prevent contact of the drop and the substrate, one often uses super hydrophobic or structured substrates [6]. However, the air layer can also remain intact on a hydrophilic substrate or even on a liquid pool [7]. In all these cases bouncing is observed.

Once the drop bounces off the substrate, it falls back due to gravity and impact again. This secondary impact occurs with lower impact velocity and hence lower We, because of energy losses in the bouncing process [5, 8]. This energy loss is minimal on rigid substrates [5, 8], while it is much higher on a liquid pool due to additional energy dissipation in the pool [7]. The time it takes for a drop to bounce is independent of the impact velocity, but increases with increasing drop radius [7, 9].

1.1.2 Deposition

For larger We, the air layer in between the drop and the substrate is squeezed out and the drop makes contact with the substrate during its spreading. This contact prevents bouncing, therefore the drop is deposited: it remains as whole into contact with the substrate (Fig. 1.2(b)). After contact with the substrate is made, the drop deforms to a flat shape and a spherical rim is formed at the outer edges of the drop. Over time, this rim distributes evenly over the thin splat, where the final splat size depends on the wettability of the substrate.

The spreading of the drop over the substrate occurs in different stages [10]. Shortly after impact in the kinematic phase the drop spreading over time scales with $t^{1/2}$. An ejection sheet is created which grows in time. At later times the spreading slows down and a thicker rim at the outer edges is formed. These phenomena depend on We, Re, the contact angle with the substrate θ and time. In the relaxation phase the drop may begin to recede, and it finally ends up in a equilibrium phase where the drop has reached its final shape.

Next to the spreading dynamics, the maximum spreading of an impacting drop has been studied. The maximum spreading depends on the drop's kinetic impact energy, its surface energy and the viscous dissipation [11, 12]. The general expression for the

maximum spreading diameter derived in Ref. [12] reads:

$$\xi_{max} = \frac{D_{max}}{D} = \frac{P^{1/2}}{A + P^{1/2}} \mathrm{Re}^{1/5}, \tag{1.1}$$

with $P = \mathrm{WeRe}^{-2/5}$ and $A = 1.24$ a fitting constant. For low Re, in the limit where the spreading depends solely on viscous dissipation, a scaling of the maximum spreading with $\mathrm{Re}^{1/5}$ is found [13]. In the capillary regime, where viscous dissipation is negligible (high Re), energy conservation predicts a scaling of D_{max} with $\mathrm{We}^{1/2}$ [14].

In all scaling arguments, only the drop properties are taken into account, expressed by We and Re. In addition, the spreading is influenced by properties of the substrate. On superheated substrates for example, the maximum spreading is different than expected from theory, which might be due to the additional vapor layer generated from the drop itself [15]. Chemicallicy structured substrates can enhance spreading in one direction and limit spreading in the other direction [16, 17]. The contact angle of the drop on the substrate also determines the spreading of the drop, such that an increase in contact angle causes a decrease of maximum spreading [18].

1.1.3 Splashing

The break off of small secondary droplets, which is called splashing, may be oberved when We is further increased. An example of so-called corona splashing is shown in Fig. 1.2(c). Here, a rim has formed that is moving upwards from the impact location and secondary droplets detach at the end of this rim. Another way of splashing is prompt splashing (Fig. 1.2(d)). This splash occurs earlier in time and secondary droplets break off from the fast moving ejecta sheet at the contact line. Describing the splashing threshold is very complex as it depends on many conditions.

Many studies focused on the transition from deposition to splashing and the determination of a splashing threshold. This threshold is influenced by properties of the drop expressed in We and Re, but also by the properties of the surrounding air and the substrate. When a drop impacts under an angle, the splash becomes asymmetric and splashing is suppressed in specific directions [19–22]. Surprisingly, the transition to both the prompt and corona splash can be forced to higher We by reducing the pressure of the surrounding air [23, 24].

The properties of the substrate also have an important influence on the transition to splashing. Whether a drop impacts onto a rigid substrate, a thin film or a deep pool lead to a different outcome of the impact, such as a different splashing threshold [25–27] or crown formation [28]. Other properties such as roughness or substrate structure [23, 29] can also be used to increase the transition to splashing (in a specific direction), while wettability [30] does not influence the splashing transition. Splashing is suppressed when the substrate is deformable, such as on viscoelastic substrates [31] or elastic membranes [32]. The temperature of the substrate can alter the transition

to splashing both when the substrate is (well) above the boiling temperature of the drop [33] and when the substrate is (well) below the melting temperature of the drop [34–39].

It is now clear that many parameters influence the transition to splashing, but so far only observations are mentioned. In Sec. 1.2 the different criteria to obtain splashing are discussed in more detail.

1.2 Splashing criteria

The starting point of all splashing criteria is that the drop needs a minimal impact velocity to splash. However, different theories exist on what causes a drop to splash when this minimal impact velocity is exceeded. Below we first discuss drop-substrate interaction followed by the role of the surrounding air. Lastly, it is discussed how also the substrate temperature may trigger drop splashing.

1.2.1 The role of drop-substrate interaction

The most commonly used splashing criterion is based on the idea that the crown of the drop needs a minimal velocity to overcome the retracting surface tension forces, making the crown break up into small secondary droplets [40, 41]. This minimal velocity is called the Taylor-Culick velocity $V_{TC} = \sqrt{\gamma/\rho e}$, with e the thickness of the crown at ejection. V_{TC} balances the surface tension forces trying to keep the drop together and the acceleration forces of the crown moving outwards [42]. The velocity of the crown V is calculated from volume conservation, where it is assumed that the volume of the drop is completely distributed over the crown [41]:

$$D^2U \sim DeV, \tag{1.2}$$

It has experimentally been shown that $e \sim \sqrt{\nu t}$, with t the time after impact [43].

The minimal velocity the crown needs to have to overcome the surface tension forces is $V > V_{TC}$, which is the splashing criterion. Using, the typical impact time scale $t \sim D/U$ in Eq. (1.2) we then obtain the splashing criterion

$$\frac{V}{V_{TC}} \sim \mathrm{We}^{1/2}\mathrm{Re}^{1/4} > K, \tag{1.3}$$

with K the critical number for splashing. Previous studies reported $K \approx 54$ for a rigid surface [25], $K \approx 160$ for a thin liquid film [26], and $K \approx 90$ for a deep liquid pool [27].

In Eq. (1.3) the properties of the substrate and of the surroundings are not taken into account which explains the different values found for K. In practice, for each different substrate or surrounding parameters the value of K has to be determined experimentally.

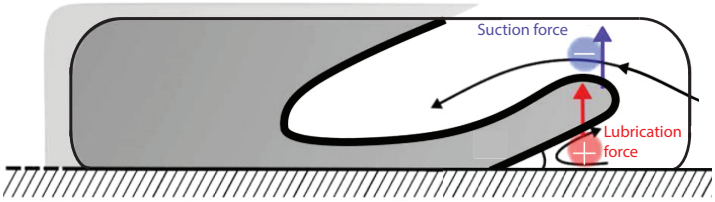

Figure 1.3: Schematic view of the forces exerted onto the ejecta sheet. As long as the ejecta sheet does not touch the substrate again, splashing might be observed. A lubrication force pushes the ejecta sheet upwards away from the substrate due to an overpressure below the ejecta sheet. There is an under pressure above the ejecta sheet resulting in a suction force that pulls on the ejecta sheet to lift it further. The black arrow shows the motion of the air during the growth of the ejecta sheet. Image adapted from Ref. [44].

1.2.2 The role of the surrounding air

A more recent criterion [44] takes the role of the surrounding air into account. To obtain splashing, it states that the ejecta sheet should detach from the substrate, as schematically shown in Fig. 1.3. This condition implies that there should be a sufficient vertical lift force acting onto the ejecta sheet to prevent touchdown. Once the ejecta sheet has detached from the substrate, its edge should not contact the substrate again. Thus, the velocity at which the ejecta sheet moves upwards has to be larger than the growth rate of the rim at the end of the ejecta sheet to prevent touchdown.

Given the importance of this criterion, let us briefly recall the key steps of the analysis of [44]. The sheet that forms the ejecta sheet can only be ejected if the tip of the sheet moves outwards faster than the wetted base area. From a momentum balance, the critical dimensionless time at which the sheet is ejected $t_{e,c} = \tilde{t_c}/(D/U_c)$ is calculated:

$$c_1 \mathrm{Re}_c^{-1} t_{e,c}^{-1/2} + \mathrm{We}_c^{-1} = c^2 t_{e,c}^{3/2}, \tag{1.4}$$

with $c_1 = \sqrt{3}/2$ and $c = 1.1$ are fitting parameters and the subscript c denotes the parameter at the splashing threshold. In the limit of high We we find $t_{e,c} \sim \mathrm{Re}^{-1/2}$, while $t_{e,c} \sim \mathrm{We}^{-2/3}$ for low We.

Once the sheet is ejected the vertical lift force ℓ can be calculated. ℓ consists of two contributions that are illustrated in Fig. 1.3: (i) the lubrication force exerted in the wedge between the substrate and the ejecta sheet and (ii) the suction force exerted at the top part of the ejecta sheet. The overpressure in the wedge dominates over the suction force, which gives $\ell \sim \mu_g V_t$, with μ_g the dynamic viscosity of the air and $V_t \sim U t_{e,c}^{-1/2}$ the radial velocity of the ejecta sheet. Once the lift force is known, the vertical force balance $\rho H_t^2 \dot{V}_v \sim \ell$ can be solved to find an expression for the vertical

tip velocity

$$V_v \sim \sqrt{\frac{\ell}{\rho H_t}}, \tag{1.5}$$

with H_t the thickness of the tip of the ejecta sheet. For the ejecta sheet not to contact the substrate again, the vertical tip velocity has to be larger than the growth rate of the rim at the tip of the ejecta sheet $V_v > \dot{H}_t$. The growth rate of the rim is found to scale as

$$\dot{H}_t \sim V_{TC} \sim \sqrt{\gamma/\rho H_t}. \tag{1.6}$$

To obtain a large enough lift force at the tip of the ejecta sheet to prevent touchdown $V_v > V_{TC}$ which gives

$$\frac{\mu_g U}{\gamma} t_{e,c}^{-1/2} = C, \tag{1.7}$$

where C is the critical number for splashing. Substrate properties such as roughness or (chemical) patterning of the substrate however are not known a priori and are captured in C, which again has to be determined experimentally for each substrate. For substrate temperatures up to the Leidenfrost temperature of the impacting drop, temperature dependent liquid and gas properties can be used in the non-simplified version of Eq. (1.7). In this way the increase of splashing threshold with substrate temperature (up to the Leidenfrost temperature) has been explained [33].

In the limit of high We Eq. (1.7) can be rewritten into the form of Eq. (1.3) to show the difference between both criteria:

$$\frac{\mu_g U}{\gamma} t_e^{-1/2} = \mathrm{We}^{1/2}\mathrm{Re}^{1/4}\sqrt{\frac{\mu_g^2}{\rho\gamma D}} > C. \tag{1.8}$$

From the differences between Eqs. (1.3) and (1.8) one concludes that K is modified not only by properties of the surrounding air, but also by properties of the impacting drop. This difference illustrates the underlying fundamental difference in the physical mechanism for splashing.

1.2.3 The role of temperature changes in the drop

The temperature of the substrate gives a third criterion for drop splashing. When the temperature of the substrate is (well) above the boiling point of the drop, Leidenfrost splashing may occur [33]. On the other hand, if the substrate temperature is (well) below the melting point of the drop it may trigger freezing induced splashing [34–39].

At the Leidenfrost temperature, a sudden decrease in splashing threshold is found [33]. This decrease shows that when the drop contacts the substrate (below the Leidenfrost temperature) it is harder to splash compared to when the drop does not contact the substrate, which is the case above the Leidenfrost temperature. Above

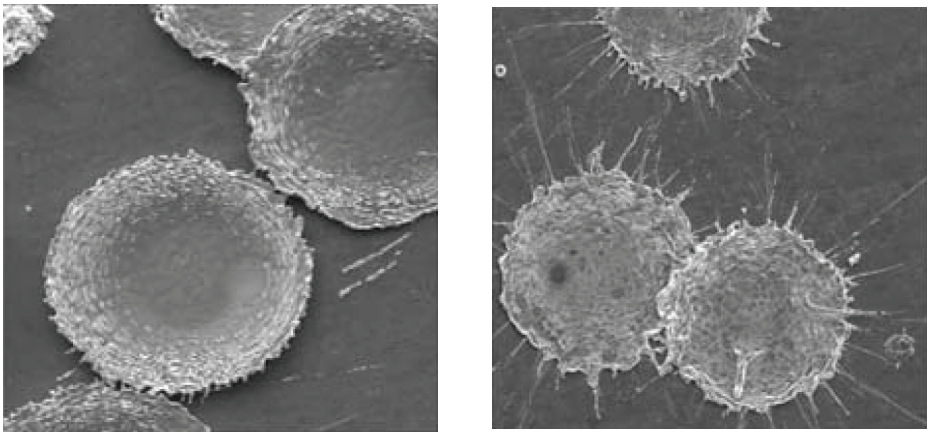

(a) (b)

Figure 1.4: Splats left by plasma-sprayed nickel drops after impact onto a steel substrate. The transition from liquid to solid for nickel is at 1455°C. (a) After impact onto a substrate with temperature 400°C a circular splat is formed. (b) Impact onto a substrate of 640°C results in fingers at the outer radius of the drop. These fingers represent instabilities during the impact, from which secondary droplets are ejected. Images are taken from Ref. [34], experiments are performed by [36].

the Leidenfrost temperature, only a slight increase in splashing threshold is found with increasing temperature. However, all studies [33, 45, 46] show a different weak temperature dependence in the splashing threshold. Therefore it is concluded that We and substrate temperature are not the only relevant parameters controlling the splashing behavior.

When a substrate is at a temperature at or below the melting point of the drop, the drop cools down during the impact and ultimately solidifies. The final shape of the solidified splat depends on substrate temperature, as shown in Fig. 1.4 for plasma-sprayed nickel drops. The amount of solidification depends on the substrate temperature, the impact velocity of the drop and thermal properties of both substrate and drop, such as latent heat, thermal conductivity, liquid melting temperature and thermal diffusivity. When part of the drop is solidified, it may obstruct the outward flowing liquid of the impacting drop and therefore trigger drop splashing. This phenomenon is called freezing-induced splashing [34–39]. Since it is difficult to generate drops that freeze fast enough to study the freezing induced splashing at controlled size and velocity, a systematic study of this transition to splashing is lacking.

1.3 Drop splashing in nanolithography

In most applications, such as ink-jet printing [47, 48], (metal) spray coating [49] or pesticide delivery [50], splashing is an unwanted side-effect that reduces the efficiency of the process. Therefore, it is of utmost importance to understand the conditions for drop splashing and to find ways to prevent it. The work described in this thesis has emerged from drop impact events in nanolithography machines in the extreme ultraviolet (EUV) light source. ASML The Netherlands B.V. is market leader in the production of these machines and wants to enhance the machine's efficiency and durability. One way of increasing this efficiency is to reduce the contamination from liquid debris in the machine by suppressing drop splashing after impact onto hardware, as we explain below.

The liquid debris is generated during the production of the EUV light, as shown schematically in Fig. 1.5. EUV light is emitted by a tin plasma that is generated in the source chamber by shooting onto a liquid tin drop with a pulsed laser, as shown in Fig. 1.5(b). The process consists of two steps: (i) A first laser pulse deforms the drop (Fig 1.5(c)) [51], such that the conversion efficiency (ratio of amount of laser power to EUV power) increases. (ii) With a second laser pulse the liquid tin can be converted into plasma. However, during both laser pulse impacts small high-velocity droplets break off from the main drop. These droplets are not converted into plasma but are expelled towards the hardware of the source chamber. This process leads to the generation of of tin debris and contaminates various places in the machine. Some of these drops are directed towards the collector mirror (Fig. 1.5(a)), where they limit the reflecting efficiency and lifetime of the mirror. Other drops are directed towards surfaces above the collector mirror. Impact onto most of these parts is harmless, as long as the drop remains attached to that surface. However, when splashing occurs small secondary droplets are ejected in multiple directions and they may contaminate the collector mirror when they impact again. It is therefore of key importance to suppress drop splashing at these surfaces in the source chamber.

There are also secondary sources of tin debris, which we describe briefly. When previous drops have impacted onto a hot surface at the side walls, they may form a liquid film at these surfaces. Next to the fact that these liquid films alter the impact behavior of the drops, they may also form another source of drop debris. If this liquid surface is at the ceiling of the hardware, a Rayleigh-Taylor instability may grow when surface tension forces are not able to overcome gravity forces [55, 56] and drops detach under influence of gravity. These are relatively large, slow drops with a size in the millimeter range and an impact velocity of meters per second and are directed towards the bottom of the source chamber.

Liquid films are also a source of other small drops. These drops are generated by a process called *spitting*: Hydrogen radicals in the liquid tin layer lead to bubble formation. These bubbles rise to the surface and burst, thereby ejection tiny droplets.

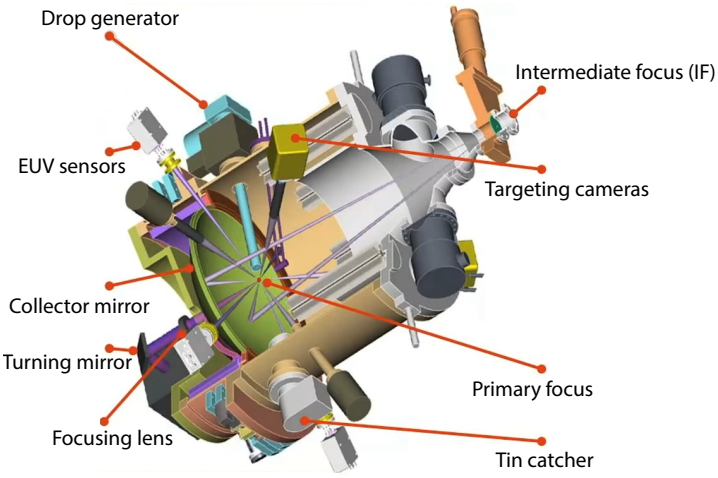

(a)

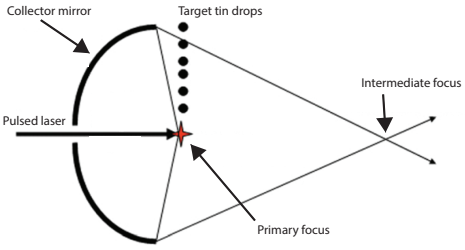

(b)

(c)

Figure 1.5: (a) Liquid tin drops are produced by the drop generator and enter the source chamber. In the EUV source chamber, the tin drops are hit by two laser pulses at the primary focus in order to create the EUV light out of the liquid tin drop. The EUV light is then collected by the collector mirror and focused at the intermediate focus (IF), before it continues to the illumination optics for lithography. During the conversion from tin to plasma by the laser pulses, tin debris remains in the source chamber. These small, fast liquid tin drops impact onto side walls of the source chamber, where splashing and further contamination are limiting the performance of the EUV source. Image adapted from Ref. [52]. (b) Simplified sketch of the source chamber. The red star indicates the main source of the tin debris. Image adapted from Ref. [53]. (c) Drop deformation after the impact of a laser pulse. Small secondary droplets are ejected in all directions from the main drop, resulting in tin debris inside the EUV chamber. Image taken from Ref. [54].

However, the presence of the hydrogen radicals is crucial for the in situ cleaning of the collector mirror [57] to maximize the running time of the EUV source.

Some of the original high-velocity drops are missed by the laser pulse and continue their path into the tin catcher (Fig. 1.5(a)). Here, the drops are trapped into a liquid pool and disposed away. During impact onto this pool, drop splashing may occur and the splashed droplets might contaminate construction parts. Another possibility is that a drop is slightly bend off the desired path and therefore misses the liquid pool. Preventing splashing of these drops is also important to increase the performance of the EUV source.

In summary, there are multiple sources generating tin drops of different sizes and velocities that impact onto the hardware of the EUV source. This hardware consists of different types of material and is kept at different temperatures depending on its functioning which leads to a variety of drop impact conditions. Next to that, the angle at which the drops arrive also varies, since the drops are produced at multiple locations in the source. Therefore, the goal of this thesis is to study how properties of a substrate, in particular orientation, temperature and elasticity, influence the splashing behavior of the impacting drops. Once this influence is known, the hardware can be adapted to minimize drop splashing after impact.

1.4 Dimensionless numbers

The tin drops that cause the contamination in the source have different origins and therefore different velocities and sizes. To generate and visualize most of these drops in a controlled way is out of reach, since they either are too small and/or go too fast for conventional drop-on-demand systems. For this reason, we focus in this thesis on a number of specific aspects of drop impact, and take advantage of the powerful method of dimensional analysis. The motivation for the dimensional analysis is that it allows for the study of an upscaled version of the tin drops that is better accessible with imaging techniques. Moreover, it allows in certain cases to replace tin by water which has many practical advantages.

The dimensionless numbers that are important in the EUV source chamber are determined from the Buckingham-π-theorem [58]. The number of independent dimensionless groups equals the the number of important variables minus the number of physical dimensions of which these variables consist. The nine important variables in the EUV source chamber are the liquid's kinematic viscosity ν, density ρ, surface tension γ, specific heat c_p, temperature difference between melting temperature and substrate temperature ΔT, latent heat for solidification L, thermal diffusivity κ, diameter D and impact velocity U. The four physical dimensions of the variables are length, mass, time and temperature. From this simple analysis, we find that we need five dimensionless groups to describe the drop impact phenomena in the source chamber.

With foreknowledge we construct these dimensionless groups in such a way we find well-known dimensionless numbers:

The Reynolds number

$$\mathrm{Re} = \frac{DU}{\nu}, \tag{1.9}$$

expressing the ratio of the inertia of the fluid and the viscous forces. By comparing the inertia and the surface tension forces of the liquid of the impacting drop one obtains the Weber number

$$\mathrm{We} = \frac{\rho D U^2}{\gamma}. \tag{1.10}$$

We can also consider the thermal properties of the liquid, where we can define the ratio between the sensible heat and the latent heat as the Stefan number

$$\mathrm{Ste} = \frac{c_p \Delta T}{L}. \tag{1.11}$$

The advective and diffusive transport rates compared results in the Péclet number

$$\mathrm{Pe} = \frac{DU}{\kappa}. \tag{1.12}$$

The last dimensionless group can be expressed as an energy ratio of the kinetic energy and the latent heat of solidification L:

$$\Pi = \frac{U^2}{L}. \tag{1.13}$$

The use of dimensionless groups reduces the number of parameters to study, but it also results in a way to compare the impact of drops of different liquids, dimensions and velocities. Unfortunately it is not possible to match all dimensionless groups at the same time, however we can study the effect of a single or a few group(s). Once we neglect the thermal properties of the drop, i.e. the entire process happens at the same temperature at which the drop remains liquid, We and Re are the two remaining parameters. To study a drop formed during plasma generation, we want to know the outcome of a D = 1 μm and U = 100 m/s impacting tin drop. Using dimensional analysis it is possible to study the impact of a larger and slower drop of a different liquid. The tin drop has We = 128 and Re = 377, which we can match with a water drop of D = 15 μm and U = 25 m/s. The dimensions of the drop have increased and the velocity decreased, making it easier to study the outcome of the drop impact. Another example of a typical tin drop in the EUV source is given in table 1.1.

For the work presented in this thesis, we make use of dimensional analysis to make the experiments better accessible for imaging. The transition from fast small tin drops to larger slower water drops also implies that experiments can take place at ambient conditions. However, for studying the effect of substrate temperature we have to use tin drops for our experiments, since the thermal properties of water and tin cannot be matched in an experimentally accessible regime.

Table 1.1: Liquid properties for tin and water drops. These properties are used to calculate dimensionless numbers, of which some are comparable for water and tin despite the different absolute values of the liquid properties.

Parameter	*Description [unit]*	*Tin*	*Water*
ν	liquid kinematic viscosity [m^2/s]	$2.66 \cdot 10^{-7}$	$1 \cdot 10^{-6}$
ρ	liquid density [kg/m^3]	6968	1000
γ	surface tension [N/m]	0.544	0.072
c_p	specific heat [J/(kg K)]	227	$4.18 \cdot 10^3$
ΔT	temperature difference [K] (interface and melting)	140	20
L	latent heat [J/kg]	$5.85 \cdot 10^4$	$3.34 \cdot 10^5$
κ	thermal diffusivity [m^2/s]	$2 \cdot 10^{-5}$	$1.44 \cdot 10^{-7}$
U	typical impact velocity [m/s]	82	20
D	typical drop diameter [μm]	6.5	100
Re	Reynolds number (1.9)	2000	2000
We	Weber number (1.10)	555	555
Ste	Stefan number (1.11)	0.54	0.24
Pe	Péclet number (1.12)	27	$1.4 \cdot 10^4$

1.5 Suppression of drop splashing

To control the tin debris in the source chamber of the nanolithography machine it is important to understand the transition from deposition to splashing for different conditions. In this thesis, we therefore focus on this transition. There are numerous ways to influence the transition to splashing, by varying the properties of the substrate or the surrounding air. Here, three variations to increase the transition to splashing are studied, from which one can understand when splashing is to be expected.

Parts of the hardware might be covered with a liquid tin layer and the drops missed by the laser pulses impact onto a liquid pool in the tin catcher. Therefore we consider water drop splashing onto a deep liquid pool in Chap. 2. We study the influence of the impact angle on the splashing behavior and the cavity dynamics. Our goal is to find a transition to splashing depending on the impact angle and the impact velocity. Next to the transition to splashing, we also model the maximal dimensions of the cavity formed during impact. Since the focus here is on the influence of the impact angle and velocity and not on thermal effects, dimensional analysis allows us to replace tin by water.

When tin debris from the plasma generation is directed towards the collector mirror, it impacts onto a cold substrate. In Chap. 3 we study the influence of substrate temperature on drop splashing and spreading. Since we cannot neglect the influence of cooling and solidification during the impact, we let tin drops impact onto a substrate of which we control the temperature. We aim to find an optimal temperature at which splashing and hence contamination of the hardware is minimized.

In Chap. 4 we suppress splashing by changing the elastic properties of the substrate. We modify the splashing criterion (Eq. 1.7) to take the elastic properties of our substrate into account and show that the threshold increases with decreasing elasticity.

In Chap. 5 we focus on practical applications of the work to suppress drop splashing and to minimize the contamination inside the EUV source. We show how substrate properties can be used to suppress splashing. Moreover, we present a method for post-analysis of a witness sample to determine what kind of drops (size, velocity, impact angle) have impacted, such that the source of these drops can be determined. Finally, Chap. 6 concludes the work of this thesis, and gives an outlook to future work.

References

[1] A. M. Worthington, “On the forms assumed by drops of liquids falling vertically on a horizontal plate”, Proc. R. Soc. **25**, 261–272 (1876).

[2] M. Versluis, “High-speed imaging in fluids”, Exp. Fluids **54**, 1458 (2013).

[3] A. Yarin, "Drop impact dynamics: Splashing, spreading, receding, bouncing…", Annu. Rev. Fluid Mech. **38**, 159–192 (2006).

[4] R. Rioboo, A. Tropea, and M. Marengo, "Outcomes from a drop impact on solid surfaces", Atomization Spray **11** (2001).

[5] J. De Ruiter, R. Lagraauw, D. Van Den Ende, and F. Mugele, "Wettability-independent bouncing on flat surfaces mediated by thin air films", Nat. Phys. **11**, 48–53 (2015).

[6] Y. Liu, L. Moevius, X. Xu, T. Qian, J. M. Yeomans, and Z. Wang, "Pancake bouncing on superhydrophobic surfaces", Nat. Phys. **10**, 385388 (2014).

[7] J. Zou, P. F. Wang, T. R. Zhang, X. Fu, and X. Ruan, "Experimental study of a drop bouncing on a liquid surface", Phys. Fluids **23** (2011).

[8] D. Richard and D. Quéré, "Bouncing water drops", Europhys. Lett. **50**, 769–775 (2000).

[9] D. Richard, C. Clanet, and D. Quéré, "Surface phenomena: Contact time of a bouncing drop", Nature **417**, 811 (2002).

[10] R. Rioboo, M. Marengo, and C. Tropea, "Time evolution of liquid drop impact onto solid, dry surfaces", Exp. Fluids **33**, 112–124 (2002).

[11] D. Bartolo, C. Josserand, and D. Bonn, "Retraction dynamics of aqueous drops upon impact on non-wetting surfaces", J. Fluid Mech. **545**, 329338 (2005).

[12] N. Laan, K. G. de Bruin, D. Bartolo, C. Josserand, and D. Bonn, "Maximum diameter of impacting liquid droplets", Phys. Rev. Appl. **2**, 044018 (2014).

[13] M. Pasandideh-Fard, Y. M. Qiao, S. Chandra, and J. Mostaghimi, "Capillary effects during droplet impact on a solid surface", Phys. Fluids **8** (1996).

[14] J. Eggers, M. A. Fontelos, C. Josserand, and S. Zaleski, "Drop dynamics after impact on a solid wall: Theory and simulations", Phys. Fluids **22** (2010).

[15] T. Tran, H. J. J. Staat, A. Prosperetti, C. Sun, and D. Lohse, "Drop impact on superheated surfaces", Phys. Rev. Lett. **108**, 036101 (2012).

[16] B. B. J. Stapelbroek, H. Jansen, E. S. Kooij, J. H. Snoeijer, and A. Eddi, "Universal spreading of water drops on complex surfaces", Soft Matter (2014).

[17] M. Lee, Y. S. Chang, and H.-Y. Kim, "Drop impact on microwetting patterned surfaces", Phys. Fluids **22** (2010).

[18] C. Antonini, A. Amirfazli, and M. Marengo, "Drop impact and wettability: From hydrophilic to superhydrophobic surfaces", Phys. Fluids **24** (2012).

[19] Š. Šikalo and E. Ganić, "Phenomena of droplet–surface interactions", Exp. Therm. Fluid Sci. **31**, 97 – 110 (2006).

[20] Š. Šikalo, C. Tropea, and E. Ganić, "Impact of droplets onto inclined surfaces", J. Colloid Interf. Sci. **286**, 661 – 669 (2005).

[21] D. G. K. Aboud and A.-M. Kietzig, "Splashing threshold of oblique droplet impacts on surfaces of various wettability", Langmuir **31**, 10100–10111 (2015).

[22] C. Antonini, F. Villa, and M. Marengo, "Oblique impacts of water drops onto hydrophobic and superhydrophobic surfaces: outcomes, timing, and rebound maps", Exp. Fluids **55**, 1–9 (2014).

[23] L. Xu, "Liquid drop splashing on smooth, rough, and textured surfaces", Phys. Rev. E. **75**, 056316 (2007).

[24] M. M. Driscoll and S. R. Nagel, "Ultrafast interference imaging of air in splashing dynamics", Phys. Rev. Lett. **107**, 154502 (2011).

[25] C. Josserand and S. Thoroddsen, "Drop impact on a solid surface", Ann. Rev. Fluid Mech. **48**, 365–391 (2016).

[26] R. D. Deegan, P. Brunet, and J. Eggers, "Complexities of splashing", Nonlinearity **21**, C1 (2008).

[27] E. Castillo-Orozco, A. Davanlou, P. K. Choudhury, and R. Kumar, "Droplet impact on deep liquid pools: Rayleigh jet to formation of secondary droplets", Phys. Rev. E 053022 (2015).

[28] S. Yang, Y. An, and Q. Liu, "Effect of viscosity on motion of splashing crown in high speed drop impact", Appl. Math. Mech. (2017).

[29] I. V. Roisman, A. Lembach, and C. Tropea, "Drop splashing induced by target roughness and porosity: The size plays no role", Adv. Colloid Interfac. **222**, 615 – 621 (2015), reinhard Miller, Honorary Issue.

[30] A. Latka, A. M. P. Boelens, S. R. Nagel, and J. J. d. Pablo, "Drop splashing is independent of substrate wetting", arXiv, 1607.08867v1.

[31] C. J. Howland, A. Antkowiak, J. R. Castrejón-Pita, S. D. Howison, J. M. Oliver, R. W. Style, and A. A. Castrejón-Pita, "It's harder to splash on soft solids", Phys. Rev. Lett. **117**, 184502 (2016).

[32] R. E. Pepper, L. Courbin, and H. A. Stone, "Splashing on elastic membranes: The importance of early-time dynamics", Phys. Fluids **20**, 082103 (2008).

[33] H. J. J. Staat, T. Tran, B. Geerdink, G. Riboux, C. Sun, J. M. Gordillo, and D. Lohse, "Phase diagram for droplet impact on superheated surfaces", J. Fluid Mech. **779** (2015).

[34] S. Chandra and P. Fauchais, "Formation of solid splats during thermal spray deposition", J. Therm. Spray Techn. **18**, 148–180 (2009).

[35] R. Dhiman and S. Chandra, "Freezing-induced splashing during impact of molten metal droplets with high weber numbers", Int. J. Heat Mass Tran. **48**, 5625 – 5638 (2005).

[36] R. Dhiman, A. G. McDonald, and S. Chandra, "Predicting splat morphology in a thermal spray process", Surf. Coat. Tech. **201**, 7789 – 7801 (2007).

[37] S. D. Aziz and S. Chandra, "Impact, recoil and splashing of molten metal droplets", Int. J. Heat Mass Tran. **43**, 2841 – 2857 (2000).

[38] R. Bhola and S. Chandra, "Parameters controlling solidification of molten wax droplets falling on a solid surface", J. Mater. Sci. **34**, 4883–4894 (1999).

[39] M. Pasandideh-Fard, V. Pershin, S. Chandra, and J. Mostaghimi, "Splat shapes in a thermal spray coating process: Simulations and experiments", J. Therm. Spray Techn. **11**, 206–217 (2002).

[40] C. Mundo, M. Sommerfeld, and C. Tropea, "Droplet-wall collisions: Experimental studies of the deformation and breakup process", Int. J. Multiphas. Flow **21**, 151 – 173 (1995).

[41] C. Josserand and S. Zaleski, "Droplet splashing on a thin liquid film", Phys. Fluids **15**, 1650–1657 (2003).

[42] F. E. C. Culick, "Comments on a Ruptured Soap Film", J. Appl. Phys. **31**, 1128–1129 (1960).

[43] S. T. Thoroddsen, "The ejecta sheet generated by the impact of a drop", J. Fluid Mech. **451**, 373–381 (2002).

[44] G. Riboux and J. M. Gordillo, "Experiments of drops impacting a smooth solid surface: A model of the critical impact speed for drop splashing", Phys. Rev. Lett. **113**, 024507 (2014).

[45] A.-L. Biance, C. Pirat, and C. Ybert, "Drop fragmentation due to hole formation during leidenfrost impact", Phys. Fluids **23** (2011).

[46] L. Wachters and N. Westerling, "The heat transfer from a hot wall to impinging water drops in the spheroidal state", Chem. Eng. Sci. **21**, 1047 – 1056 (1966).

[47] A. Tirella, F. Vozzi, C. D. Maria, G. Vozzi, T. Sandri, D. Sassano, L. Cognolato, and A. Ahluwalia, "Substrate stiffness influences high resolution printing of living cells with an ink-jet system", J. Biosci. Bioeng. **112**, 79 – 85 (2011).

[48] D. B. van Dam and C. L. Clerc, "Experimental study of the impact of an ink-jet printed droplet on a solid substrate", Phys. Fluids **16**, 3403 – 3414 (2004).

[49] Z. Djuric and P. Grant, "Two-dimensional simulation of liquid metal spray deposition onto a complex surface: Ii. splashing and redeposition", Model. Simul. Mater. Sc. **9**, 111 (2001).

[50] C. A. E. Peirce, C. Priest, T. M. McBeath, and M. J. McLaughlin, "Uptake of phosphorus from surfactant solutions by wheat leaves: spreading kinetics, wetted area, and drying time", Soft Matter **12**, 209–218 (2016).

[51] A. L. Klein, "Laser impact on flying drops", Ph.D. thesis, University of Twente (2017).

[52] A. Shilov, "EUV lithography makes good progress, still not ready for prime time", URL `https://www.anandtech.com`, accessed: 2017-10-26.

[53] V. Y. Banine, K. N. Koshelev, and G. H. P. M. Swinkels, "Physical processes in euv sources for microlithography", J. Phys. D. Appl. Phys. **44**, 253001 (2011).

[54] A. L. Klein, W. Bouwhuis, C. W. Visser, H. Lhuissier, C. Sun, J. H. Snoeijer, E. Villermaux, D. Lohse, and H. Gelderblom, "Drop shaping by laser-pulse impact", Phys. Rev. Applied **3**, 044018 (2015).

[55] J. W. S. Rayleigh, "Investigation of the character of the equilibrium of an incompressible heavy fluid of variable density", P. Lond. Math. Soc. **s1-14**, 170–177 (1882).

[56] G. F. R. S. Taylor, "The instability of liquid surfaces when accelerated in a direction perpendicular to their planes. I", P. Roy. Soc. Lon. A. Mat. **201**, 192–196 (1950).

[57] D. T. Elg, J. R. Sporre, G. A. Panici, S. N. Srivastava, and D. N. Ruzic, "In situ collector cleaning and extreme ultraviolet reflectivity restoration by hydrogen plasma for extreme ultraviolet sources", J. Vac. Sci. Technol. A. **34**, 021305 (2016).

[58] P. K. Kundu, I. M. Cohen, and D. R. Dowling, *Fluid Mechanics*, 5th edition (Elsevier) (2012).

2

Oblique drop impact onto a deep liquid pool *†

Oblique impact of drops onto a solid or liquid surface is frequently observed in nature. Most studies on drop impact and splashing, however, focus on perpendicular impact. Here, we study oblique impact of 100 µm drops onto a deep liquid pool, where we quantify the splashing threshold, maximum cavity dimensions and cavity collapse by high-speed imaging above and below the water surface. Gravity can be neglected in these experiments. Three different impact regimes are identified: smooth deposition onto the pool, splashing in the direction of impact only, and splashing in all directions. We provide scaling arguments that delineate these regimes by accounting for the drop impact angle and Weber number. The angle of the axis of the cavity created below the water surface follows the impact angle of the drop irrespectively of the Weber number, while the cavity depth and its displacement with respect to the impact position do depend on the Weber number. Weber number dependency of both the cavity depth and displacement is modeled using an energy argument.

*Published as: "Oblique drop impact onto a deep liquid pool", Marise V. Gielen, Pascal Sleutel, Jos Benschop, Michel Riepen, Victoria Voronina, Claas Willem Visser, Detlef Lohse, Jacco H. Snoeijer, Michel Versluis, and Hanneke Gelderblom, Phys. Rev. Fluids 2, 083602 (2017).

†MVG and PS contributed equally to this work.

2.1 Introduction

In nature, oblique drop impact is ubiquitous. It is for example encountered in rain drop impact onto waves or puddles [1], where it triggers air entrainment [2] and aerosol generation [3] that drive the global gas-liquid exchange. In agriculture, e.g., in pesticides crop spraying [4], oblique drop impact and the subsequent splashing and droplet rebound [5] is important. In industrial applications oblique impact occurs in, e.g., metal spray deposition [6] and direct fuel injection internal combustion engines [7]. In many of these applications, splashing is an unwanted side effect after impact; it decreases the deposition efficiency and may lead to a widespread contamination.

While drop impact and splashing is a topic widely studied (see, e.g., Refs. [8–22]), surprisingly few papers (e.g., Refs. [23–26]) deal with non-perpendicular or oblique impact. Drop splashing upon perpendicular impact has been studied on a solid substrate [12, 13], a thin liquid film [14–16] and a deep liquid pool [17–22]. In the last case, a cavity is formed under the water surface [2]. Collapse of this cavity [27–29] may lead to the pinch-off of small droplets [1, 30]. These droplets emerge from a high-speed microjet, and can reach velocities higher than the impact velocity [31]. The main parameter that governs splashing is the Weber number, $\mathrm{We} = \frac{\rho D U^2}{\gamma}$ with drop diameter D, drop velocity U, liquid surface tension $\gamma = 0.072$ N/m, and liquid density $\rho = 1000$ kg/m^3. In addition, the splashing threshold depends on the Reynolds number, $\mathrm{Re} = \frac{UD}{\nu}$, with ν the kinematic viscosity. A standard splashing threshold has the form of $\mathrm{We}^{1/2}\mathrm{Re}^{1/4} = K$ [8, 13] where K is a constant that depends on the surrounding pressure [32], the thickness of the liquid layer, and the surface roughness when a drop impacts onto a rigid substrate.

To study oblique impact, experiments onto dry tilted plates [23–26] and onto a moving plate [33] were performed. Bird *et al.* [33] showed that by moving the substrate, the velocity of the ejecta sheet and therefore the splashing threshold changes. Only a few studies [34–39] focus on oblique impact onto wetted surfaces and thin liquid films. Gao and Li [38] quantify a splashing threshold for impact onto a moving thin liquid film, but due to experimental complications such as the liquid inertia, this approach is not feasible for a deep liquid pool.

In numerical simulations, oblique impact onto a wetted substrate [40–42] shows a transition from crown splashing to single-sided splashing. In addition, crown formation and cavity formation [42] are studied. Due to the aforementioned experimental limitations these simulations lack validation. For oblique drop impact onto a wetted or dry surface, there is a clear influence of the impact angle on the splashing, but to our best knowledge no experiments of oblique drop impact onto a liquid pool have been reported in the literature.

Here, we present an experimental study of oblique drop impact onto a quiescent deep liquid pool. We provide details of our experimental method in Sec. 2.2 and

discuss a typical result for the impact and splashing phenomena in Sec. 2.3.1. The angle of impact is varied systematically to quantify the splashing threshold and a model to explain these observations is presented in Sec. 2.3.2. We also quantify the cavity formation and present a scaling law for the cavity formation in Sec. 2.3.3.

2.2 Experimental methods

To study oblique drop impact for a wide range of Weber numbers and impact angles onto a deep liquid pool, two steps are important: (1) creation of a single drop and (2) rotation of the drop generator to obtain oblique impact. To create single drops a method previously described in Ref. [43] is used, which we adopt for oblique impact. For clarity, we briefly describe this method to isolate single drops from a stream of drops here, which is schematically drawn in Fig. 2.1(a).

Drops of size of 115 ± 15 μm are generated by pumping (Shimadzu LC-20AD HPLC pump) demineralized water ($<$0.1% of ammonia added for conductivity, negligible effects on surface tension) through a micropipette (Microdrop AD K-501). The continuous jet breaks up into drops by applying a piezoacoustic pressure on the jet, which transforms the jet into a stream of monodisperse drops with equal velocity. Velocities ranging from 6 up to 25 m/s can be achieved resulting in Weber numbers between 40 and 1056. Here, the lower bound is set by the minimum velocity required to create a train of drops and the upper bound by the maximal flow rate of the apparatus. The drop train is directed through a ring-shaped charging electrode, where a periodic high-voltage pulse charges all passing drops except one every 10 ms. Next, the drops pass another region with a high electric field ($E \geq 100$ kV/m) between two deflection plates. The electric field separates the charged drops from the uncharged ones, and allows for the uncharged drops to continue straight and impact onto the pool. The pool consists of a glass container that is filled to the top with water to minimize the influence of a disturbing meniscus at the container wall that may limit the optical imaging quality. The charged drops are caught further on their path and then disposed. To create an oblique impact, the micropipette, charge electrode, and deflection plates are tilted. In this way, impact angles up to 80° from perpendicular can be obtained. This method allows for the creation of oblique drop impact with a wide range of velocities and a large enough drop spacing to prevent disturbances of the pool due to earlier impact events.

Figure 2.1(b) shows a sketch of drop velocity U and impact angle α. These parameters are varied systematically, while keeping the drop diameter D constant. By doing so, we effectively change the ratio between the perpendicular impact velocity $U_\perp = U\cos\alpha$ and the parallel impact velocity $U_\parallel = U\sin\alpha$. Note that $U_\perp$ and $U_\parallel$ cannot be varied completely independently since a minimum total velocity U is required to create a train of drops.

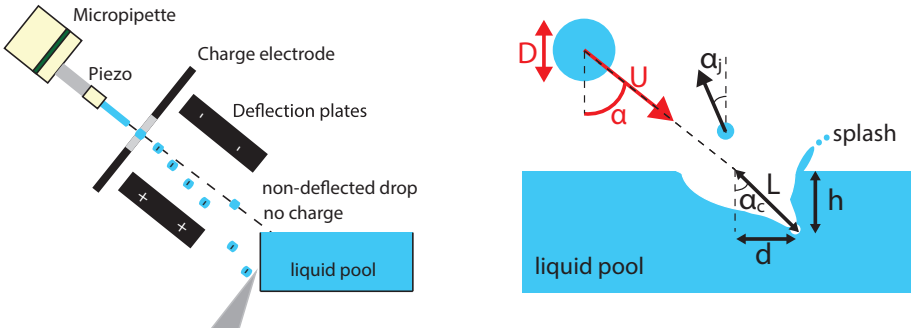

Figure 2.1: (a) Sketch of the experimental setup. A continuous stream of drops is created by piezoelectric actuation of a microjet. A charging electrode charges the drops, which are subsequently deflected by the deflection plates. Every 10 ms a single drop is left uncharged and can be separated from the stream. By tilting the micropipette, charging electrode, and deflection plates, the impact angle α of the drops onto the pool can be varied. The pool has a depth of 10 mm, a width of 10 mm, and a length of 100 mm. (b) Drop diameter D, velocity U, and impact angle α are controlled by the experiment, and cavity displacement d and height h are measured, which results in cavity angle α_c and a characteristic length of the cavity L. Next to that, the angle of the jetted droplet out of the cavity α_j is measured. The shape of the splash and the collapse of the cavity are recorded by two separate high-speed recordings above and below the water surface, respectively.

Drop impact is recorded in a side view by high-speed imaging (Photron SA-X2, operated at frame rates up to 100 kfps, average pixel resolution of 3.2 μm) and backlight illumination (Olympus ILP-2). From these recordings, we extract D, U, and α using a customized image-processing analysis. The impact velocity is measured from the penultimate frames just before impact to minimize the influence of air drag. The error in these measurements is estimated to be 2 μm for D and 0.2 m/s for U, both based on the camera resolution. For a typical measured velocity of U = 15 m/s, these errors result in an error in We of about 15 and in α of about 2°.

The dynamics of the cavity is characterized simultaneously with the impact event by collecting two separate recordings for each impact condition, one above and one below the water surface, in order to compensate for the different optical focal depth. From the measurements above the water surface we characterize the direction of the splash. From the cavity recordings, we estimate the maximum cavity displacement d, maximum height h and define the cavity angle α_c by $\tan\alpha_c = \left(\frac{d}{h}\right)$. These maximum dimensions are not always clearly pronounced. We therefore obtain d and h, and hence α_c, from an average of six measurements above and below the water surface for each impact condition. The typical errors obtained are a few μm in d and h and a few degrees in α_c. In total, to quantify the cavity dimensions and collapse below the water surface and the splashing threshold above the water surface, we analyzed 1147 individual drop impacts.

2.3 Results and interpretation

2.3.1 Typical features of oblique drop impact

Figure 2.2 shows the time series of a typical experiment with We = 674 and α = 28°. Qualitatively the different stages of oblique impact are comparable to perpendicular impact, but with some important qualitative differences, which we will now discuss.

Figure 2.2(a) shows a snapshot 0.02 ms after the drop has impacted. The formation of a hemispherical cavity has started below the water surface, and an asymmetric splash ejecting small droplets is visible above the water surface. At t = 0.1 ms [2.2(b)], both the crown and the cavity are growing. In contrast to perpendicular impact the droplets only detach on a single side. Just below the water surface, a wave crest is observed [28]. At t = 0.28 ms (2.2(c)) this wave crest is highlighted by an arrow while it travels downward along the cavity wall. Here one can clearly observe that the cavity is asymmetric. At this point in time, the cavity is still growing while surface tension causes the crown to retract and the rim to grow thicker. Figure 2.2(d) (t = 0.66ms) shows the cavity at its deepest point, where the maximum cavity depth and displacement are reached. Then, the closure of the cavity starts and the capillary wave crest collides at the bottom of the cavity. During the collision of these waves an air bubble can be entrapped [2]. The tip at the bottom of the cavity in 2.2(d) marks this

air bubble just before pinch-off. The tip will retract quickly due to the high local curvature. The series of subsequent image frames suggest that the jetted droplet, which is visible above the water surface in Fig. 2.2(e) at $t = 0.77$ ms, originates from the rapid tip retraction. The droplets jetted out of the cavity reach velocities of the same order as the main drop impact velocity. Below the water surface [2.2(e)] a tiny bubble is clearly visible. At $t = 1.02$ ms [2.2(f)] the cavity has completely collapsed, marked by the emergence of a thick Worthington jet [44].

2.3.2 Splashing threshold

After drop impact three different phenomena can be observed above the water surface, as illustrated in Fig. 2.3(a). First, the drop can smoothly coalesce with the liquid pool. This behavior is identified as deposition. Second, a crown can be formed, which destabilizes on a single side of the drop and results in the ejection of satellite droplets at the tips of the crown on this side of the drop. The direction of splashing corresponds to the direction of impact. This behavior is denoted as single-sided splashing. The final phenomenon observed is the ejection of small satellite droplets from the crown in all directions, which is indicated as omni-directional splashing. We quantify these phenomena in a phase diagram of α and We illustrated by three distinct regions; see Fig. 2.3(b). For a single value of α the impact behavior can change from deposition to single-sided splashing to omni-directional splashing for increasing We. Similarly, for a single value of We the impact behavior can change from omni-directional splashing to single-sided splashing to deposition for increasing α.

We now provide a scaling argument to explain these observations. To find the splashing threshold for oblique impact, we aim to describe the velocity of the crown in terms of U, D, α, and We. We start by considering perpendicular (i.e. vertical) impact. A schematic view of the drop during impact is shown in Fig. 2.4(a). In this case, the flow into the crown is distributed symmetrically. Once the entire drop has impacted, we can assume that the entire drop volume is proportional to the volume of the crown, which gives (per unit time) [15]

$$D^2U \sim eDV, \tag{2.1}$$

where e is the thickness of the crown at its origin. In line with a model for splashing of the fast ejecta onto a thin liquid film [15], we assume that in order to obtain splashing upon impact onto a liquid pool the velocity of the crown V has to be larger than the Taylor-Culick velocity $V_{TC} \sim \sqrt{\frac{\gamma}{\rho e}}$. Thoroddsen [21] showed experimentally that $e \sim \sqrt{\nu t}$, consistent with dimensional analysis. Using $t \sim \frac{D}{U}$ in the expression for e and (2.1) to express V we find the splashing criterion

$$\frac{V}{V_{TC}} \sim \mathrm{We}^{1/2}\mathrm{Re}^{1/4} > K, \tag{2.2}$$

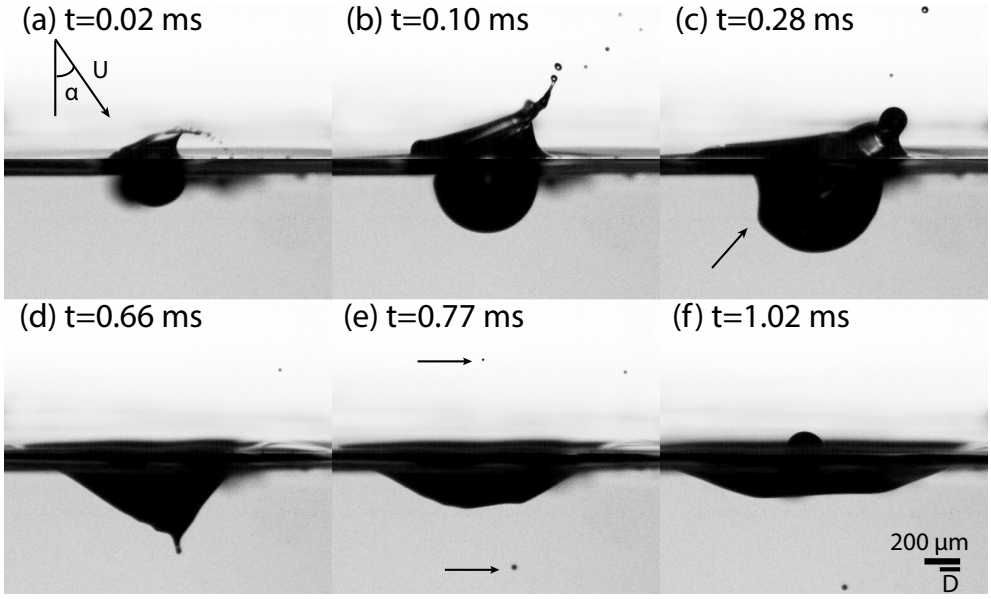

Figure 2.2: Time series of a drop impacting onto the pool with a Weber number We = 674 and impact angle $\alpha = 28^\circ$, where $t = 0$ marks the moment the drop makes first contact with the pool. In this caption time t is non-dimensionalized to $t^* = \frac{t}{t_{imp}} = \frac{tU}{D}$ while in the figure the dimensional time is given. (a) $t^* = 3.6$. The impacting drop causes a splash that fragments into droplets. Here, the splash is formed on a single side only. (b) $t^* = 18$. A crown develops and remains more pronounced on one side. The cavity has a hemispherical shape and is growing. (c) $t^* = 51$. The splashing is finished and the cavity still grows. An arrow points to the wave crest, which travels downwards along the cavity surface; see Ref. [28]. The oblique impact leads to an asymmetry of the cavity. (d) $t^* = 119$. The capillary wave focuses off-center at the bottom of the cavity. (e) $t^* = 139$. Collapse of the wave leads to the entrainment of a bubble and retraction of the jet leads to the ejection of tiny droplets during closure of the cavity. The arrows indicate the position of the entrained bubble and the droplets. (f) $t^* = 184$. A Worthington jet is formed during closure of the cavity [44].

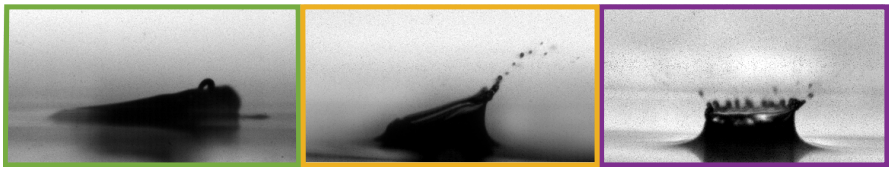

(a)

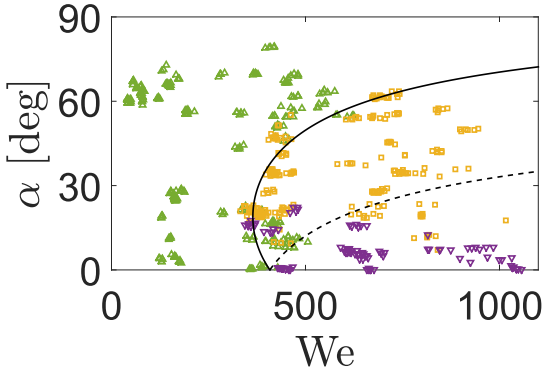

(b)

Figure 2.3: (a) Three types of impact behavior are observed above the water surface. From left to right: deposition (green), single-sided splashing (yellow), and omni-directional splashing (purple). (b) A phase diagram of the impact behavior as a function of the Weber number We and impact angle α. The color codes correspond to (a): upward green triangles represent deposition, yellow squares represent single-sided splashing, and downward purple triangles represent omni-directional splashing. The solid and the dashed line are derived from Eqn. (2.4) with $c = 0.44$, where the solid line represents the splashing threshold from deposition to single-sided splashing [Eqn. (2.4) with plus sign] and the dashed line indicates the splashing threshold from single-sided splashing to omni-directional splashing [Eqn. (2.4) with minus sign].

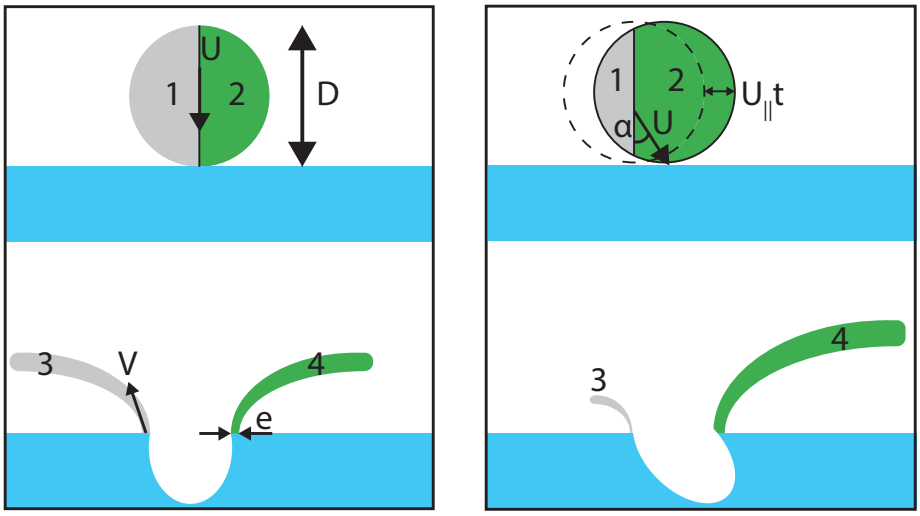

(a) (b)

Figure 2.4: Schematic illustration of the mass distribution in the crown. Volume 1 indicates the part of the original drop that flows into crown volume 3. Volume 2 represents the part of the original drop that flows into crown volume 4. Volumes 1 and 3, and 2 and 4 are identical due to mass conservation. (a) For perpendicular drop impact the volume of the original drop is distributed evenly over the crown, such that volumes 1 and 2, and thus 3 and 4, are identical. (b) For oblique impact, $U_{\parallel}$ will cause a shift (solid line) in drop position with respect to the perpendicular impact (dashed line). This shift reduces volume 1 and increases volume 2 by an amount of $\pm\rho D U_{\perp} U_{\parallel} t$ (see text). As a result, the crown becomes asymmetric.

where K is the critical number for splashing [8, 9, 45].

The numerical value of K depends on specific experimental conditions, such as the flow profile inside the crown [15]. Previous studies reported $K \approx 54$ for a rigid surface [9], $K \approx 160$ for a thin liquid film [14], and $K \approx 90$ for a deep liquid pool [20]. For our experiments we determine for perpendicular impact ($\alpha \simeq 0^{\circ}$) a critical Weber number for splashing of about $\mathrm{We}_s \approx 400$ which leads to $K \approx 130$.

For oblique impact the mass is no longer symmetrically distributed over the crown: the mass flow into the crown increases on one side of the drop and decreases on the other side of the drop (Fig. 2.4(b)). This unequal mass distribution originates from the contribution of the tangential component of the impact velocity $U_{\parallel}$. On one side of the drop, $U_{\parallel}$ leads to an increased mass flow, while on the other side the mass flow is decreased. The added or reduced mass flow rate into the crown scales as $\pm\rho D U_{\perp} U_{\parallel} t$, respectively, where $U_{\perp}$ sets the speed with which the drop is moving down into the

pool. To account for this additional mass flow, we rewrite (2.1) as

$$D^2U_\perp \pm cDU_\perp U_\parallel t \sim eDV, \tag{2.3}$$

where c is a fit parameter that accounts for the exact amount of mass that is redistributed over the crown. The (critical) velocity for crown splashing now depends on both $U_\perp$ and $U_\parallel$. From (2.3) it follows that $U_\perp \left[1 \pm c\frac{U_\parallel t}{D}\right] \sim \frac{Ve}{D}$ and hence the splashing criterion for oblique impact reads, with $t \sim \frac{D}{U_\perp}$,

$$\frac{V}{V_{TC}} \sim \mathrm{We}^{1/2}\mathrm{Re}^{1/4}(\cos\alpha)^{5/4}\left[1 \pm c\tan\alpha\right] > K. \tag{2.4}$$

In (2.4), we use $K = 130$ (as determined for perpendicular impact) to find the splashing threshold as a function of We and α. These considerations show that there are two transitions in the phase space of Fig 2.3(b): (1) A transition from deposition to single-sided splashing when V_{TC} is reached on a single side of the drop (solid line). (2) A transition from single-sided splashing to omni-directional splashing when V_{TC} is reached for splashing in all directions (dashed line).

In Fig. 2.3(b) we plot these transitions and we find qualitative agreement with the experimental data using $c = 0.44$. The model also quantitatively captures the transition from deposition to single-sided splashing, while the predicted transition from single-sided to omni-directional splashing shows a stronger deviation from experiment. Moreover, we experimentally observe a zone where all three impact behaviors overlap for We around 400 and $\alpha < 20^\circ$, which is absent in the model. In this transition region the three impact behaviors are close together. As a consequence, this region is very sensitive to small experimental variations in We and α. In addition, smaller droplets ejected in a splash might not be observable because of the camera resolution, which further complicates the judgment on the impact behavior. More importantly, three-dimensional effects that occur outside the observation plane make it difficult to discriminate between single-sided splashing and omni-directional splashing in a discrete manner: the transition is not sharp but gradual. Therefore the dashed line in Fig. 2.3(b) is far from perfect in separating between single-sided and omni-directional splashing.

2.3.3 Cavity formation

From our recordings we extract the angle α_c, as defined in fig 2.1(b), and the dimensions (h and d) of the cavity. In Fig. 2.5 cavity angle α_c is plotted as a function of impact angle α. For small impact angles the cavity angle equals the impact angle, which is expected since the momentum of the drop is transferred to the cavity in the direction of impact. However, for impact angles larger than $\alpha \gtrsim 30^\circ$, α_c gets increasingly smaller as compared to α. The measurement error of α_c does not explain

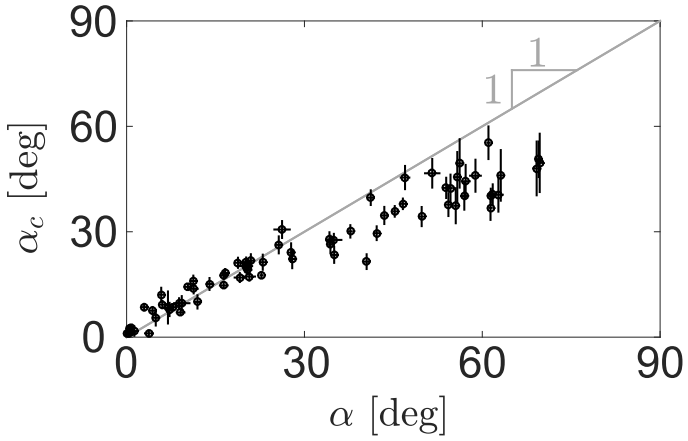

Figure 2.5: Cavity angle α_c as a function of the impact angle α. The solid line has slope unity. Each data point is the average value of six separate experiments, where the error bars indicate the propagated error in α_c corresponding to the measurement error in d and h.

the observed decrease. We analyzed the cavity angle as a function of We, but found no significant dependency (data not shown). A possible explanation for the deviation in proportionality of α_c with α for larger impact angles could come from additional wave drag [46] for drops moving almost parallel to the surface (i.e., drops impacting with a large α). For larger impact angles, part of the impact energy will be dissipated into the build-up of waves in the direction tangential to the surface, which reduces the cavity angle.

We now present data on the maximum cavity depth and maximum displacement. In Figs. 2.6 and 2.7 the maximum cavity depth h and displacement d are plotted as a function of We based on the perpendicular impact velocity $\mathrm{We}_\perp = \frac{\rho D U_\perp^2}{\gamma}$ and the tangential velocity $\mathrm{We}_\parallel = \frac{\rho D U_\parallel^2}{\gamma}$, respectively. The data suggests $h \sim \mathrm{We}_\perp^{1/2}$ while $d \sim \mathrm{We}_\parallel^{1/2}$. These scalings can be explained from energy conservation. We consider that the kinetic energy of the impacting drop is proportional to the additional surface energy to create the cavity

$$\rho D^3 U^2 \sim \gamma L^2, \tag{2.5}$$

where L is the characteristic length of the cavity, as shown in Fig. 2.1(b). For oblique impact experiments, L depends on both h and d since the maximum depth of the cavity is displaced by d as a consequence of the tangential component of the impact velocity, resulting in $L \sim \sqrt{h^2 + d^2} \sim h\sqrt{1 + \tan^2 \alpha}$. Here we have assumed $\tan \alpha = \frac{d}{h}$, which

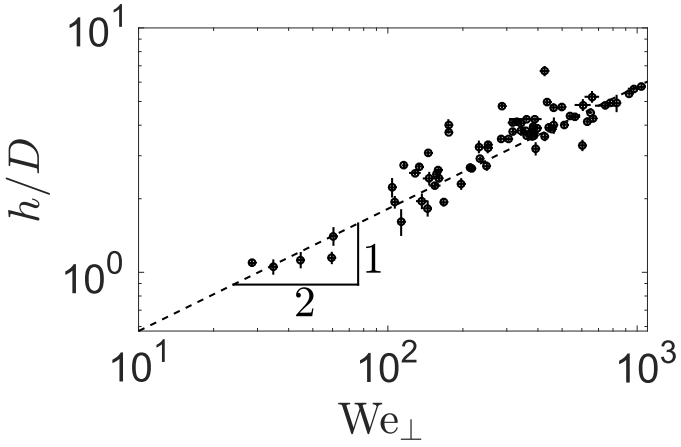

Figure 2.6: Double logarithmic plot of the maximum cavity depth h as a function of the Weber number, based on the perpendicular impact velocity $\mathrm{We}_\perp$. The dashed line corresponds to Eqn. (2.6) and a prefactor of 0.18. Each data point is the average value of six separate experiments with corresponding error bars.

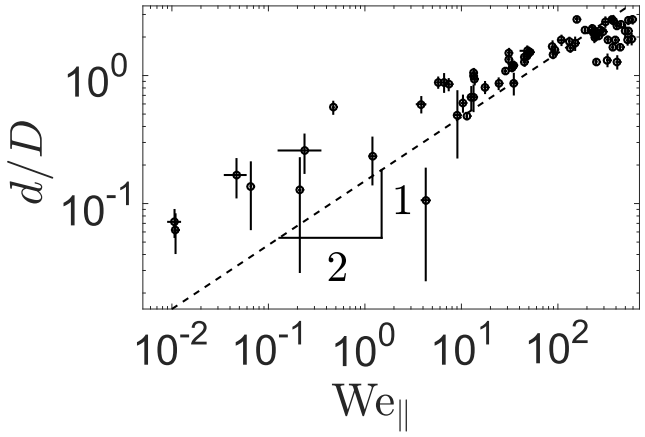

Figure 2.7: Double logarithmic plot of the maximum horizontal cavity displacement d as a function of the Weber number based on the tangential impact velocity $\mathrm{We}_\parallel$. The dashed line corresponds to Eqn. (2.7) and a prefactor of 0.15. Each data point is the average value of six separate experiments with corresponding error bars.

will introduce a small error for $\alpha \gtrsim 30^\circ$, as seen in Fig. 2.5. From (2.5) we find $\frac{L}{D} \sim \mathrm{We}^{1/2}$. Using the geometrical relation for L we find $\frac{h}{D} \sim \mathrm{We}^{1/2} \cos\alpha$, and hence

$$\frac{h}{D} \sim \mathrm{We}_\perp^{1/2}. \tag{2.6}$$

Figure 2.6 shows scaling law (2.6) together with the experimentally determined maximum cavity depth, where we used a prefactor of 0.18. For $\mathrm{We}_\perp > 100$, we observe a somewhat larger spread in h. This spread could be due to capillary waves propagating over the cavity surface, which distort the measurement of h. For the maximum cavity displacement we find $\frac{d}{D} \sim \frac{h}{D} \tan\alpha \sim \mathrm{We}^{1/2} \sin\alpha$, which gives

$$\frac{d}{D} \sim \mathrm{We}_\parallel^{1/2}. \tag{2.7}$$

In Fig. 2.7 scaling (2.7) is plotted with a prefactor 0.15 together with the experimentally determined maximum cavity displacement. For $\mathrm{We}_\parallel \lesssim 100$ we observe a deviation between the experimental data and the proposed scaling. For these small Weber numbers the uncertainty in d (of a few micron) becomes of the order of the value of d that is actually measured. As explained in Sec. 2.2, the perpendicular and parallel impact velocity in our experiment cannot be varied completely independently. Indeed, to achieve the measurements at small $U_\parallel$, and hence small $\mathrm{We}_\parallel$, we had to use a large $U_\perp$ to create a drop train. However, a large $U_\perp$ at small $U_\parallel$ implies a small α and hence a small d, which is hard to measure accurately. In addition, the measure for the cavity displacement is not as well defined as that for the cavity depth: when the cavity becomes less sharp, several values for d could correspond to the same h, which leads to a further spread in the data in Fig. 2.7.

2.4 Discussion on cavity collapse

The collapse of a cavity is sometimes accompanied by the jetting of a droplet out of the cavity; see Fig. 2.8(a). In this subsection we aim to quantify the direction of the jetting behavior. Figure 2.1(b) depicts the angle α_j at which the droplet is jetted out of the cavity. Not every impact leads to the observation of a jetted droplet, which could mean that no droplets were pinched off from the jet, or that droplets remain trapped inside the cavity. Given the small droplet size and the limited depth of field of our imaging system, the ejected droplet could also have moved out of the optical focal plane.

Another observation is that the trajectory of the droplet is curved when it moves out of the cavity, as shown in Fig. 2.8(a). This may be an indication that the initial α_j, directly after pinch-off from the jet, is different from the α_j measured above the closing cavity, where it may be hindered by a disturbing airflow. To better quantify

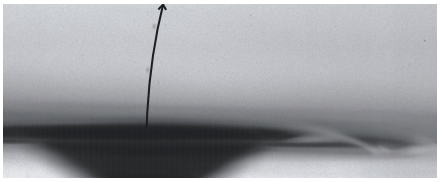

(a)

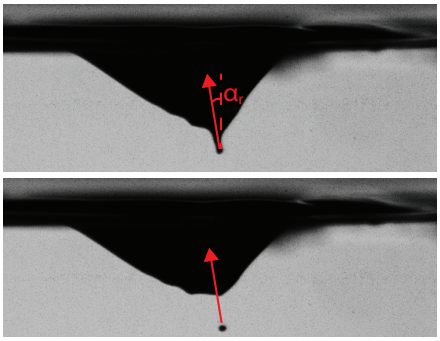

(b)

Figure 2.8: (a) The trajectory of two jetted droplets for We $= 371$ and $\alpha = 0.3°$ shows a deflection when the droplets leave the cavity. This deflection is indicated by the arrow. (b) Snapshot of the cavity at its maximum dimensions (top), and approximately 14 μs later (bottom) when the collapse and tip retraction have started. The red arrows indicate the direction in which the cavity starts to collapse, which is used as a measure for the direction of the jetted droplet out of the cavity.

the jet direction, we therefore change our focus to the cavity collapse and deduce the retraction angle α_r, as depicted in Fig. 2.8(b), where we assume that the onset of retraction of the cavity sets the initial direction of the jetted drop. From a series of frames α_r is measured where the first frame was taken when the cavity is at its maximum dimensions. In the next frames we follow the direction of cavity collapse by tracking this point to find the retraction angle.

As shown in Fig. 2.9(a), α_j and α_r are indeed similar, with α_j being slightly smaller than α_r, which is probably due to the influence of a disturbing airflow, as discussed above. α_r follows α up to about 25°. For $\alpha > 25°$, α_r flattens and reaches a maximum of about 30°. The deviation from α occurs around the same α for both α_c and α_r. However, the build-up of drag waves in front of the impacting drop is not enough to account for the flattening observed for α_r. We speculate that this saturation is caused by a maximum angle that the cavity can make with the surface. For perpendicular impact, the cavity is symmetric and hemispherical, which is energetically most favorable. For oblique impact, the cavity is no longer hemispherical but one side of the cavity wall starts to move inwards (see Fig. 2.9(b)). At the other side the cavity opening grows as surface tension smooths the sharp edge as is illustrated in Fig. 2.9(b) by the shaded area. This effect breaks the symmetry and therefore poses a limit on the maximum value of α_r.

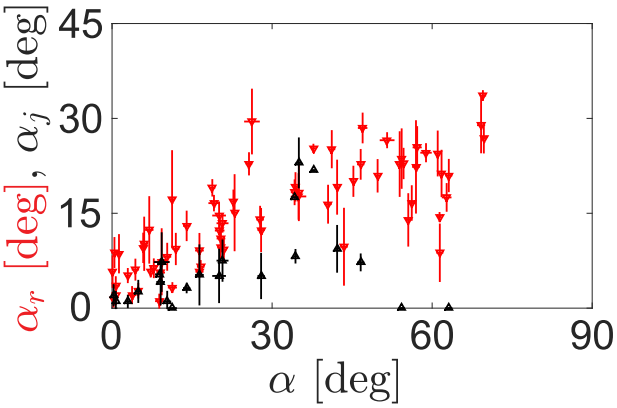

(a)

(b)

Figure 2.9: (a) Angle of the droplet jetted out of the cavity α_j (upward black triangles, each triangle corresponds to the average of about six measurements) and retraction angle of the cavity α_r (downward red triangles, each triangle corresponds to the average taken over six measurements below and above the water surface) as a function of the impact angle α. (b) Schematic view of the cavity angle and the retraction angle. When a drop impacts obliquely, one expects a cavity consisting of the white area, due to symmetry. However, since surface tension prohibits the existence of the sharp corner, the shaded area is pulled outward. Therefore, an asymmetric cavity forms resulting in a retraction angle which is smaller compared to the cavity angle.

2.5 Discussion and Conclusions

We presented an experimental study of oblique drop impact onto a quiescent deep liquid pool. We performed quantitative experiments where drops impact obliquely onto a deep liquid pool for a wide range of Weber numbers and impact angles, and we analyzed the splashing behavior, the cavity formation, and the cavity collapse.

In analogy to previous studies (e.g., Refs. [8, 9, 15, 45]), we found that the crown velocity has to be larger than the Taylor-Culick velocity to obtain splashing. For oblique drop impact this crown velocity is influenced by the tangential velocity of the impacting drop, leading to an asymmetry in the crown and giving rise to an asymmetry in the splashing threshold [33]. In contrast to the model presented in Ref. [33], where oblique drop impact onto a dry substrate was studied, we cannot describe our data by simply adding or subtracting the tangential velocity to the crown velocity. Instead, we assumed the tangential velocity influences the amount of mass squeezed into the crown. We quantified this effect using scaling arguments and derived a model that is consistent with our measurements for a wide range of We and α. Thus, the model gives valuable insight into the occurrence and direction of splashing.

For small impact angle α the cavity angle α_c directly equals the impact angle and does not depend on We, for large α a decrease in α_c with respect to α was observed. The magnitude of the cavity displacement depends on the tangential Weber number and the cavity depth depends on the perpendicular Weber number. The scarce numerical simulations on oblique impact [42] confirm this We-dependence of the cavity displacement. However, since Ref. [42] described drop impact onto a thin liquid film, no information on the cavity depth is available.

In conclusion, our study provides the first quantitative overview of the events following oblique impact onto a deep quiescent liquid pool. The results allow us to predict under what impact velocity and in what direction drops can splash after impact. In our experiment, data from a single measurement plane is obtained. It would be interesting to obtain the full three-dimensional profile above and below the water surface using holographic microscopy [47] or by extended numerical simulations. Further studies will also be required to assess the influence of gravity on splashing and the cavity collapse, which may be relevant for larger droplets as generated by rain or breaking waves.

References

[1] M. Rein, “The transitional regime between coalescing and splashing drops”, J. Fluid Mech. **306**, 145–165 (1996).

[2] H. N. Oguz and A. Prosperetti, “Bubble entrainment by the impact of drops on liquid surfaces”, J. Fluid Mech. **219**, 143–179 (1990).

[3] K. Sellegri, C. O'Dowd, Y. Yoon, S. Jennings, and G. de Leeuw, "Surfactants and submicron sea spray generation", J. Geophys. Res-Atmos. **111** (2006).

[4] C. A. E. Peirce, C. Priest, T. M. McBeath, and M. J. McLaughlin, "Uptake of phosphorus from surfactant solutions by wheat leaves: spreading kinetics, wetted area, and drying time", Soft Matter **12**, 209–218 (2016).

[5] T. Gilet and J. W. M. Bush, "Droplets bouncing on a wet, inclined surface", Phys. Fluids **24** (2012).

[6] Z. Djuric and P. Grant, "Two-dimensional simulation of liquid metal spray deposition onto a complex surface: Ii. splashing and redeposition", Model. Simul. Mater. Sc. **9**, 111 (2001).

[7] Z. Wang, H. Du, J. Liu, L. Han, and S. Liu, "Spray wall-impingement from a single hole nozzle under common rail condition", Adv. Mat. Res. **347-353**, 770–773 (2012).

[8] C. Mundo, M. Sommerfeld, and C. Tropea, "Droplet-wall collisions: Experimental studies of the deformation and breakup process", Int. J. Multiphas. Flow **21**, 151 – 173 (1995).

[9] C. Josserand and S. Thoroddsen, "Drop impact on a solid surface", Ann. Rev. Fluid Mech. **48**, 365–391 (2016).

[10] S. Thoroddsen, K. Takehara, and T. Etoh, "Micro-splashing by drop impacts", J. Fluid Mech. **706**, 560–570 (2012).

[11] L. Zhang, J. Toole, K. Fezzaa, and R. Deegan, "Splashing from drop impact into a deep pool: Multiplicity of jets and the failure of conventional scaling", J. Fluid Mech. **703**, 402–413 (2012).

[12] A. L. Yarin and D. A. Weiss, "Impact of drops on solid surfaces: self-similar capillary waves, and splashing as a new type of kinematic discontinuity", J. Fluid Mech. **283**, 141–173 (1995).

[13] A. Yarin, "Drop impact dynamics: Splashing, spreading, receding, bouncing…", Annu. Rev. Fluid Mech. **38**, 159–192 (2006).

[14] R. D. Deegan, P. Brunet, and J. Eggers, "Complexities of splashing", Nonlinearity **21**, C1 (2008).

[15] C. Josserand and S. Zaleski, "Droplet splashing on a thin liquid film", Phys. Fluids **15**, 1650–1657 (2003).

[16] I. V. Roisman and C. Tropea, "Impact of a drop onto a wetted wall: description of crown formation and propagation", J. Fluid Mech. **472**, 373–397 (2002).

[17] J. O. Marston and S. T. Thoroddsen, "Apex jets from impacting drops", J. Fluid Mech. **614**, 293–302 (2008).

[18] B. Ray, G. Biswas, and A. Sharma, "Bubble pinch-off and scaling during liquid drop impact on liquid pool", Phys. Fluids **24** (2012).

[19] B. Ray, G. Biswas, and A. Sharma, "Regimes during liquid drop impact on a liquid pool", J. Fluid Mech. **768**, 492–523 (2015).

[20] E. Castillo-Orozco, A. Davanlou, P. K. Choudhury, and R. Kumar, "Droplet impact on deep liquid pools: Rayleigh jet to formation of secondary droplets", Phys. Rev. E 053022 (2015).

[21] S. T. Thoroddsen, "The ejecta sheet generated by the impact of a drop", J. Fluid Mech. **451**, 373–381 (2002).

[22] T. Tran, H. De Maleprade, C. Sun, and D. Lohse, "Air entrainment during impact of droplets on liquid surfaces", J. Fluid Mech. **726**, R3 (2013).

[23] Š. Šikalo and E. Ganić, "Phenomena of droplet–surface interactions", Exp. Therm. Fluid Sci. **31**, 97 – 110 (2006).

[24] Š. Šikalo, C. Tropea, and E. Ganić, "Impact of droplets onto inclined surfaces", J. Colloid Interf. Sci. **286**, 661 – 669 (2005).

[25] C. Antonini, F. Villa, and M. Marengo, "Oblique impacts of water drops onto hydrophobic and superhydrophobic surfaces: outcomes, timing, and rebound maps", Exp. Fluids **55**, 1–9 (2014).

[26] D. G. K. Aboud and A.-M. Kietzig, "Splashing threshold of oblique droplet impacts on surfaces of various wettability", Langmuir **31**, 10100–10111 (2015).

[27] R. Bergmann, D. van der Meer, S. Gekle, A. van der Bos, and D. Lohse, "Controlled impact of a disk on a water surface: Cavity dynamics", J. Fluid Mech. **633**, 381–409 (2009).

[28] S. Gekle, A. van der Bos, R. Bergmann, D. van der Meer, and D. Lohse, "Noncontinuous froude number scaling for the closure depth of a cylindrical cavity", Phys. Rev. Lett. **100**, 084502 (2008).

[29] G.-J. Michon, C. Josserand, and T. Séon, "Jet dynamics post drop impact on a deep pool", Phys. Rev. Fluids **2**, 023601 (2017).

[30] S. Gekle, J. M. Gordillo, D. van der Meer, and D. Lohse, "High-speed jet formation after solid object impact", Phys. Rev. Lett. **102**, 034502 (2009).

[31] M. Longuet-Higgins and H. Oguz, "Critical microjets in collapsing cavities", J. Fluid Mech. **290**, 183–201 (1995).

[32] L. Xu, W. W. Zhang, and S. R. Nagel, "Drop splashing on a dry smooth surface", Phys. Rev. Lett. **94**, 184505 (2005).

[33] J. C. Bird, S. S. H. Tsai, and H. A. Stone, "Inclined to splash: triggering and inhibiting a splash with tangential velocity", New J. Phys. **11**, 063017 (2009).

[34] S. K. Alghoul, C. N. Eastwick, and D. B. Hann, "Normal droplet impact on horizontal moving films: an investigation of impact behaviour and regimes", Exp. Fluids **50**, 1305–1316 (2011).

[35] T. Okawa, T. Shiraishi, and T. Mori, "Effect of impingement angle on the outcome of single water drop impact onto a plane water surface", Exp. Fluids **44**, 331–339 (2008).

[36] Z. Che, A. Deygas, and O. K. Matar, "Impact of droplets on inclined flowing liquid films", Phys. Rev. E **92**, 023032 (2015).

[37] G. Liang, Y. Guo, Y. Yang, N. Zhen, and S. Shen, "Spreading and splashing during a single drop impact on an inclined wetted surface", Acta Mechanica **224**, 2993–3004 (2013).

[38] X. Gao and R. Li, "Impact of a single drop on a flowing liquid film", Phys. Rev. E **92**, 053005 (2015).

[39] J. R. Castrejón-Pita, B. N. Muñoz-Sánchez, I. M. Hutchings, and A. A. Castrejón-Pita, "Droplet impact onto moving liquids", J. Fluid Mech. **809**, 716–725 (2016).

[40] M. Cheng and J. Lou, "A numerical study on splash of oblique drop impact on wet walls", Comput. Fluids **115**, 11–24 (2015).

[41] P. Brambilla and A. Guardone, "Automatic tracking of corona propagation in three-dimensional simulations of non-normal drop impact on a liquid film", Computing **95**, 415–424 (2013).

[42] B. Ray, G. Biswas, and A. Sharma, "Oblique drop impact on deep and shallow liquid", Commun. Comput. Phys. **11**, 1386–1396 (2012).

[43] C. W. Visser, P. E. Frommhold, S. Wildeman, R. Mettin, D. Lohse, and C. Sun, "Dynamics of high-speed micro-drop impact: numerical simulations and experiments at frame-to-frame times below 100 ns", Soft Matter **11**, 1708–1722 (2015).

[44] A. Worthington, *A study of splashes* (Longmans, Green, and Co.) (1908).

[45] C. D. Stow and M. G. Hadfield, "An experimental investigation of fluid flow resulting from the impact of a water drop with an unyielding dry surface", P. Roy. Soc. Lond. A. Mat. **373**, 419–441 (1981).

[46] M. Le Merrer, C. Clanet, D. Quéré, E. Raphaël, and F. Chevy, "Wave drag on floating bodies", P. Natl. Acad. Sci. **108**, 15064–15068 (2011).

[47] U. Schnars and W. Jüptner, "Digital recording and numerical reconstruction of holograms", Meas. Sci. Technol. **13**, R85–R101 (2002).

3

Solidification during tin drop impact *

The dynamics of drop impact can be changed considerably when solidification occurs due to contact with the substrate. Here, we experimentally study tin drop impact onto a sapphire substrate of controlled temperature. By combining side and bottom-view images of the impacting drops, we measure the maximum drop spreading and determine the number of ligaments formed at the outer edge of the drop for various substrate temperatures. We find that the maximum drop spreading decreases when the drop solidifies during the impact and model this process quantitatively. Moreover, solidification is found to strongly decrease the number of ligaments formed, which we attribute to solidification of the early-time ejecta sheet. Beyond that, we also show how the splashing threshold is affected by the liquid solidification.

3.1 Introduction

Drop impact onto a substrate with a temperature below the freezing temperature of the liquid is encountered in many applications. Perhaps most importantly, precise solid structures can be fabricated with three-dimensional (3D) printing of liquid metal drops, which solidify after impact [1, 2]. Another example is thermal spray coating, where a uniform metal coating is applied to surface [3]. Here, it is important to know how solidification alters the drop spreading and the splashing threshold during impact. Next to the direct application of solidifying drops, drop solidification is also relevant

*To be submitted as: "Solidification during tin drop impact", M.V. Gielen, R. de Ruiter, R.B.J. Koldeweij, D. Lohse, J.H. Snoeijer and H. Gelderblom.

for airplanes, transmission lines, or wind turbines under solidification conditions, as due to solidification impacting rain drops decrease the efficiency. For air planes, anti-icing surfaces prevent the drop to freeze after impact by minimizing the contact time of the drop with the substrate or delaying solidification inside the drop [4–6].

The reason why solidification during drop impact is a challenging phenomenon lies in the combination of the drop deformation dynamics [7, 8] with simultaneous heat transfer and phase transition [9–14]. In the following, we will briefly discuss what had been done on the individual phenomena, namely isothermal spreading after impact, solidification in spreading drops, isothermal drop splashing, and solidification during drop splashing.

Isothermal spreading has been studied extensively, see e.g. [7, 8, 15, 16]. A theoretical criterion for isothermal maximum spreading has been derived [8], where the drop arrests once its thickness equals the thickness of the viscous boundary layer. However, solidification has not yet been included in this arrest criterion.

Solidification in spreading drops after deposition (zero impact velocity) has been studied both experimentally and theoretically [17–20]. A successful model [17] invokes the kinetic undercooling of the contact line, where the drop stops spreading abruptly when the liquid at the contact line reaches a critical temperature. It remains to be tested whether this model holds for drops with a finite impact velocity. Few studies considered drop impact onto cold substrates [9, 13, 14, 21, 22]. Solidification was shown to decrease the drops maximum spreading. This limited spreading is explained by a loss of kinetic energy in the solidified liquid [9–11]. However, a systematic and quantitative comparison of these models to experimental data is lacking.

Drop splashing under isothermal conditions has been studied extensively (see e.g. [23–29]). Several substrate properties have been shown to influence splashing behavior. The substrate's roughness or structure can either suppress or promote splashing in a specific direction [30–32]. The substrate's (visco-)elasticity can be used to suppress splashing [33–35]. On cold substrates where the liquid solidifies during impact one would also expect splashing to be suppressed. However, experimental studies report that solidification actually promotes splashing [10–12, 21, 22, 36]. A solidified layer is thought to obstruct the radially outwards flowing liquid and therefore trigger *freezing-induced* splashing. Several studies [11, 12, 36] used (plasma-)sprayed drops to study the splashing threshold. For these sprayed drops it is difficult to obtain a controlled range of sizes and velocities where single drop impact events can be studied. However, the development of a drop-on-demand system that generates single drops that solidify and splash during impact is challenging. As a result, there is no quantitative study on the splashing threshold for solidifying drops.

Here, we experimentally study tin drop impact onto a sapphire substrate of various temperatures below the melting point of tin. In Sec. 3.2 we present a setup to generate isolated liquid tin drops with a controlled impact velocity and size that allows for

simultaneous side and bottom-view imaging. The outcome of a typical experiment is described in Sec. 3.3. We quantify the maximum drop spreading as a function of substrate temperature and present a model to explain our findings in Sec. 3.4.1. Our bottom view experiments reveal the growth of ligaments over time. We measure the number of ligaments as a function of substrate temperature and explain our results in Sec. 3.4.2. We quantitatively determine the splashing threshold of the impacting drops as a function of substrate temperature in Sec. 3.4.3. This chapter closes with a discussion in Sec. 3.5.

3.2 Experimental method

To study the influence of the substrate temperature on the impact dynamics, we let tin drops impact onto a sapphire substrate of which the temperature is controlled. To create isolated liquid metal drops in a controlled way we adopted a similar method as in Refs. [37, 38]. An overview of the entire setup to generate single liquid tin drops on demand is shown in Fig. 3.1.

Drops of size of 1.7 ± 0.16 mm or 2.0 ± 0.43 mm were generated by heating the reservoir containing the tin to $T = 250^{\circ}$C, which is well above the melting temperature of tin ($T_m = 232^{\circ}$C). We used 99.9% pure tin with density $\rho = 7.0 \cdot 10^3$ kg/m^3, surface tension $\gamma = 0.54$ N/m, and kinematic viscosity $\nu = 2.6 \cdot 10^{-7}$ m^2/s. Thermal properties of the tin are its specific heat $c_p = 2.3 \cdot 10^2$ J/(kgK), its latent heat $L = 5.9 \cdot 10^4$ J/kg, its thermal diffusivity $\kappa = 2.0 \cdot 10^{-5}$ m^2/s and its thermal conductivity $k = c_p \rho \kappa = 31$ W/(mK). The bottom of the reservoir is tapered to allow smooth connection to the needle (Hamilton, custom made, stainless steel, $\varnothing$ 0.71 and 1.14 mm). The reservoir is mounted on a movable stage of one meter that allows to change the impact height and thereby the impact velocity of the drop between 0.5 m/s $< U <$ 5.5 m/s.

The pressure inside the reservoir was controlled by pressure controllers that are situated one meter above the liquid tin reservoir. In this way the pressure controllers remained at room temperature (working temperature) while the tin in the reservoir can be melted. To prevent leakage of the molten tin under the effect of gravity the reservoir was maintained at an underpressure of $p \approx 45$ mbar. To generate a tin drop the underpressure was replaced by a short pressure pulse of 340 mbar (pulse duration between 0.06 s $< \Delta t <$ 0.09 s depending on height of the tin in the reservoir). The pressure pulse is longer as compared to Refs. [37, 38] due to the one meter connection between the pressure controller and the tin reservoir.

To prevent oxidation of the liquid tin drop during its fall, the entire setup was contained in a closed box. The box was filled with nitrogen gas at a slight overpressure to prevent oxygen leaks. During heating the setup was flushed with nitrogen while during operation the flow was lowered to minimize disturbances to the impacting drop. The temperature of this box was controlled at $T = 250^{\circ}$C to prevent cooling down of

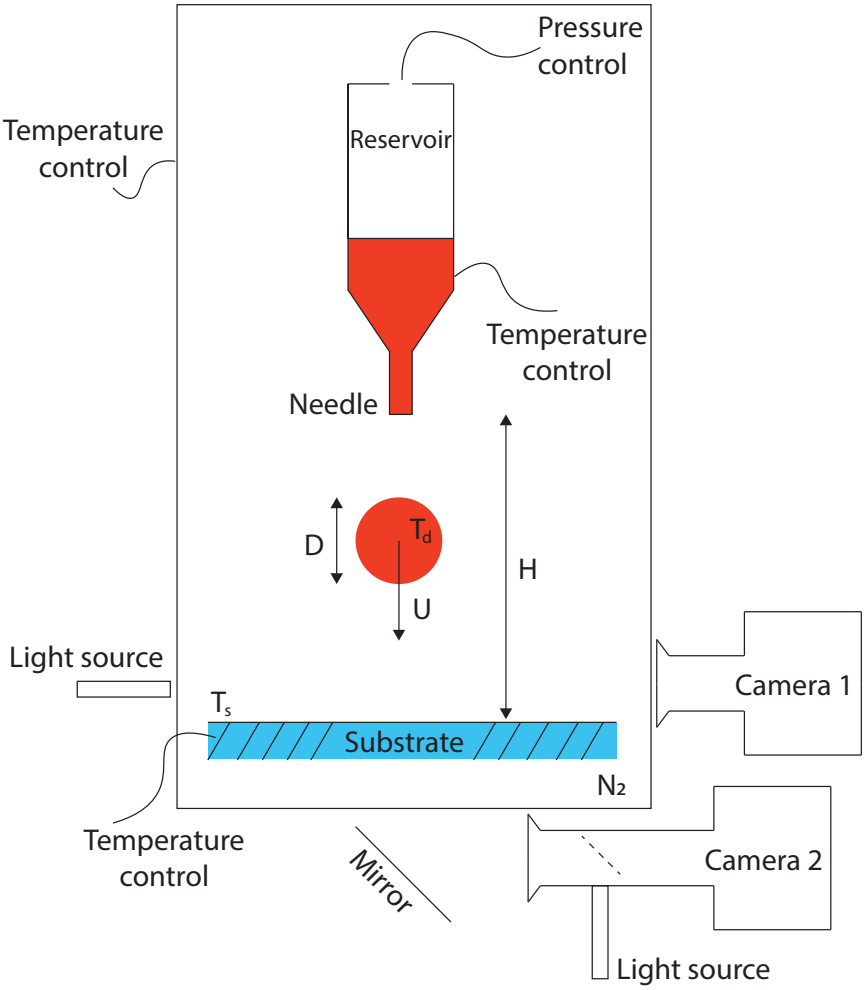

Figure 3.1: Schematic view of the drop impact setup. Tin was put in a reservoir and is heated to 250°C. When the tin melted, it filled a needle from which the drops were generated. The pressure inside the reservoir was controlled: It was kept at a slight underpressure to prevent the tin from leaking out. To generate a drop a short, large pressure pulse was given. The drop fell down under the influence of gravity. By changing the needle height H, the impact velocity was varied in the range 0.5 m/s $< U <$ 5.5 m/s. The temperature of the sapphire substrate T_s was controlled between 40°C and 250°C. The substrate and the tin reservoir were placed within a closed box, where a nitrogen environment was created to avoid oxidation and the temperature was controlled at 250°C.

the drop during its fall.

At the bottom of the closed box a sapphire substrate (thickness $h = 3$ mm, thermal conductivity k = 24 W/(mK)) was placed inside a temperature-controlled holder. We waited for ten minutes after placing the substrate inside the setup to assure the temperature at the interface is the same as the temperature of the substrate heater, as observed from our temperature measurements. No temperature measurements were performed during impact. The center of the metal holder is open to allow for bottom-view measurements. The substrate temperature was varied between 40°C $< T_s <$ 250°C, such that the influence of the substrate temperature on the drop impact can be compared to isothermal conditions.

We measured the outcome of the impact using high-speed imaging from the side and from below. The side-view images (Camera 1 in Fig. 3.1, Photron SA1.1, 30,000 fps) were taken with back light illumination (Sumita LS-M352A) and the bottom-view images (Camera 2 in Fig. 3.1, Photron SA-X2, 30,000 fps) were generated with coaxial illumination (Asahi MAX-303). Both cameras were synchronized to the pressure pulse that generates the drop with a delay of 0.4 seconds.

In the experiments drop diameter D, impact velocity U, and substrate temperature T_s can be varied. In dimensionless form the control parameters are the Reynolds number Re = UD/ν, Weber number We = $\rho DU^2/\gamma$, and Péclet number Pe = UD/κ based on the drop properties, and the Stefan number Ste = $c_p(T_m - T_s)/L$ based on the drop thermal properties and the substrate temperature T_s. Our goal was to measure the dimensionless drop spreading $\xi = D_s/D$ over time from the bottom-view images, with D_s the spreading diameter of the drop, and to identify the critical impact conditions for splashing as a function of the dimensionless substrate temperature Ste from the side-view images.

3.3 Typical experiments

Figure 3.2 shows the time series of three impacting drops at similar We onto a sapphire substrate of varying temperature ($T_s = 249$°C, 150°C and 39°C). The top row images show the drop impact event in side view, the bottom row images in bottom view. The bottom-view images reveal interesting aspects of the impact event that cannot be observed from side-view images. Before impact ((*i*) in Fig. 3.2(a), (b) and (c)) the drop is not visible from below, since there is no contact with the substrate.

During isothermal impact (Fig. 3.2(a)) we observe that the drop spreads smoothly over the substrate at early times (*ii*). As time evolves ligaments become visible (*iii*) and grow until the drop reaches its maximum spreading (*iv*). Since the static contact angle of tin with the sapphire substrate is about 130° (as measured by side-view imaging of a deposited drop), the drop retracts after maximum spreading and part of the drop bounces off the substrate while small droplets detach (*v*).

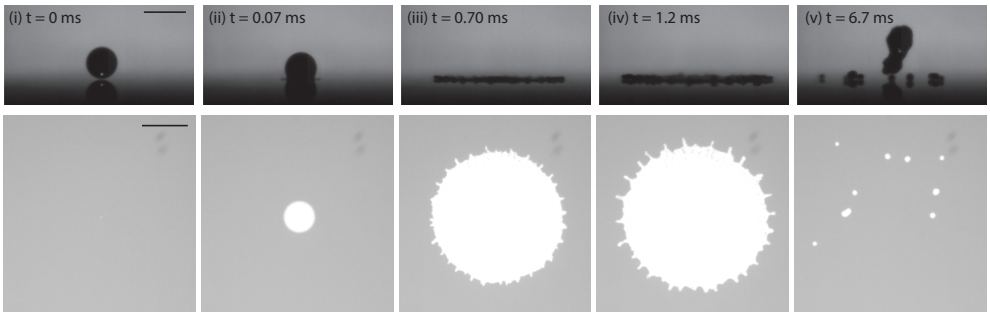

(a)

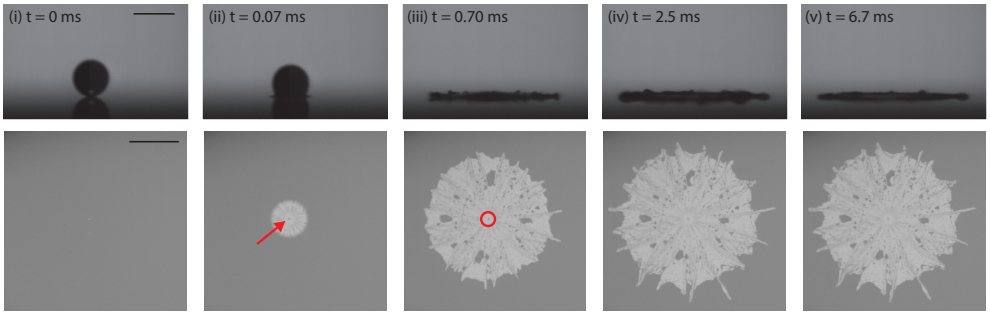

(b)

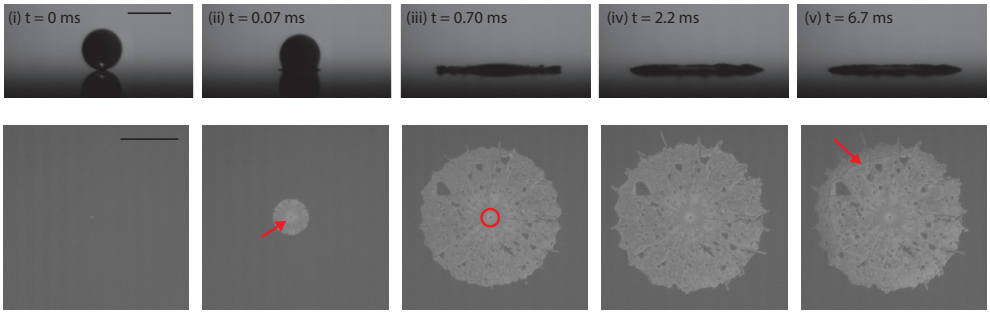

(c)

Figure 3.2: Time series of drop impact onto a sapphire substrate of different substrate temperature. (a) We =310, $T_s = 249°C$ (b) We = 267, $T_s = 150°C$, and (c) We = 278, $T_s = 39°C$. The top rows show side-view images recorded by camera 1, the bottom rows bottom-view images taken with camera 2 (see Fig. 3.1). The scale bar in each row represents 2 mm. The drop is shown just before impact (*i*) and spreads over the surface in time (*ii* and *iii*) until it reaches its maximum spreading in frame *iv* and retracts or remains solidified at the substrate (*v*).

We now lower the substrate temperature to $T_s = 150°C$ (Fig. 3.2(b)), which is below the melting temperature of tin. During the impact the variations in grayscale below the impacting drop show the solidified structures at the substrate. Directly after impact (*ii*), a gray spot is visible at the impact center of the drop (red arrow), which is the center air bubble that is entrapped during impact [39]. This spot remains visible since the surrounding tin solidifies after contact with the substrate. When the drop spreads further radially outwards moving stripes become visible. These stripes are visible starting from the defect distance D_d [40], which is indicated by the red circle in (*iii*). The stripes then grow into ligaments, which are clearly visible at maximum spreading (*iv*). Both the number of ligaments and the drop's spreading are reduced as compared to isothermal impact (Fig. 3.2(a)). As time progresses (*v*) the bulk of the drop solidifies. As the drop stays attached to the substrate the bottom-view image no longer changes over time. At some locations there are dark gray spots visible in the imprint of the spreading drop. At these locations the liquid tin is hindered by imperfections at the substrate during the spreading, which results in the entrapment of air pockets. Due to solidification of the surrounding tin most of these air pockets remain visible at the final splat (*v*), while some have disappeared.

For a further decrease of substrate temperature ($T_s = 39°C$, Fig. 3.2(c)) we again observe the air bubble entrapped at early times of impact in the solidified splat (red arrow in (*ii*)) and the defect distance as indicated by the red circle in (*iii*). Again, the observed ligaments can be traced all the way back to the defect distance (*iv*). Their number is lower than at isothermal impact (Fig. 3.2(a)), but comparable to the experiment shown in Fig. 3.2(b). The drop spreading is even smaller than the one in Fig. 3.2(b). Moreover, at later times an inward moving front is observed from bottom-view images (red arrow in (*v*)). This is a peeling front where the drop detaches from the substrate. This peeling is a consequence of the stresses in the quickly solidifying drop, which make the drop bend away from the substrate. This bending of the drop is called self-peeling [40]. Indeed, the splat of the drops that show this self-peeling is much easier to remove from the substrate after the experiment than a splat without self-peeling.

Splats of drops that peel off the substrate were evaluated under the microscope. An example of a microscope image is shown in Fig. 3.3(a). Since for this experiment We is small (We = 135) as compared to Fig. 3.2 no radially moving outwards structures and ligaments are observed. We do see a clear wavelength of undulations that might grow into ligaments once We is higher. At the impact center a black spot is visible, which is the air bubble entrapped directly after impact. At small spreading distances a light area (white circle) is observed where no structures are visible: the defect distance D_d. Outside this area a pattern of circular rings is observed. These circular rings are called air ridges [40]: Solidification stops the contact line from moving while the bulk liquid tin spreads further over the substrate. During this renewed contact of the liquid

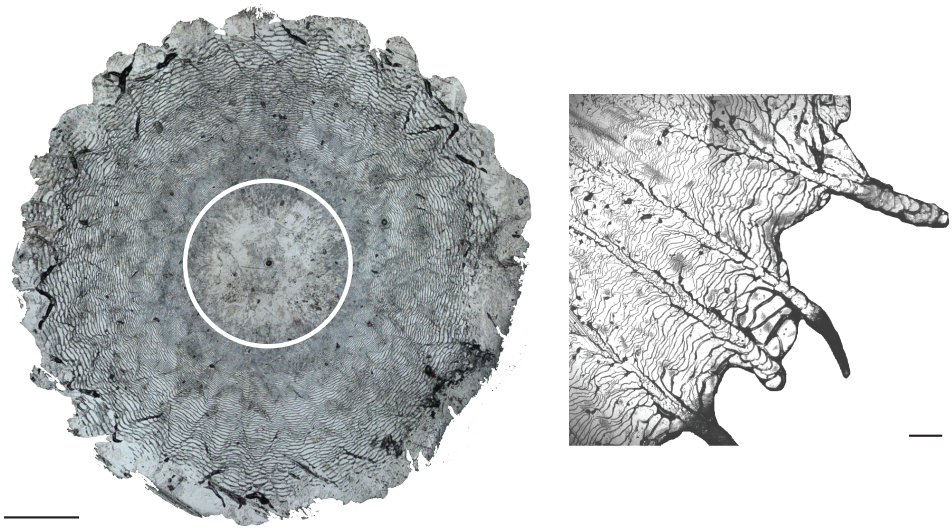

(a) (b)

Figure 3.3: Microscopic image of the solidified splat of a tin drop that has impacted onto a sapphire substrate with (a) 5× magnification, We = 135 and $T_s \approx 50^\circ$C and (b) 4× magnification, We = 448 and $T_s = 150^\circ$C. (a) The scale bar represents 0.5 mm. Around the impact center there is an area without structure. Further outwards, a pattern of circular rings is observed. The first circular rim is observed at $D_d/D \approx 0.7$ mm as indicated by the white circle. (b) The scale bar represents 2 mm. For impact at higher Weber number the circular rings are also observed. At such high Weber number also ligaments are formed, and a radial outward pointing stripe pattern is observed.

tin with the substrate air is trapped between the tin and the substrates forming the air ridge. At larger We, we observe similar circular structures (Fig. 3.3(b)). In addition, the radial stripe pattern and ligaments are visible.

3.4 Results and interpretation

Having seen that solidification strongly influences the outcome of an impact event, we now quantify and explain how solidification alters the spreading, the formation of ligaments and splashing of drops during impact. In Sec. 3.4.1 we use the bottom-view images to focus on the spreading dynamics and determine the maximum spreading as function of Pe and T_s. In Sec. 3.4.2 we present a model where we show how the substrate temperature affects the formation of ligaments and analyze the number of ligaments as a function of We. The splashing threshold as function of substrate

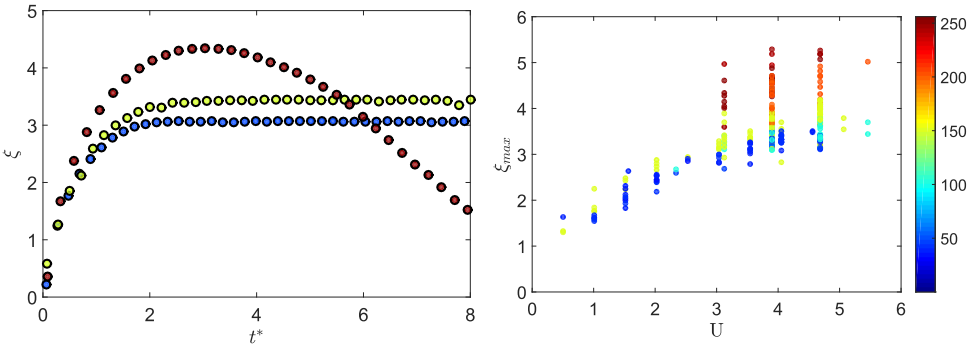

Figure 3.4: (a) Plot of the dimensionless spreading $\xi = D_s/D$ of the drop as function of time $t^* = t/(D/U)$ for different substrate temperatures for We = 278, $T_s = 39°C$ (blue dots), We = 267, $T_s = 150°C$ (yellow dots) and We = 310, $T_s = 249°C$ (red dots). For clarity, only one every three data points is shown. For $T_s = 249°C$, we observe retraction of the drop, which means that ξ decreases after the maximum is reached. For $T_s = 150°C$ and $T_s = 39°C$, the drop solidifies during the expansion phase and does not retract, such that ξ remains at its maximum value. For decreasing substrate temperature, this maximum spread decreases. (b) Plot of the maximum spreading $\xi_{max} = D_{max}/D$ as function of impact velocity U for different T_s (color bar). The maximum spreading increases with increasing U and T_s.

temperature is evaluated in Sec. 3.4.3.

3.4.1 Drop spreading

We study the spreading of a drop onto a sapphire substrate by systematically varying the impact velocity and the substrate temperature. We measure the spreading of the drop in time using the bottom-view images (bottom row in Fig. 3.2) from which we determine the equivalent diameter of the area occupied by the spreading drop. Figure 3.4(a) shows the dimensionless spreading diameter $\xi = D_s/D$ of three drops on a sapphire substrate of different substrate temperature over time $t^* = t/(D/U)$. At early times ($t^* \ll 1$), all drops follow the isothermal spreading curve. The exact moment of deviation from isothermal spreading depends on the substrate temperature. In contrast to what has been reported for gently deposited drops [17], this deviation from isothermal spreading is not abrupt: The spreading first slows down before the drop comes to rest. For lower substrate temperatures the deviation starts earlier and a smaller maximum spreading is reached. When the drop solidifies during impact, no retraction is observed, which means that the maximum spreading is reached during the expansion phase of the drop.

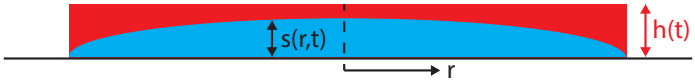

Figure 3.5: Schematic view of the growth of the solidification layer inside the spreading drop at arrest. The thickness of the solidified layer s (in blue) reaches the thickness of the liquid spreading drop h (in red). The drop is assumed to have a pancake-shape. While the pancake spreads the solidified layer starts growing after the drop comes into contact with the substrate. As this occurs at a different time for different radial positions the solidified layer assumes a radial dependent shape $s(r,t)$. When $s(0,t) = h(t)$ the drop stops spreading.

The curves of Fig. 3.4(a) allow us to extract $\xi_{max} = D_{max}/D$, with D_{max} the maximum spreading diameter. Figure 3.4(b) shows ξ_{max} as function of the impact velocity U for different substrate temperatures. For increasing U we observe an increase of ξ_{max}. A decrease of substrate temperature results in a decrease of the maximum spreading. For example, for a drop with $U \approx 4.6$ m/s the maximum spreading ranges from $\xi_{max} = 5.2$ (isothermal) to $\xi_{max} = 3.1$ ($T_s \approx 50°$C).

To explain the behavior observed in Fig. 3.4(b), we now develop a model for the maximum spreading that accounts for the influence of solidification. Isothermal spreading upon impact has succesfully been modeled by assuming that arrest occurs when the growing viscous boundary layer reaches the thickness of the spreading drop [8]. In this spirit, we assume that for solidification-limited spreading the drop arrests when the solidified layer that grows from the bottom of the drop reaches the thickness of the spreading drop, as shown schematically in Fig. 3.5.

The first step is to determine the time at which the spreading arrests. We start by noting that in our experiments arrest occurs during the isothermal expansion phase on a time $t_{max} \sim D/U$. On this time, the drop shape can be approximated by a pancake [8] of uniform thickness h, see Fig. 3.5. From mass conservation it follows that

$$h^* = \frac{h}{D} \sim \left(\frac{D}{D_s}\right)^2. \tag{3.1}$$

As solidification-limited arrest occurs at early times, i.e. before the viscous boundary layer has grown to a considerable thickness, the pancake dynamics can be described by the axisymmetric Euler equation [41]. In the thin-sheet approximation mass and momentum conservation then read

$$r\frac{\partial h}{\partial t} + \frac{\partial}{\partial r}(ruh) = 0, \tag{3.2a}$$

$$\frac{\partial u}{\partial t} + u\frac{\partial u}{\partial r} = -\frac{1}{\rho}\frac{\partial p}{\partial r}, \tag{3.2b}$$

with r the radial coordinate, u the radial velocity, and p the pressure in the pancake. Upon integration of Eq. (3.2a) and by using Eq. (3.1), we find $u = r\dot{D}_s/D_s$. As we expect surface tension to have a negligible effect on the spreading dynamics since $t_{max}/t_c \sim \mathrm{We}^{-1/2} \ll 1$ with $t_c = \sqrt{\rho D^3/\gamma}$ the capillary time scale, we assume $\partial p/\partial r = 0$. Equation (3.2b) then reduces to $\ddot{D}_s = 0$, i.e. $D_s/D \sim t^*$. From Eq. (3.1) we then find the early-time spreading dynamics of the pancake to be given by

$$h^* \sim t^{*-2}. \tag{3.3}$$

The next step is to describe the thickness of the solidified layer and to equate it to the thickness of the pancake from Eq. (3.3) to find the time of arrest. We assume that a one-dimensional (1D) solidification front grows from the bottom of the drop after the drop makes contact with the substrate. The thickness of this solidified layer [42, p.185-188] in the center is given by (see App. 3.A)

$$s^* = \frac{s}{D} \sim \sqrt{t^* \frac{\mathrm{Ste}}{\mathrm{Pe}}}. \tag{3.4}$$

In Fig. 3.5 the growth of the solidified layer is shown schematically. Solidification starts as soon as the liquid contacts the substrate. As a result, the thickness of the solidified layer varies over the radial distance from the impact center: Since the drop diameter increases linearly in time, the solidified layer will show a square-root radial dependency, i.e. $s^* \sim (D_s - r)^{1/2}$.

We assume that for solidification-limited spreading arrest occurs when $h^* = s^*$, which gives

$$t^*_{max} \sim \left(\frac{\mathrm{Pe}}{\mathrm{Ste}}\right)^{1/5}. \tag{3.5}$$

From Eq. (3.3) we find that $\xi = D_s/D \sim t^*$, thus $\xi_{max} \sim t^*_{max}$, and hence, using Eq. (3.5),

$$\xi_{max} \sim \left(\frac{\mathrm{Pe}}{\mathrm{Ste}}\right)^{1/5}. \tag{3.6}$$

Eq. (3.6) is valid as long as the spreading is solidification-limited and s^* is larger than the boundary layer thickness $\delta^* = \delta/D \sim \sqrt{t^*/\mathrm{Re}}$, which means that $\mathrm{Ste/Pr} > 1$ with $\mathrm{Pr} = \nu/\kappa$ the Prandtl number. For our experiments $\mathrm{Ste/Pr} \gtrsim 10$, which means that the spreading is indeed solidification limited and Eq. (3.6) can be used to describe the maximum spreading. Furthermore, as the arrest occurs at early times $t_{max} \ll t_c$, surface tension also has a negligible influence on the maximum spreading.

When no solidification occurs ($T_s > T_m$) the drop spreads isothermally. In that case, the maximum spreading has been previously addressed in detail [16]. The importance of viscosity and surface tension is described by the impact parameter $P = \mathrm{WeRe}^{-2/5}$. In our isothermal experiments $P = \mathcal{O}(1)$, such that both surface tension and viscosity

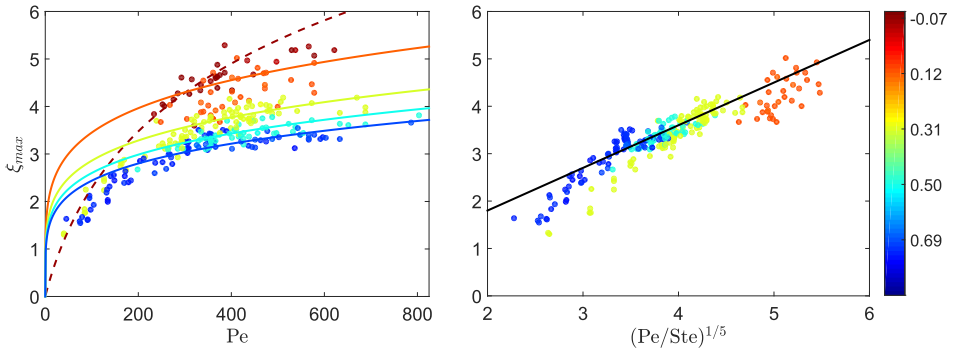

Figure 3.6: (a) Dimensionless plot of the maximum drop spreading ξ_{max} as function of Pe for different Ste (color bar). The solid lines give the expected maximum spreading from Eq. (3.6) with prefactor 0.9. The maximum spreading for the isothermal experiments (dashed line) is given by Eq. (3.7) with prefactor 0.9. (b) Dimensionless plot of the maximum drop spreading as function of $(\mathrm{Pe}/\mathrm{Ste})^{1/5}$ for $\mathrm{Ste} > 0$ for different Ste (color bar). The solid line corresponds to Eq. (3.6) with prefactor 0.9.

control the maximum drop spreading. For this transition regime a scaling for the maximum spreading has been suggested [16]

$$\xi_{max} \sim \frac{P^{1/2}}{A + P^{1/2}} \mathrm{Re}^{1/5}, \tag{3.7}$$

with $A = 1.24$ a fitting constant.

Figure 3.6(a) shows our measurements in dimensionless form where U is non-dimensionalized using $\mathrm{Pe} = UD/\kappa$. For different Ste, the predictions of Eqs. (3.6) and (3.7) are plotted together with our measurements. The isothermal experiments ($\mathrm{Ste} \leq 0$) show good agreement with Eq. (3.7) using a prefactor of 0.9, while in [16] a prefactor unity is used. This small discrepancy originates from the fact that we assess the spreading diameter from our bottom-view images where we can correct for the length of the ligaments and measure the equivalent area covered by the spreading drop.

When the drop solidifies during impact our model of Eq. (3.6) shows good agreement with prefactor 0.9 for all Ste. At low Pe ($\mathrm{Pe} \lesssim 110$) there is a regime where the modeled isothermal maximum spreading (Eq. (3.7)) is smaller than the maximum spreading model where solidification is taken into account (Eq. (3.6)) for all Ste. In this regime the maximum spreading is not solidification-limited, but the combined effect of surface tension and viscosity determines the maximum drop spreading and the data follows Eq. (3.7). In Fig. 3.6(b) we show that we can collapse all solidified-limited data of Fig. 3.6(a) onto a single master curve by using the rescaling in terms of Pe and Ste, which is well described by the scaling law of Eq. (3.6).

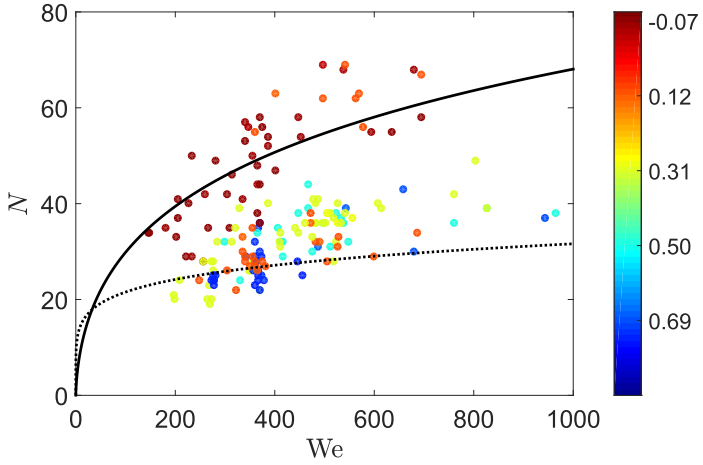

Figure 3.7: Number of ligaments N as function of We for different Ste (color bar). The solid line shows the expected number of ligaments according to Eq. (3.11) with a prefactor of 4.25. The dashed line shows the expected number of ligaments when solidification is taken into account as given by Eq. (3.14) with prefactor 10. For We $\lesssim$ 150, no ligaments are observed.

3.4.2 Number of ligaments

As the rim decelerates over time, corrugations at the rim get amplified by the Rayleigh-Taylor instability [43]. In addition, a capillary (Rayleigh-Plateau) instability of the same wavenumber [43] develops at the rim. As the corrugations grow they develop into ligaments from which secondary droplets may detach. In Fig. 3.2 we observe that solidification has a strong influence on the development of these ligaments, as was also observed in Ref. [21]. In contrast to [21], the bottom-view images allow us to follow the growth of the ligaments over time. In particular, for the solidified drops ligaments seem to evolve from the early-stage stripe pattern as discussed in Sec. 3.3. By contrast, for isothermal impact the ligaments evolve from the rim and become apparent only at later stages of spreading (compare Fig. 3.2(a),(*iv*) with Fig. 3.2(c),(*ii*)).

To interpret these observations we manually count the number of ligaments N as a function of We for different substrate temperatures as shown in Fig. 3.7. For We $\lesssim$ 150 no ligaments are observed as the impact is not violent enough to trigger an instability. For larger We, the number of ligaments N increases with increasing We, where N increases much steeper for isothermal impact than for solidification-limited impact: N (almost) doubles when we compare isothermal impact (Ste ≤ 0) and impact onto the coldest substrate used (Ste = 0.69).

We now propose a model to explain the spreading in the data points of N in

2 clouds. For isothermal impact, destabilization of the outer rim is observed at relatively long time scales after impact ($t^* \approx 2$, see Fig. 3.2(a)). At impact events with solidification the ligaments also become visible at relatively long time scales, but the origin of these ligaments can be traced back to times shortly after impact by following the imprint of the radially outward pointing stripes (see Fig. 3.2(b) and (c)). We hypothesize that on cold substrates early-time destabilizations of the fast ejecta sheet are immediately solidified. Therefore, they set a solidified pattern over which the remaining liquid flows, forming the radial stripes on which the ligaments formed by the rim eventually evolve.

To describe these two branches, we first revisit the model for rim destabilization derived by Villermaux and Bossa for impact onto a pillar [43]. We then modify this model to account for the early-time destabilizations and solidification of the ejecta sheet. During spreading the rim located at D_s moves outwards. For our model we assume that the expulsion of ligaments at the rim is due to a Rayleigh-Taylor mechanism. The number of ligaments then depends on the wavenumber of the fastest growing mode k, which scales as

$$k \sim \sqrt{\frac{-\ddot{D}_s \rho}{\gamma}}, \tag{3.8}$$

with $\ddot{D}_s$ the deceleration of the rim. The number of ligaments is then obtained from Eq. (3.8) and the diameter of the spreading drop on which the corrugations grow:

$$N \sim k D_s. \tag{3.9}$$

For isothermal impact, the corrugations become visible close to maximum spreading [43]. Here we approximate $\ddot{D}_s \sim -D_{max}/t_c^2$ such that

$$k \sim \sqrt{\frac{D_{max}}{D^3}}, \tag{3.10}$$

where D_{max} is given by Eq. (3.7). In our case, D_{max} is given by Eq. (3.7), which is different from Villermaux and Bossa [43], where inviscid impact onto a pillar was considered. By combining Eqs. (3.9) and (3.10) we find the number of ligaments to be

$$N \sim \left(\frac{A + P^{1/2}}{P^{1/2}} \mathrm{Re}^{1/5} \right)^{3/2}. \tag{3.11}$$

This scaling is shown in Fig. 3.7 as the solid line and shows good agreement with the isothermal data with prefactor 4.25.

When solidification becomes important, we re-evaluate Eqs. (3.8) and (3.9) using the deceleration of the ejecta sheet $\ddot{D}_e$ instead of the outer rim. To this end we use the model for the ejecta sheet dynamics by Riboux and Gordillo [29]:

$$D_e \sim D\sqrt{t_e}, \tag{3.12}$$

with $t_e = \tilde{t_e} D/U$ the dimensionless time of sheet ejection and $\tilde{t_e}$ the time of sheet ejection. In the limit for Re/We $\gg 1$ (here Re/We > 55) the dimensionless time of sheet ejection scales as $t_e \sim \mathrm{We}^{-2/3}$ [29], which gives

$$\frac{D_e}{D} \sim \mathrm{We}^{-1/3} \tag{3.13a}$$

$$\frac{\ddot{D}_e}{D} \sim -\mathrm{We}. \tag{3.13b}$$

The fastest growing wavenumber is now calculated from Eqs. (3.8) and (3.13b). This result combined with $N \sim kD_e$ and (3.13a) sets the number of ligaments:

$$N \sim \mathrm{We}^{1/6}, \tag{3.14}$$

This weak dependence on We is confirmed by our experimental data (see Fig. 3.7). Eq. (3.14) predicts the minimum number of ligaments well for solidifying drops with prefactor 10.

To support our hypothesis that the ligaments may grow from the corrugation at the solidifying ejecta sheet we check if the time needed to solidify the ejecta sheet is indeed shorter than the time at which the rim corrugations develop. In analogy to Sec. 3.4.1 we assume that the ejecta sheet solidifies if $s^* = h_e^*$, with s^* the thickness of the solidified layer (Eq. (3.4)) and h_e^* the thickness of the ejecta sheet. From [29] it is found that $h_e^* \sim t_e^{3/2}$ and $t_e \sim \mathrm{We}^{-2/3}$ as used before, which gives

$$h_e^* \sim \mathrm{We}^{-1}. \tag{3.15}$$

From Eqs. (3.4), (3.15) we then find the time scale to solidify the ejecta sheet

$$t_s^* \sim \frac{\mathrm{Pe}}{\mathrm{Ste}\ \mathrm{We}^2} \tag{3.16}$$

Rim stabilities develop at time scales of $t_c^* \sim \sqrt{\mathrm{We}}$. Therefore, the ejecta sheet can solidify before rim corrugations are developed when

$$\frac{t_s^*}{t_c^*} \ll \frac{\mathrm{Pe}}{\mathrm{Ste}\ \mathrm{We}^{5/2}}. \tag{3.17}$$

Indeed, for $t_s^*/t_c^* \ll 1$ the ejecta sheet solidifies way before the rim corrugations develop, such that the solidified ejecta sheet controls the number of ligaments, which then follows Eq. (3.14). On the other hand, when $t_s^*/t_c^* \gg 1$ the ejecta sheet cannot solidify before the rim corrugations develop and Eq. (3.11) holds. For our experiments with Ste > 0, $t_s^*/t_c^* \sim \mathcal{O}(10^{-3})$ so the ejecta sheet rapidly solidifies and therefore N can be determined from corrugations at the ejecta sheet.

The models for the number of ligaments in Eqs. (3.11) and (3.14) give limiting values for our measurements. The isothermal model (Eq. (3.11)) gives the upper limit which is in good agreement with our measurements. The model accounting for the solidifying ejecta sheet (Eq. (3.14)) gives the lower limit. For most impacting drop the actual number of ligaments is above this lower limit. While the minimum number of ligaments is set during early time scale, new ligaments can form next to the early-time corrugations therefore altering the total number of ligaments. For drop impacts Pe $\gtrsim$ 400 (i.e. at high impact velocity) and substrate temperature slightly below T_m (Ste = 0.12) we observe that the number of ligaments follows the isothermal scaling. In that case, the late-time corrugations grow over the ejecta sheet corrugations and N follows the isothermal scaling.

3.4.3 Splashing threshold

The ligaments formed may destabilize, which results in secondary droplet generation, i.e. splashing. When no secondary droplets are created the drop is said to deposit when it adheres to the substrate and to bounce when (part of) the drop lifts off from the substrate. In Fig. 3.8(a) we quantify the outcome of an impact event for different substrate temperatures and impact conditions. For the isothermal impact events ($T_s = 250°$C) and low We the drop bounces. For We > 400 splashing is observed. There is a small transition regime, which is a range of We where both bouncing and splashing are observed. When the substrate temperature is below the melting temperature of tin we do not observe bouncing at low impact velocities but deposition: The drop sticks to the substrate. The width of the transition region increases for increasing substrate temperature. Splashing can be observed both at early times (Fig. 3.8(c)(*iii*)) and at late times (Fig. 3.8(c)(*iv*)), however in the data shown in Fig. 3.8(a) and (b) we do not distinguish between these types of splashing.

In Fig. 3.8(b) we show the Weber numbers corresponding to both the first splashing and the last deposition event as a function of Ste. On the one hand, the last deposition event increases rapidly with increasing Ste. For Ste > 0.3 we still observe both deposition and splashing events even at the highest We accessible by our setup. On the other hand, the first splashing event increases up to Ste ≈ 0.3, then decreases for increasing Ste. As a result, the transition regime increases for increasing Ste.

To explain the twofold splashing behavior (decreasing first splashing event, increasing last deposition event), we again invoke the early-time solidification of the ejecta sheet. First, the solidified ejecta forms corrugations at the substrate. These corrugations interact with instabilities developing on the rim and may trigger freezing-induced splashing [10–12]. This effect becomes more severe with increasing Ste (lower substrate temperatures). The occurrence of a freezing-induced splash will depend on the detailed interaction between the substrate, the solidified pattern formed by the ejecta sheet, and the corrugations developing at the rim. This type of splash-

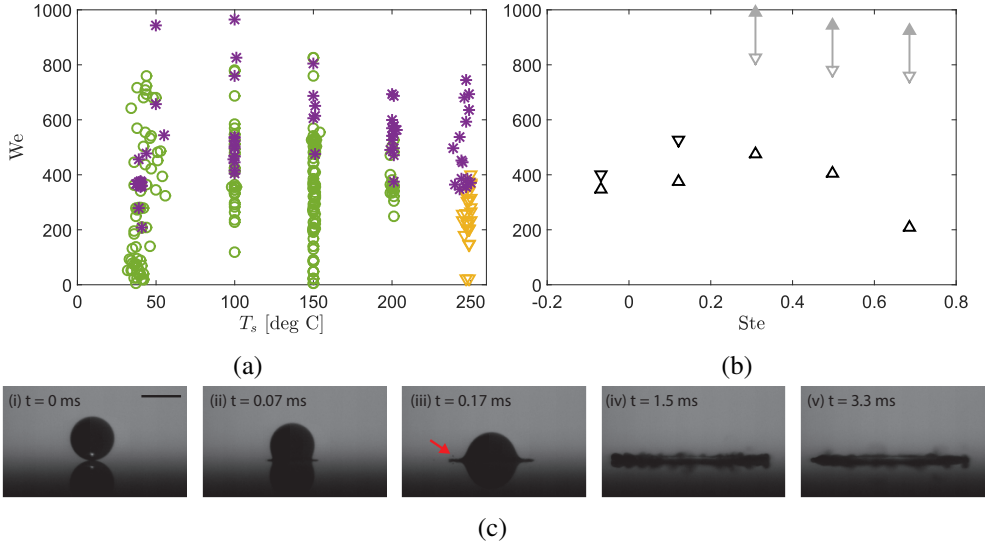

Figure 3.8: (a) Phase diagram showing the outcome of drop impact as function of We and T_s. The three impact behaviors observed are bouncing (orange triangles), deposition (green circles) and splashing (purple stars). (b) Plot of the first splashing event ($\triangle$) and last bouncing/deposition event ($\triangledown$) observed as function of We and Ste extracted from the data in Fig. 3.8(a). For isothermal impact (Ste ≤ 0) the transition to splashing is found at We ≈ 375. The threshold for the last deposition/bouncing event rapidly increases to We outside our measurement range, as marked by the gray symbols and arrows. (c) Side-view images of drop impact with We ≈ 370 and $T_s = 40°$C. Splashing is observed at different time scales: (1) From the ejecta sheet (indicated by the red arrow in (*iii*)) and (2) close to maximum spreading (*iv*).

ing therefore has a stochastic nature and is not observed for each single experiment. Second, in absence of a solidified pattern the drop will still splash at sufficiently high Weber number [23, 29]. On this type of splashing solidification is expected to have a suppressing influence: As part of the liquid solidifies during impact less kinetic energy remains in the drop for splashing. For increasing Ste the amount of energy lost in solidification increases, which explains the increase of the last deposition event with Ste.

3.5 Discussion and conclusion

We studied the influence of solidification on drop impact dynamics. Solidification was shown to strongly alter drop spreading, destabilization through the formation of ligaments, and splashing.

Using bottom-view imaging we recorded drop spreading curves. Drop spreading is already limited by solidification during the expansion phase, resulting in a lower maximum spreading. We described this reduced maximum spread by assuming that the drop arrests once the thickness of the solidification layer equals the thickness of the spreading drop. For the solidified layer growth a quasi-static one-dimensional model was used, where the contact resistance between the drop and the substrate was neglected. Our simple argument showed good agreement with experiments. Numerical simulations could be of added value to reveal the radial and longitudinal growth of the solidified layer over time, and provide a further test for the validity of the 1D model. Below, we reflect on other solidification models from literature and discuss their applicability to our data.

A frequently used criterion for maximum isothermal drop spreading is based on energy conservation arguments [44, 45]. In these models, solidification is included as an additional energy loss [9–11]. Our data is in reasonable agreement with these models. However, to estimate the energy loss by solidification a fixed arrest time $t^* = 8/3$ is used, independent of the substrate temperature. This assumption is in contradiction with our experimental observations (see Fig. 3.4(a)) where the gradual deviation from isothermal spreading sets in earlier for colder substrates.

In a previous study [17] of drop spreading during deposition (i.e. with zero impact velocity) kinetic undercooling effects were used to obtain a criterion for contact line arrest. In that work, the entire drop is assumed to stop spreading abruptly, as soon as the velocity of the contact line is lower than the velocity of the solidification front. For arrest to occur during the early-time inertial spreading phase, the rapidly moving contact line has to be at a temperature lower than the bulk solidification temperature. For impacting drops the contact line moves even faster. One might therefore expect a similar arrest condition to apply. However, in our spreading curves we observed gradual deviations from isothermal spreading before the drop arrests (see Fig. 3.4(a)),

which is in contradiction with the mechanism by [17]. Furthermore, when the criterion by [17] is modified to account for the finite impact velocity of the drop it strongly underestimates the maximum spreading diameter measured.

In fact, the arrest diameter predicted by the kinetic undercooling scenario is of the order of the defect distance D_d shown in Fig. 3.3 (see App. 3.B). We therefore hypothesize that the *first* contact line arrest indeed occurs through the kinetic undercooling mechanism described in [17]. However, as long as the bulk liquid in the drop has enough kinetic energy available, new liquid can flow over this solidification front and touchdown at the substrate again at a larger distance [40]. This process continues until the majority of the bulk liquid is solidified and the entire drop comes to halt. During these repeated contact-line motions air is entrapped, and ridge patterns as shown in Fig.3.3 are formed. A more systematic study of the location of the defect diameter as a function of substrate temperature and impact velocity is required to further validate this hypothesis.

During the impact corrugations grow at the contact line from which ligaments may be formed. We have shown that solidification strongly reduces the number of ligaments that form, in agreement with the results reported by [21]. However, our bottom-view images provided a unique additional insight: We observed the ligaments on the solidifying drops form from a stripe pattern that is already present during the very early stages just after impact. This observation led us to propose a model where on cold substrates the early-stage ejecta sheet solidifies and thereby forms a solidified pattern over which the remaining liquid flows. Thereby, corrugations of the frozen ejecta sheet interfere with the late-time instabilities developing at the rim and strongly influence the observed wavelength.

The solidified ejecta is also a potential cause of the freezing-induced splashing we observed. The solidified pattern increases the surface roughness and can thereby trigger instabilities in the spreading drop. As a result, splashing is observed at Weber numbers below the isothermal splashing threshold. By contrast, solidification also shifts the last deposition event to higher Weber numbers, thereby increasing the width of the transition zone where both splashing and deposition occur. To further quantify this shift, an experimental setup that can achieve higher Weber numbers is required, possibly with another drop generation method. On the theoretical side, a future challenge is to adapt existing splashing models such as the one by [29] to account for the solidifying ejecta sheet.

3.A 1D model for the solidified layer

The thickness of the solidified layer in Eq. (3.4) is determined from a one-dimensional heat transfer model [42, p. 185-188], which we briefly discuss here. This model assumes a quasi-static situation with a solid in contact with a liquid at different

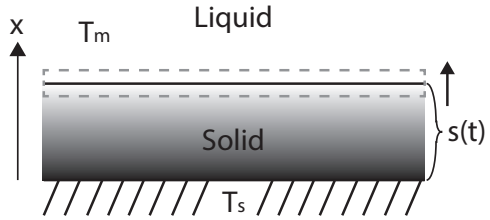

Figure 3.9: Schematic view of the solidification process. A solidified layer of thickness s grows on top of a substrate that is kept at T_s. The liquid above s is assumed to be isothermal and at T_m, while temperature gradients exist in the solidified layer. The gray dashed rectangle indicates the control volume which moves along with the solidification front.

temperature. Thereby we neglect the 3D nature of the problem as well as the transient effects that occur as the drop spreads in time.

Figure 3.9 shows a sketch of the model: An isothermal liquid slab at the solidification temperature T_m is in contact with a solid substrate kept at $T_s < T_m$. From the substrate the liquid starts to solidify forming a layer $s(t)$. The motion of $s(t)$ is governed by energy conservation in a control volume enclosing the front

$$\rho \frac{\partial s}{\partial t} AL = -kA \left(\frac{\partial T}{\partial x} \right)_{x=s}, \tag{3.18}$$

with ρ the density of the liquid, A the area of the solidification front, and L the latent heat for solidification. The left-hand side describes the energy that has to be extracted from the control volume to solidify the liquid. On the right-hand side the heat transfer from the solidification front to the solid is denoted. Both terms of Eq. (3.18) depend on the exact location of the solidification front, which changes over time.

For a thin solidified layer (Ste < 1) the quasi-static temperature distribution in the solid is approximately linear

$$\frac{T_m - T(x,t)}{T_s - T_m} \sim 1 - \frac{x}{s(t)}. \tag{3.19}$$

Combining Eqs. (3.18) and (3.19) we find

$$s \sim \sqrt{\frac{c_p(T_m - T_s)}{L} \frac{k}{\rho c_p} t}, \tag{3.20}$$

with $k/\rho c_p = \kappa$. In dimensionless form we obtain

$$s^* = \frac{s}{D} \sim \sqrt{t^* \frac{\mathrm{Ste}}{\mathrm{Pe}}}. \tag{3.21}$$

3.B Contact line arrest criterion for impacting drops

Here, we derive the arrest criterion for impacting drops based on kinetic undercooling [17]. In this criterion the drop stops spreading when contact line reaches a critical temperature: A non-equilibrium solidification temperature that is lower than the bulk solidification temperature. In [17] this effect is studied in detail for drops after deposition (no impact velocity).

We now modify this criterion to account for the contact line velocity U_{CL} of an impacting drop. From our measurements (see Fig. 3.3) we observe that the point of first arrest D_d is relatively small, which means it is determined at early times after impact.

In this early time regime ($t^* < 0.1$) drop spreading follows [7]

$$\xi = \frac{D_s}{D} = b \cdot (t^*)^{1/2}, \tag{3.22}$$

where $b = 2.9$ from [7]. The contact line velocity is the given by

$$U_{CL} = \frac{dD_s}{dt} = bU\,(t^*)^{-1/2} = b^2 \xi^{-1} U, \tag{3.23}$$

where we used Eq. (3.22) to express t^* in terms of ξ.

For small kinetic undercooling the velocity of the solidification front U_{front} at arrest is given by [46–48]

$$T_m - T_{front} = U_{front}/\kappa, \tag{3.24}$$

with T_{front} the temperature of the solidification front and κ is the kinetic undercooling coefficient, which is a liquid property that has to be determined from experiments. In line with [17] we assume that the contact line arrests once the velocity of the solidification front equals the contact line velocity $U_{front} = U_{CL}$. In that case, the temperature of the contact line has to be equal to the temperature of the solidification front, i.e. $T_{CL} = T_{front}$. For small contact angles the height of the drop close to the contact line is also small and temperature gradients inside the drop are negligible [17], such that $T_{CL} = T_s$. The arrest criterion of Eq. (3.24) then becomes

$$U_{CL} = (T_m - T_s)\kappa. \tag{3.25}$$

Combining Eqs. (3.23) and (3.25) we find an expression for the defect distance

$$\xi_d = \frac{D_d}{D} = d^2 \frac{U}{(T_m - T_s)\kappa}. \tag{3.26}$$

For the experiment shown in Fig. 3.3(a) we find $\xi_d \approx 0.7$ (as determined from high-resolution images) which gives $\kappa = 0.16$ m/(sK), which is of the right order of magnitude for metals [49–52].

References

[1] C. W. Visser, P. E. Frommhold, S. Wildeman, R. Mettin, D. Lohse, and C. Sun, "Dynamics of high-speed micro-drop impact: numerical simulations and experiments at frame-to-frame times below 100 ns", Soft Matter **11**, 1708–1722 (2015).

[2] M. Vaezi, H. Seitz, and S. Yang, "A review on 3d micro-additive manufacturing technologies", Int. J. Adv. Manuf. Tech. **67**, 17211754 (2013).

[3] P. Fauchais, A. Vardelle, M. Vardelle, and M. Fukumoto, "Knowledge concerning splat formation: An invited review", J. Therm. Spray Techn. **13**, 337360 (2004).

[4] M. J. Kreder, J. Alvarenga, P. Kim, and J. Aizenberg, "Design of anti-icing surfaces: smooth, textured or slippery?", Nat. Rev. Mats. **1** (2016).

[5] P. Tourkine, M. Le Merrer, and D. Qur, "Delayed freezing on water repellent materials", Langmuir **25**, 7214–7216 (2009).

[6] L. Mishchenko, B. Hatton, V. Bahadur, J. A. Taylor, T. Krupenkin, and J. Aizenberg, "Design of ice-free nanostructured surfaces based on repulsion of impacting water droplets", ACS Nano **4**, 7699–7707 (2010).

[7] R. Rioboo, M. Marengo, and C. Tropea, "Time evolution of liquid drop impact onto solid, dry surfaces", Exp. Fluids **33**, 112–124 (2002).

[8] J. Eggers, M. A. Fontelos, C. Josserand, and S. Zaleski, "Drop dynamics after impact on a solid wall: Theory and simulations", Phys. Fluids **22** (2010).

[9] M. Pasandideh-Fard, R. Bhola, S. Chandra, and J. Mostaghimi, "Deposition of tin droplets on a steel plate: simulations and experiments", Int. J. Heat Mass Tran. **41**, 2929 – 2945 (1998).

[10] R. Dhiman and S. Chandra, "Freezing-induced splashing during impact of molten metal droplets with high weber numbers", Int. J. Heat Mass Tran. **48**, 5625 – 5638 (2005).

[11] R. Dhiman, A. G. McDonald, and S. Chandra, "Predicting splat morphology in a thermal spray process", Surf. Coat. Tech. **201**, 7789 – 7801 (2007).

[12] S. Chandra and P. Fauchais, "Formation of solid splats during thermal spray deposition", J. Therm. Spray Techn. **18**, 148–180 (2009).

[13] M. Schremb, S. Borchert, E. Berberovic, S. Jakirlic, I. V. Roisman, and C. Tropea, "Computational modelling of flow and conjugate heat transfer of a drop impacting onto a cold wall", Int. J. Heat Mass Tran. **109**, 971 – 980 (2017).

[14] M. Schremb, I. V. Roisman, and C. Tropea, "Normal impact of supercooled water drops onto a smooth ice surface: experiments and modelling", J. Fluid Mech. **835**, 10871107 (2018).

[15] C. Clanet, C. Béguin, D. Richard, and D. Quéré, "Maximal deformation of an impacting drop", J. Fluid Mech. **517**, 199208 (2004).

[16] N. Laan, K. G. de Bruin, D. Bartolo, C. Josserand, and D. Bonn, "Maximum diameter of impacting liquid droplets", Phys. Rev. Appl. **2**, 044018 (2014).

[17] R. de Ruiter, P. Colinet, P. Brunet, J. H. Snoeijer, and H. Gelderblom, "Contact line arrest in solidifying spreading drops", Phys. Rev. Fluids **2**, 043602 (2017).

[18] S. Schiaffino and A. A. Sonin, "Motion and arrest of a molten contact line on a cold surface: An experimental study", Phys. Fluids **9**, 2217 (1997).

[19] S. Schiaffino and A. A. Sonin, "On the theory for the arrest of an advancing molten contact line on a cold solid of the same material", Phys. Fluids **9**, 2227 (1997).

[20] F. Tavakoli, S. H. Davis, and H. P. Kavehpour, "Spreading and arrest of a molten liquid on cold substrates", Langmuir **30**, 10151–10155 (2014).

[21] S. D. Aziz and S. Chandra, "Impact, recoil and splashing of molten metal droplets", Int. J. Heat Mass Tran. **43**, 2841 – 2857 (2000).

[22] R. Bhola and S. Chandra, "Parameters controlling solidification of molten wax droplets falling on a solid surface", J. Mater. Sci. **34**, 4883–4894 (1999).

[23] C. Mundo, M. Sommerfeld, and C. Tropea, "Droplet-wall collisions: Experimental studies of the deformation and breakup process", Int. J. Multiphas. Flow **21**, 151 – 173 (1995).

[24] A. L. Yarin and D. A. Weiss, "Impact of drops on solid surfaces: self-similar capillary waves, and splashing as a new type of kinematic discontinuity", J. Fluid Mech. **283**, 141–173 (1995).

[25] I. V. Roisman and C. Tropea, "Impact of a drop onto a wetted wall: description of crown formation and propagation", J. Fluid Mech. **472**, 373–397 (2002).

[26] C. Josserand and S. Zaleski, "Droplet splashing on a thin liquid film", Phys. Fluids **15**, 1650–1657 (2003).

[27] L. Xu, W. W. Zhang, and S. R. Nagel, "Drop splashing on a dry smooth surface", Phys. Rev. Lett. **94**, 184505 (2005).

[28] A. Latka, A. Strandburg-Peshkin, M. M. Driscoll, C. S. Stevens, and S. R. Nagel, "Creation of prompt and thin-sheet splashing by varying surface roughness or increasing air pressure", Phys. Rev. Lett. **109**, 054501 (2012).

[29] G. Riboux and J. M. Gordillo, "Experiments of drops impacting a smooth solid surface: A model of the critical impact speed for drop splashing", Phys. Rev. Lett. **113**, 024507 (2014).

[30] L. Xu, "Liquid drop splashing on smooth, rough, and textured surfaces", Phys. Rev. E. **75**, 056316 (2007).

[31] P. Tsai, R. C. A. van der Veen, M. van de Raa, and D. Lohse, "How micropatterns and air pressure affect splashing on surfaces", Langmuir **26**, 16090–16095 (2010), pMID: 20860398.

[32] I. V. Roisman, A. Lembach, and C. Tropea, "Drop splashing induced by target roughness and porosity: The size plays no role", Adv. Colloid Interfac. **222**, 615 – 621 (2015), reinhard Miller, Honorary Issue.

[33] C. J. Howland, A. Antkowiak, J. R. Castrejón-Pita, S. D. Howison, J. M. Oliver, R. W. Style, and A. A. Castrejón-Pita, "It's harder to splash on soft solids", Phys. Rev. Lett. **117**, 184502 (2016).

[34] R. E. Pepper, L. Courbin, and H. A. Stone, "Splashing on elastic membranes: The importance of early-time dynamics", Phys. Fluids **20**, 082103 (2008).

[35] M. V. Gielen, R. de Ruiter, J. H. Snoeijer, and H. Gelderblom, "Suppressed splashing on elastic membranes", arXiv, 1711.05634.

[36] M. Pasandideh-Fard, V. Pershin, S. Chandra, and J. Mostaghimi, "Splat shapes in a thermal spray coating process: Simulations and experiments", J. Therm. Spray Techn. **11**, 206–217 (2002).

[37] S. X. Cheng, T. Li, and S. Chandra, "Producing molten metal droplets with a pneumatic droplet-on-demand generator", J. Mater. Process. Tech. **159**, 295 – 302 (2005).

[38] S.-Y. Zhong, L.-H. Qi, J. Luo, H.-S. Zuo, X.-H. Hou, and H.-J. Li, "Effect of process parameters on copper droplet ejecting by pneumatic drop-on-demand technology", J. Mater. Process. Tech. **214**, 3089 – 3097 (2014).

[39] W. Bouwhuis, R. C. A. van der Veen, T. Tran, D. L. Keij, K. G. Winkels, I. R. Peters, D. van der Meer, C. Sun, J. H. Snoeijer, and D. Lohse, "Maximal air bubble entrainment at liquid-drop impact", Phys. Rev. Lett. **109**, 264501 (2012).

[40] J. de Ruiter, D. Soto, and K. K. Varanasi, "Self-peeling of impacting droplets", Nat. Phys. (2017).

[41] E. Villermaux and B. Bossa, "Single-drop fragmentation determines size distribution of raindrops", Nat. Phys. **5** (2009).

[42] A. Bejan, *Heat Transfer* (John Wiley & Sons, Inc., Hoboken, New Jersey) (1993).

[43] E. Villermaux and B. Bossa, "Drop fragmentation on impact", J. Fluid Mech. **668**, 412–435 (2011).

[44] M. Pasandideh-Fard, Y. M. Qiao, S. Chandra, and J. Mostaghimi, "Capillary effects during droplet impact on a solid surface", Phys. Fluids **8** (1996).

[45] S. Wildeman, C. W. Visser, C. Sun, and D. Lohse, "On the spreading of impacting drops", J. Fluid Mech. **805**, 636655 (2016).

[46] M. Amini and B. B. Laird, "Kinetic coefficient for hard-sphere crystal growth from the melt", Phys. Rev. Lett. **97**, 216102 (2006).

[47] A. Fedorchenko and A.-B. Wang, "Non-equilibrium solidification of the molten metal droplets impacting on a solid surface", Int. J. Heat Mass Transfer **50**, 2463 – 2468 (2007).

[48] D. M. Herlach, "Dendrite growth kinetics in undercooled melts of intermetallic compounds", Crystals **5**, 355–375 (2015).

[49] G. Rodway and J. Hunt, "Thermoelectric investigation of solidification of lead I. pure lead", J. of Cryst. Growth **112**, 554 – 562 (1991).

[50] F. Celestini and J.-M. Debierre, "Measuring kinetic coefficients by molecular dynamics simulation of zone melting", Phys. Rev. E **65**, 041605 (2002).

[51] D. Buta and M. Asta, "Kinetic coefficient of steps at the Si(111) crystal-melt interface from molecular dynamics simulations", J. of Chem. Phys. **127**, 074703 (2007).

[52] J. Monk, Y. Yang, M. I. Mendelev, M. Asta, J. J. Hoyt, and D. Y. Sun, "Determination of the crystal-melt interface kinetic coefficient from molecular dynamics simulations", Model. Simul. Mater. Sci. Eng. **18**, 015004 (2010).

4

Suppressed splashing on elastic membranes *

The dynamics of drop impact on solid surfaces can be changed significantly by tuning the elasticity of the solid. Most prominently, the substrate deformation causes an increase in the splashing threshold as compared to impact onto perfectly rigid surfaces, and can thus lead to splash suppression. Here, we experimentally determine the splashing threshold for impact on thin membranes as a function of the tension in the membrane and its elastic properties. The drop dynamics is correlated to the membrane deformation, which is simultaneously measured using a laser profilometry technique. The experimental results enable us to adapt current models for splashing, showing quantitatively how substrate deformation alters the splashing threshold.

4.1 Introduction

Drop splashing onto an elastic membrane is a widely observed phenomenon. For example, it is encountered when rain drops impact onto leaves, where the impact can lead to damage [1], or the splashing drop can play a role in the outbreak of foliar diseases [2]. In industry, drop splashing onto an elastic substrate is encountered in e.g. pesticide delivery [3], (biological) inkjet printing [4, 5], and (cold) spray coating [6, 7]. In these applications, splashing decreases the deposition efficiency and may lead to widespread contamination, and is therefore an unwanted side effect.

Splashing of drops during impact is widely studied, as a function of the drop

*Under review in Physical Review Fluids as: "Suppressed splashing on elastic membranes", M.V. Gielen, R. de Ruiter, J.H. Snoeijer and H. Gelderblom

properties [8–10], the properties of the surroundings [11, 12], and the substrate properties [9, 12–15]. The impact velocity [8] or viscosity [9] of the drop are examples of drop properties that can be changed to control splashing. The surrounding air influences drop splashing by its pressure [11, 12]. The substrate at which the drop impacts also influences drop splashing, for example by its structure [9, 12, 13].

To quantify the splashing threshold of a drop with diameter D, velocity U, density ρ, surface tension γ, and kinematic viscosity ν, Mundo, Sommerfeld and Tropea [8] derived the well-known criterion: $\mathrm{We}^{1/2}\mathrm{Re}^{1/4} > K$, where $\mathrm{We} = \frac{\rho D U^2}{\gamma}$ is the Weber number, $\mathrm{Re} = \frac{DU}{\nu}$ is the Reynolds number, and K is the critical number to obtain splashing depending on for example substrate properties. This splashing criterion can be related to the argument that the velocity at which the ejecta sheet moves away from the impact location has to be larger than the Taylor-Culick velocity to obtain splashing [16]. For different kinds of substrates, typical values for K are found: $K \approx 54$ for a rigid surface [17], $K \approx 160$ for a thin liquid film [18] and $K \approx 90$ for a deep liquid pool [19]. For oblique drop impact on a liquid pool, this splashing criterion is modified to account for the parallel impact velocity [20]. However, this splashing criterion by Mundo, Sommerfeld and Tropea does not account for the role of the surrounding atmosphere [11, 12].

Recently, Riboux and Gordillo [21] derived a new splash criterion that includes the effect of the surrounding gas and showed good agreement with the experimental results of Ref. [11]. In this argument the liquid not only has to dewet the solid, but the upward velocity of the ejecta also has to be large enough to prevent touchdown of the growing rim, which leads to an adapted splashing threshold:

$$(\mu_g U/\gamma)\tilde{t}_e^{-1/2} > C, \tag{4.1}$$

where C is the critical number to obtain splashing based on e.g. surface properties, μ_g is the dynamic viscosity of the surrounding gas and $\tilde{t}_e = t_e U/D$ is the dimensionless time for sheet ejection.

On elastic or soft substrates, the splashing threshold is found to increase with decreasing substrate (visco)elasticity [14, 15]. On a viscoelastic substrate [15] a drop needs up to 70 % more kinetic energy to splash compared to a rigid surface, which is attributed to the substrate deformation during the early stages of impact. A similar result is found on elastic membranes [14]. However quantitative data of the substrate deformation and supporting modeling are lacking. Moreover, the role of substrate elasticity has not been evaluated in light of the recent advances on the splashing threshold by Ref. [21].

Here, we experimentally study the splashing threshold on an elastic membrane. Details of the experimental setup for analyzing the drop impact and the membrane deformation are provided in Sec. 4.2 and a typical impact experiment is discussed in Sec. 4.3.1. The splashing threshold is measured for different membrane elasticities

in Sec. 4.3.2. Systematic measurements of the membrane deformation are presented in Sec. 4.3.3. In Sec. 4.4 we interpret our observations and modify the splashing threshold model by Ref. [21], taking the elastic properties of the membrane into account. The chapter closes with a discussion in Sec. 4.5.

4.2 Experimental methods

To study the influence of membrane elasticity on drop splashing during impact, we place an elastic membrane (plastic wrap, WRAPPITT) over a circular Teflon frame with diameter 10 cm, as shown in Fig. 4.1(a). The setup is similar to the one described in Ref. [14], but with choice of different materials for frame and membrane. The thickness of the membrane $h = 13 \pm 0.5$ μm, the density $\rho_f = 1.7{\cdot}10^3$ kg/m^3, the Young's Modulus $E = 180 \pm 37$ MPa (calculated from measurements of the extension of the plastic wrap under the influence of added mass) and the roughness $R_a \leq 50$ nm (as measured with SensoSCAN, Sensofar metrology). The frame is wetted to allow the membrane to slide over the frame during the experiments.

The membrane is placed under tension by attaching it to a mass (Fig. 4.1(a)). The mass is added to the membrane carefully, where care is taken to apply no additional tension. To vary the tension in the membrane the mass M attached to it is varied between 292 and 1460 g. The tension is then given by $T = Mg/2\pi R_f$, with g the gravitational constant and R_f the radius of the frame and ranges from $9 \pm 0.2 \leq T \leq 46 \pm 0.7$ N/m. To obtain a measure for the error in the applied additional tension, we use multiple membranes for the experiments at some tensions ($T \approx 9$, 27 and 46 N/m). We notice that when putting the membrane under tension it shows a considerable amount of creep, which affects the reproducibility of our experiments. Therefore, we wait at least two hours after we place the membrane over the frame before performing the experiment.

An ethanol drop with a diameter of $D = 2.3 \pm 0.4$ mm is created by pumping ethanol at low flow rate through a capillary. Experiments take place under ambient conditions, such that the ethanol density $\rho = 789$ kg/m^3 and the surface tension $\gamma =$ 0.02 N/m. By varying the release height of the drop, the impact velocity is controlled between $0.7 \leq U \leq 5.1$ m/s. The outcome of the impact is recorded by side-view shadowgraphy imaging. The drop is illuminated (Sumita LS-M352A) and recordings are taken at 8,000 fps (Photron SA-X2) at a resolution of 23 μm per pixel.

To relate the drop dynamics to the membrane deformation, we simultaneously perform shadowgraphy and membrane deformation measurements. The deformation is measured by laser profilometry, as decribed by Refs. [14] and [22]. The setup for the profilometry measurements is shown schematically in Fig. 4.1(b). We focus two laser sheets (Laser Macro Line Generator, Schäfter+Kirchhoff, $\lambda = 660 \pm 5$ nm, sheet width ~ 300 μm) from below at the bottom of the membrane such that the impacting

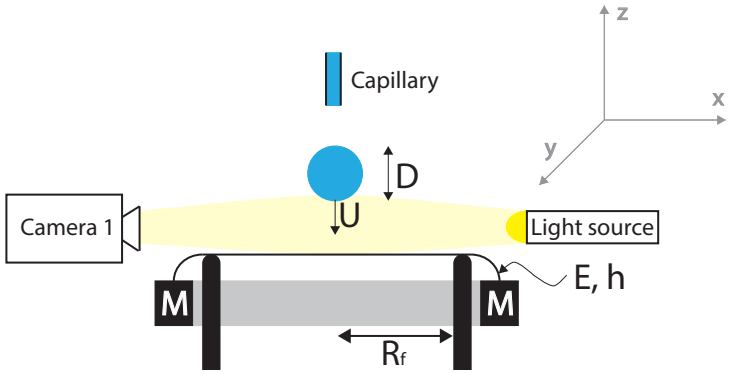

(a)

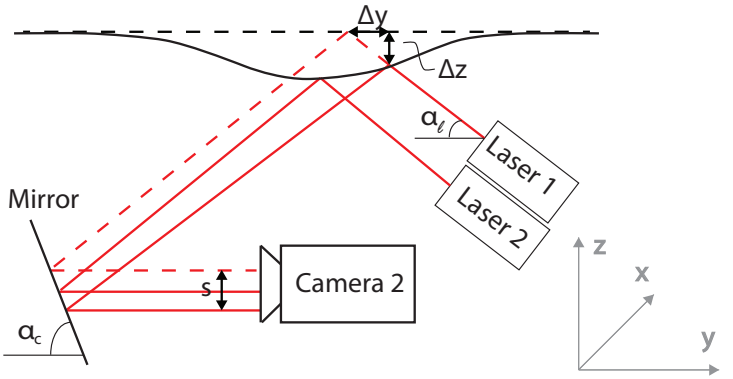

(b)

Figure 4.1: (a) Sketch of the drop impact setup. At the end of the capillary an ethanol drop with diameter D is created. The drop falls down under influence of gravity, such that by changing the release height of the drop the impact velocity U is controlled. The drop impacts onto an elastic membrane, where the added mass M determines the variable tension ($9 \leq T \leq 46$ N/m). The membrane has thickness $h = 13$ μm and Young's Modulus $E = 180$ MPa. A side-view recording of the impact event is made using high speed shadowgraphy imaging. (b) To measure the membrane deformation two laser sheets are focused at the bottom of the membrane within a drop radius apart from each other. A second high speed camera focuses onto the membrane, via a mirror. When a drop impacts the membrane deforms and the recorded position of the laser sheets changes. The displacement s of the laser sheets on the camera is related to the actual membrane deformation Δy and Δz through geometrical relations, using laser angle α_ℓ and camera angle α_c (Eq. (4.2)).

drop is not blocking the view. The use of two laser sheets makes the measurement less sensitive to small variations in the exact impact locations, and provides an additional measurement. A second camera (Photron SA1.1) is focused via a mirror onto the bottom of the membrane recording the location of the laser sheets. In order to increase the reflection of the membrane, the bottom of the membrane is coated with a white powder. Because of this coating, the intensity of the reflections of the laser sheets increases and the quality of the recording improves, obtaining a resolution of 21 μm per pixel at a frame rate of 8,000 fps.

During drop impact the membrane will move down, resulting in a displacement of the laser sheets on the camera. This displacement is related to the actual membrane deformations Δy and Δz via geometrical relations (Fig. 4.1(b)). For small deformations, the deformation is linearly related to the displacement of the laser sheet s [22],

$$\Delta z = \frac{s}{2}\frac{\sin(\alpha_c + \alpha_\ell)}{\cos(\alpha_\ell)} \tag{4.2a}$$

$$\Delta y = \frac{s}{2}\frac{\sin(\alpha_c + \alpha_\ell)}{\sin(\alpha_\ell)}, \tag{4.2b}$$

where α_ℓ is the angle of the laser and α_c is the angle of the camera, corresponding to the angle of the mirror.

To calculate Δy and Δz correctly, α_ℓ and α_c are determined from separate calibration measurements. For α_ℓ, we track the direction of the laser sheets using our drop impact shadowgraphy setup as the light passes through the membrane. For α_c we remove the membrane from our frame and use a flat target for calibration. For various target heights, we know Δz from our shadowgraphy measurement and from our profilometry setup we know α_ℓ and measure s, which allows us to calculate α_c from these combined experiments.

For every impacting drop we detect the profile of the laser sheets. The maximum deformation along the laser sheet gives the impact center of the drop in x-direction (see Fig. 4.2(a)), while the impact center of the drop in y-direction is extracted from the shadowgraphy measurements. Once we know the exact impact position of the drop, we relate every detected point of the laser sheet to a radial distance from the impact center, as shown in Fig. 4.2(a). Combining this radial distance and the measured deformation, we construct the entire profile of the deformed membrane. An example is shown in Fig. 4.2(b). The maximum deformation is not captured by the laser sheets, therefore a linear fit through the four branches is made to determine the maximum deformation at $r = 0$. For each frame, the average value at $r = 0$ of those fits gives an estimate of the central deformation $\delta(t)$ of a single experiment. We compared different fitting functions, and found the linear fit the most appropriate and robust, even though it lacks the condition of vanishing slope at $r = 0$ and therefore slightly overestimates δ.

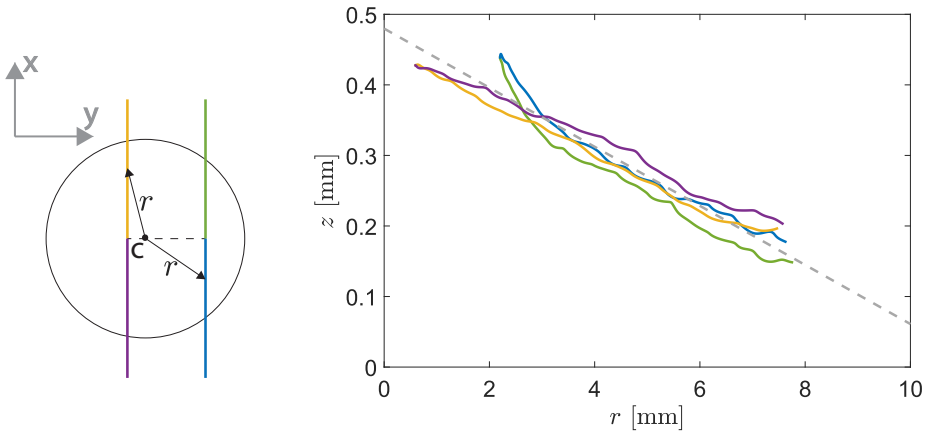

(a) (b)

Figure 4.2: (a) Schematic representation of the drop impact center c with respect to the location of both laser sheets. By combining the shadowgraphy and profilometry recordings, the location of the impact center c is determined. From here the radial distance to both laser sheets is calculated. Each laser sheet therefore consists of two branches starting at the same radial position. (b) Plot showing the membrane profile at maximum deformation for We = 1123 and $T/Eh = 0.012$ (see Fig. 4.3). The colors match the branches from Fig. 4.2(a). With increasing radius from the impact center the deformation decreases. A linear fit (dashed line) is made to the laser sheets to find the maximum deformation at the center of the impacting drop ($r = 0$).

In the experiments we can vary the drop diameter D, impact velocity U and mass M (resulting in a change in membrane tension T) and measure the outcome of the impact and the deformation of the membrane z simultaneously. In dimensionless form, the control parameters are the Weber number We$= \rho DU^2/\gamma$ and the scaled tension T/Eh. Typically, $T/Eh \ll 1$ in our experiments. Our goal is to identify the critical Weber number for splashing as a function of the dimensionless tension, and to correlate this to the membrane's deformability.

4.3 Results

We first explain the general outcome of a drop impact event, emphasizing the information we get from the simultaneous shadowgraphy and profilometry measurements in Sec. 4.3.1. In Sec. 4.3.2 the splashing threshold obtained from shadowgraphy measurements and its dependence on impact velocity and membrane tension are presented. Finally, in Sec. 4.3.3 we show how the membrane deformation varies with impact velocity and membrane tension.

4.3.1 A typical drop impact experiment

Figure 4.3 shows the time series of a typical experiment with We = 1123 and dimensionless tension $T/Eh = 0.012$. The top row images show the drop during impact while the bottom row images show the measured deflection of the laser sheets at the same time. Before impact (Fig. 4.3(a)) the membrane is undeformed, while in Fig. 4.3(b) the impact has started and both drop and membrane are deforming. At $t = t_{max} = 0.63$ ms (Fig. 4.3(c)), the maximum deformation of the membrane is reached, while the drop is still spreading. Shortly after the moment of maximum deformation, secondary droplets break off from the initial drop and a splash is visible (Fig. 4.3(d)). After t = 2.50 ms (Fig. 4.3(e)), the membrane has released all of its stored energy and has returned to its original position. The drop, however, is still spreading further over the membrane until it reaches its maximum spreading diameter at t = 4.30 ms (Fig. 4.3(f)). During this spreading, the membrane oscillates around its equilibrium position until these oscillations are damped out (images not shown here). An important observation, which applies to all splashing events studied, is that the splash occurs after the membrane has reached its maximum deformation. This observation is consistent with the result of Ref. [14].

4.3.2 Splashing threshold

We now study the impact of a drop onto an elastic membrane by systematically varying the impact velocity and the membrane tension. Two different outcomes of an impact event are observed: (i) Deposition: After impact the drop remains intact on

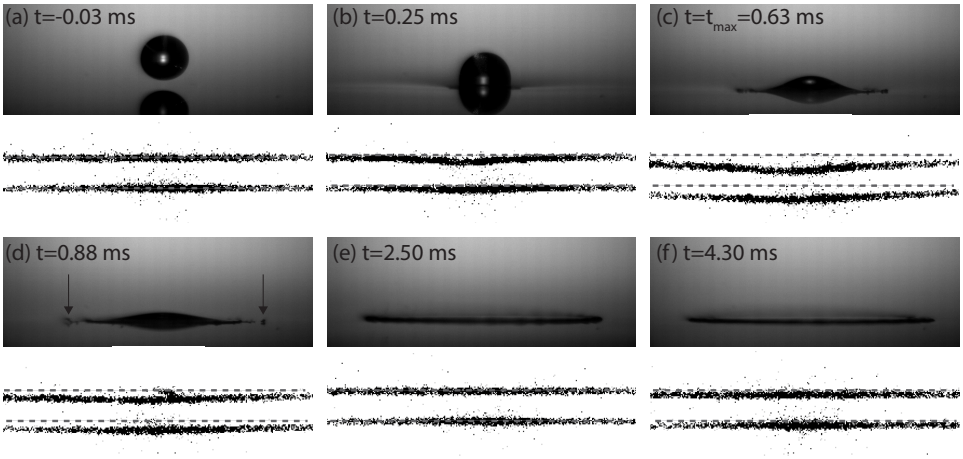

Figure 4.3: Time series of a drop impacting onto the membrane. The dimensionless tension in the membrane is $T/Eh = 0.012$ and the impact Weber number We = 1123. Time t=0 marks the moment the drop makes first contact with the membrane. Each snapshot consists of two images: a side-view image where the drop is visible and an image of the laser sheet reflection on the membrane to show the deformation of the membrane. For clarity, the dashed lines indicate the original position of the laser sheet. (a) t = -0.03 ms: Just before impact, when the membrane is undeformed. (b) t = 0.25 ms: Right after the impact both the drop and the membrane start to deform. (c) t = 0.63 ms: The drop spreads over the membrane, while the membrane reaches its maximum deformation. The corresponding membrane deformation is shown in Fig. 4.2(b). (d) t = 0.88 ms: Drop splashing; the formation of secondary droplets is observed, indicated by the arrows. (e) t = 2.50 ms: The membrane has returned to its original position, while the drop is still spreading over the membrane. (f) t = 4.30 ms: The drop reaches its maximum spreading, while the membrane oscillates around its equilibrium position.

the membrane. (ii) Splashing: After impact small secondary droplets break off from the rim of the original drop. In case only one or two droplets are ejected on the same side, this is still referred to as deposition. Figure 4.4(a) shows all experimental data for different impact velocities and tensions. For low impact velocities, the impacting drop deposits onto the membrane, while for higher impact velocities the drop splashes during impact. With decreasing tension the impact velocity at which splashing is first observed increases. For each tension there is a small region where both deposition and splashing are observed, which is called the transition region. From this transition region the splashing threshold and its standard deviation are derived, which will be used as an error bar for the determination of the splashing threshold. To this end, the impact velocities are grouped in bins with a range of 0.25 m/s and the percentage of drops that splashes during impact is determined. A cumulative distribution function fit is made through all these data points to find the expected threshold value and its standard deviation. To test the reproducibility of our results, we repeated the same experiments with a new membrane for $T/Eh = 0.0039$, 0.012, and 0.020. The increase in standard deviation of the splashing threshold for these experiments shows the sensitivity of the experiments to the manual fixation of the mass to the membrane.

The threshold for splashing is presented in non-dimensional form in Fig. 4.4(b), where we show the critical Weber number $\mathrm{We}_c = \rho D U_c^2/\gamma$ as function of the dimensionless tension T/Eh (black circles). As a reference case, we also performed experiments onto a membrane carefully placed on top of a glass plate, where we avoid air bubble entrainment between the glass plate and the membrane, finding a splashing threshold of We = 255 (solid line). While We_c for splashing decreases with increasing dimensionless tension, the rigid threshold is never reached, which shows that even at the highest tension impact energy is used to deform the membrane. In Ref. [14] a similar range of tensions was studied and the results are reproduced here for comparison (black squares). The authors also found a decrease in splashing threshold, however, in contrast to our results, there the rigid limit (We = 382) was reached already for the highest tensions. Despite the higher rigid splashing threshold, the typical values reported for We_c on the membrane are lower compared to our observations.

4.3.3 Membrane deformation

To explain the splash suppression mechanism, we now turn to the membrane deformation. From a simultaneous measurement of the impact event and membrane deformation, we can relate the deformation dynamics to the impact velocity of the drop. In Fig. 4.5(a) we plot the central deformation (at $r = 0$) as function of time. At $t = t_{max}$ the maximum deformation δ_{max} is reached. Before $t = t_{max}$, the membrane deforms and stores part of the kinetic energy of the impacting drop as elastic energy. For $t > t_{max}$, the membrane returns to its original position and (part of) the stored elastic energy is released. At later times, the membrane oscillates and subsequently

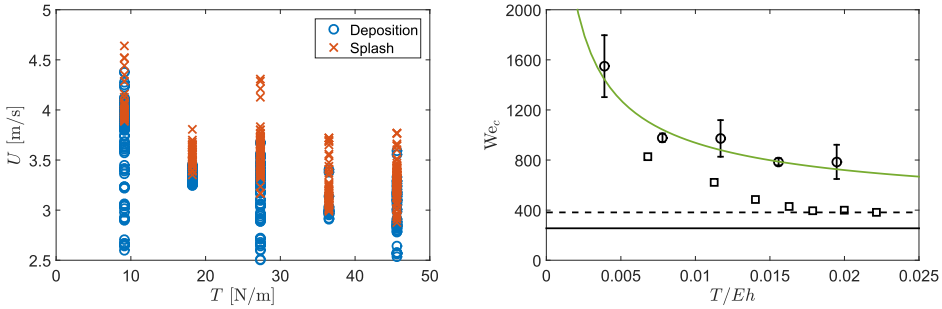

(a) (b)

Figure 4.4: (a) Plot of all individual measurements done for different tensions in the membrane T and varying impact velocity U. The blue circles indicate deposition experiments, while the red crosses indicate splashing experiments. For each tension we find a zone where deposition and splashing events overlap, from which we determine the splash threshold velocity U_c. (b) Non-dimensional plot of the critical Weber number $\mathrm{We}_c = \rho D U_c^2/\gamma$ for splashing as function of the non-dimensional tension in the membrane T/Eh. Circles represent measurements of this study, while squares represent measurements by Ref. [14]. The error bars indicate one standard deviation. The solid black line is the splashing threshold on a rigid substrate with the same surface properties (standard deviation negligibly small), the black dashed line indicates the rigid splashing threshold found by Ref. [14]. For decreasing T/Eh, We_c increases. The solid green line shows the splashing threshold according to Eq. (4.9) with $c_t = 0.07$ for our measurements.

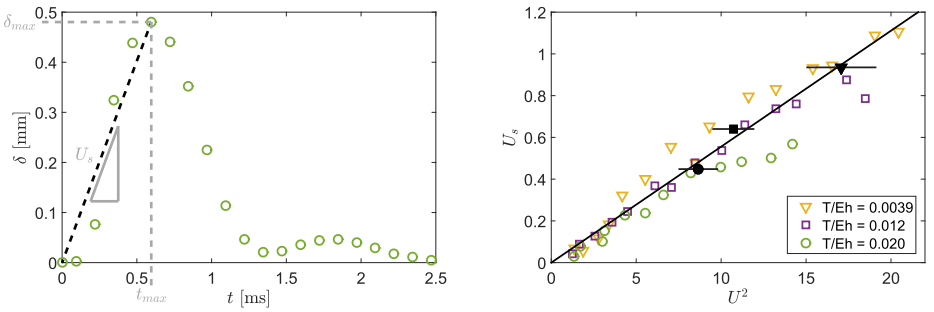

(a) (b)

Figure 4.5: (a) Plot of the central deformation of the membrane δ as function of time t for the same experiment as shown in Fig. 4.3 (We = 1123 and $T/Eh = 0.17$). Time $t = 0$ corresponds to time of impact. A linear fit from zero to maximum deformation δ_{max} gives a measure for the velocity at which the membrane deforms (here $U_s \approx 0.77$ m/s) . Before $t = t_{max} = 0.63$ ms, kinetic energy of the impacting drop is stored as elastic energy in the membrane. For $t > t_{max}$, this elastic energy is released and the membrane returns to its original position while oscillating. (b) Plot of the membrane velocity U_s as a function of U^2 for three different tensions. We have taken bins of $U = 0.25$ m/s to group experiments. U_s is linearly related to U^2 until the splashing threshold is reached. Black symbols indicate the critical velocity for splashing U_c at different tensions with corresponding error bars. The solid line shows the empirical fit given by Eq. (4.3) to the data with $c_U = 18$.

relaxes to its final position.

From Fig. 4.5(a) one can extract the velocity U_s at which the membrane initially deforms from a linear fit. Figure 4.5(b) shows U_s as function of U^2. One observes that the membrane velocity increases linearly with U^2. For larger impact velocities U a deviation from this trend is observed, which starts at lower U for higher tension. The start of this deviation turns out to coincide with the splashing threshold U_c, marked as the black symbols in Fig. 4.5(b). Apparently, from this impact velocity on the membrane can no longer store enough impact energy to prevent the drop from splashing. The lower the tension, the higher U_c, and therefore the higher the membrane velocity where the deviation starts. For $U < U_c$, the membrane velocity collapses onto a single linear curve (black solid line in Fig. 4.5(b)) for all tensions. To describe the data up to the splashing threshold we therefore propose the following empirical law

$$U_s = c_U \frac{U^2}{U^*}, \tag{4.3}$$

where $U^* = \sqrt{E/\rho_f}$ is the characteristic wave velocity of the membrane and $c_U = 18$

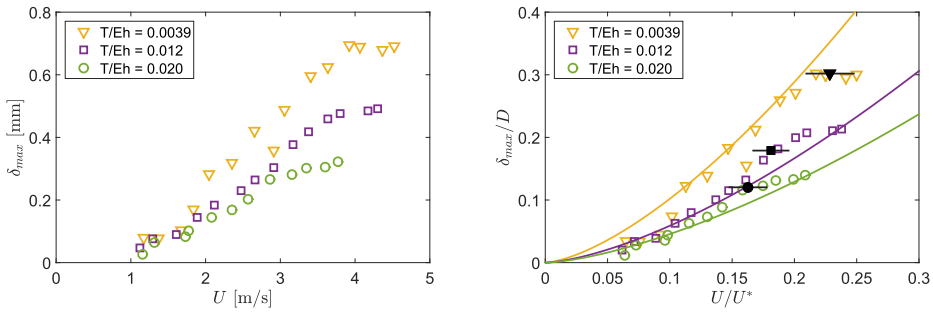

(a) (b)

Figure 4.6: (a) Maximum deformation δ_{max} as function of the impact velocity U. Each open symbol corresponds to a set of experiments averaged over a small range of U (0.25 m/s). For increasing impact velocity the maximum deformation increases. For lower membrane tension the deformation is larger at the same impact velocity. (b) The same data as shown in (a) plotted in dimensionless form. The solid black symbols indicate the maximum deformation measured at the splashing threshold. The increase of deformation with impact velocity is captured by Eq. (4.7) with $c_\delta = 0.4$. After the splashing threshold a deviation is observed between model and experimental data.

gives a fit to our data.

From the membrane deformation measurements as shown in Fig. 4.5(a) one can also extract the maximum deformation of the membrane. In Fig. 4.6(a) we show that the maximum deformation increases with impact velocity, as was to be expected. In addition, the maximum deformation is larger when the tension is smaller.

4.4 Interpretation

We now interpret and quantify the increase in splashing threshold with decreasing tension observed in Fig. 4.4(b). To this end, the model for the splashing threshold on a rigid surface as given by Ref. [21] is modified to account for the membrane elasticity. The modified threshold will turn out to involve both the membrane deformation velocity U_s (Sec. 4.3.3) and the maximum deformation δ_{max}, which is therefore discussed in more detail in Sec. 4.4.1. In Sec. 4.4.2 we then use U_s and δ_{max} to arrive at a splashing criterion for impact on an elastic membrane.

4.4.1 Maximum membrane deformation

In Fig. 4.6(b) we plot the dimensionless maximum deformation δ_{max}/D versus the impact velocity nondimensionalized by the characteristic membrane velocity U/U^*.

To understand the dependence of δ_{max} on U and T, we propose a model for the maximum deformation based on momentum conservation in two consecutive steps: Ⓐ The momentum of the drop before impact is equated to the momentum of the drop and the membrane at the moment of the inelastic collision. Ⓑ Subsequently, at maximum deformation the drop has stopped moving downwards and the membrane has provided an impulse $\sim \sigma h \delta_{max} t_{max}$, with $\sigma = E\varepsilon + T/h$ the total stress in the membrane. In terms of a scaling analysis, the momentum balance then reads

$$\rho D^3 U \overset{Ⓐ}{\sim} (\rho D^3 + \rho_f h \ell^2) U_s \overset{Ⓑ}{\sim} \left(E\varepsilon + \frac{T}{h} \right) h \delta_{max} t_{max}, \tag{4.4}$$

where ℓ is the horizontal length scale over which the membrane is deformed and $\varepsilon \sim (\delta_{max}/\ell)^2$ is the strain in the membrane. From Ⓐ we obtain an expression for ℓ, making use of our experimental observation $U/U_s \gg 1$,

$$\ell^2 \sim \frac{\rho D^3}{\rho_f h} \frac{U}{U_s}. \tag{4.5}$$

For the parameters in our experiments this predicts $\ell \sim 10^{-2}$ m, which is consistent with the experimental observations (Fig. 4.2(b)).

Eliminating ℓ through Eq. (4.5) and using that $t_{max} \sim \delta_{max}/U_s$ in Eq. (4.4)Ⓑ we obtain a quadratic relation for δ_{max}:

$$\left(\frac{\delta_{max}}{D} \right)^2 = \frac{1}{2} c_\delta^2 \frac{\rho D}{\rho_f h} \frac{T}{Eh} \frac{U}{U_s} \left[-1 + \sqrt{1 + 4 \frac{E h^2 \rho_f}{T^2} U_s^2} \right]. \tag{4.6}$$

The use of an equality sign in Eq. (4.6) requires a definition of the proportionality constant c_δ, which will be determined from experiments. Noting that $4\frac{Eh^2\rho_f}{T^2} U_s^2 \ll 1$ allows us to reduce Eq. (4.6) to

$$\left(\frac{\delta_{max}}{D} \right) = c_\delta \left[\frac{\rho D U U_s}{T} \right]^{1/2}, \tag{4.7}$$

where U_s follows from Eq. (4.3). A fit of Eq. (4.7) to the data in Fig. 4.6(b) gives c_δ = 0.4.

Figure 4.6(b) confirms that Eq. (4.7) captures the dependence of δ_{max} on both U and T up to U_c, where the membrane velocity starts to deviate from Eq. (4.3).

4.4.2 Splashing threshold

The next step is to adapt the splashing criterion by Riboux and Gordillo given in Eq. (4.1) to account for the membrane elasticity. To this end, we use the empirical relation of the membrane velocity Eq. (4.3) and the model for the membrane deformation Eq. (4.7).

For completeness, we first briefly recap the model for splashing on a rigid substrate. To obtain splashing, two criteria have to be fulfilled simultaneously [21]: (i) The ejecta sheet has to dewet the solid such that the ejecta sheet moves upwards, and (ii) the vertical velocity at the tip of the ejecta sheet has to be large enough to prevent touchdown of the growing rim on the substrate. Once both conditions are fulfilled, the splashing criterion is given by Eq. (4.1), where the time scale for sheet ejection at the splashing threshold $t_{e,c}$ is found from [21]

$$k_1 \mathrm{Re}_c^{-1} \tilde{t}_{e,c}^{-1/2} + \mathrm{We}_c^{-1} = k^2 \tilde{t}_{e,c}^{3/2}, \tag{4.8}$$

with $\tilde{t}_{e,c} = t_{e,c} U_c / D$ and $k_1 = \sqrt{3}/2$ and $k = 1.1$ taken from Ref. [21]. Our measurements on a rigid substrate coated by the elastic membrane give a critical impact velocity $U_c \approx 1.8$ m/s. Applying the model of Eqs. (4.1) and (4.8) to our measurements of a membrane coated glass slide, we obtain $\tilde{t}_{e,c} \approx 0.027$ ($t_{e,c} \approx 35\ \mu$s), and find for the critical splashing number $C \approx 0.0093$.

On an elastic membrane criteria (i) and (ii) still need to be fulfilled to obtain splashing. However, as the impact energy is firstly absorbed by the membrane and released only at later times $t > t_{max}$, we hypothesize it is now the time scale of the membrane deformation that controls the sheet ejection. We therefore suggest a modified splashing criterion by simply adding t_e and t_m in Eq. (4.1), such that the splash criterion now reads

$$\frac{\mu_g U_c}{\gamma} (\tilde{t}_e + c_t \tilde{t}_{max,c})^{-1/2} = C, \tag{4.9}$$

where c_t is a fitting parameter. The critical dimensionless time of membrane deformation is given by $\tilde{t}_{max,c} = \frac{\delta_{max}}{D} \frac{U_c}{U_s}$, where the membrane velocity is given by Eq. (4.3) and the maximum substrate deformation by Eq. (4.7) with the prefactors as determined from the independent deformation measurements. In the limit where $T \to \infty$ ($\tilde{t}_{max} \to 0$) one recovers the splashing criterion on a rigid substrate (Eq. (4.1)).

In Fig. 4.4(b), Eq. (4.9) is compared to the experimental data, as shown by the solid green line. In Eq. (4.9) $C = 0.0093$ as obtained for a rigid substrate is used, since the only substrate property that is varied in the experiment is the tension. We then solve Eq. (4.9) numerically, using $\mu_g = 1.7 \cdot 10^{-5}$ kg/m·s and find good agreement with the experimentally determined splashing threshold for $c_t = 0.07$.

4.5 Discussion and Conclusion

The splashing threshold for drop impact onto an elastic membrane is determined by the simultaneous measurement of the impact behavior by side-view imaging and the membrane deformation by laser profilometry. The observed increase in splashing

threshold with decreasing tension is interpreted by modifying the splashing criterion by Ref. [21] to account for the membrane deformation.

From the profilometry measurements we extracted two key quantities that determine the splashing threshold: the membrane deformation velocity and the maximum membrane deformation. We observed a quadratic scaling of the membrane velocity with the impact velocity independent of membrane tension, up to the splashing threshold. For larger impact velocities the membrane can no longer deform fast enough and the drop splashes. The maximum membrane deformation could accurately be described by a simple scaling argument based on momentum conservation, again up to the splashing threshold. The increased splashing threshold is then explained by a delayed sheet ejection time caused by the membrane deformation dynamics, and showed good agreement with experimental data. Unfortunately we could not test the splashing criterion against the data by Ref. [14], since the reported measurements do not provide enough data on the membrane deformation.

So far, we validated the modified splashing criterion by measuring the splashing threshold as a function of membrane tension. A more direct validation would require measurements of the sheet ejection time as a function of the membrane tension, which unfortunately was obscured from view by the membrane deformation. On visco-elastic gels similar problems have been reported [15]. A detailed numerical model could be used to overcome these experimental limitations. Moreover, such model could provide a detailed description of the membrane dynamics and explain the observed deviation from the quadratic scaling in the membrane velocity. However, our basic modification of Riboux and Gordillo [21] based on simple scaling arguments is already capable of predicting the observed trends.

References

[1] S. Gart, J. E. Mates, C. M. Megaridis, and S. Jung, "Droplet impacting a cantilever: A leaf-raindrop system", Phys. Rev. Applied **3**, 044019 (2015).

[2] T. Gilet and L. Bourouiba, "Fluid fragmentation shapes rain-induced foliar disease transmission", J. Roy. Soc. Interface **12** (2015).

[3] C. A. E. Peirce, C. Priest, T. M. McBeath, and M. J. McLaughlin, "Uptake of phosphorus from surfactant solutions by wheat leaves: spreading kinetics, wetted area, and drying time", Soft Matter **12**, 209–218 (2016).

[4] A. Tirella, F. Vozzi, C. D. Maria, G. Vozzi, T. Sandri, D. Sassano, L. Cognolato, and A. Ahluwalia, "Substrate stiffness influences high resolution printing of living cells with an ink-jet system", J. Biosci. Bioeng. **112**, 79 – 85 (2011).

[5] D. B. van Dam and C. L. Clerc, "Experimental study of the impact of an ink-jet printed droplet on a solid substrate", Phys. Fluids **16**, 3403 – 3414 (2004).

[6] R. Lupoi and W. O'Neill, "Deposition of metallic coatings on polymer surfaces using cold spray", Surf. Coat. Technol. **205**, 2167 – 2173 (2010).

[7] R. Srikar, T. Gambaryan-Roisman, C. Steffes, P. Stephan, C. Tropea, and A. Yarin, "Nanofiber coating of surfaces for intensification of drop or spray impact cooling", Int. J. Heat Mass Tran. **52**, 5814 – 5826 (2009).

[8] C. Mundo, M. Sommerfeld, and C. Tropea, "Droplet-wall collisions: Experimental studies of the deformation and breakup process", Int. J. Multiphas. Flow **21**, 151 – 173 (1995).

[9] L. Xu, "Liquid drop splashing on smooth, rough, and textured surfaces", Phys. Rev. E. **75**, 056316 (2007).

[10] R. Rioboo, M. Marengo, and C. Tropea, "Time evolution of liquid drop impact onto solid, dry surfaces", Exp. Fluids **33**, 112–124 (2002).

[11] L. Xu, W. W. Zhang, and S. R. Nagel, "Drop splashing on a dry smooth surface", Phys. Rev. Lett. **94**, 184505 (2005).

[12] A. Latka, A. Strandburg-Peshkin, M. M. Driscoll, C. S. Stevens, and S. R. Nagel, "Creation of prompt and thin-sheet splashing by varying surface roughness or increasing air pressure", Phys. Rev. Lett. **109**, 054501 (2012).

[13] P. Tsai, R. C. A. van der Veen, M. van de Raa, and D. Lohse, "How micropatterns and air pressure affect splashing on surfaces", Langmuir **26**, 16090–16095 (2010), pMID: 20860398.

[14] R. E. Pepper, L. Courbin, and H. A. Stone, "Splashing on elastic membranes: The importance of early-time dynamics", Phys. Fluids **20**, 082103 (2008).

[15] C. J. Howland, A. Antkowiak, J. R. Castrejón-Pita, S. D. Howison, J. M. Oliver, R. W. Style, and A. A. Castrejón-Pita, "It's harder to splash on soft solids", Phys. Rev. Lett. **117**, 184502 (2016).

[16] C. Josserand and S. Zaleski, "Droplet splashing on a thin liquid film", Phys. Fluids **15**, 1650–1657 (2003).

[17] C. Josserand and S. Thoroddsen, "Drop impact on a solid surface", Ann. Rev. Fluid Mech. **48**, 365–391 (2016).

[18] R. D. Deegan, P. Brunet, and J. Eggers, "Complexities of splashing", Nonlinearity **21**, C1 (2008).

[19] E. Castillo-Orozco, A. Davanlou, P. K. Choudhury, and R. Kumar, "Droplet impact on deep liquid pools: Rayleigh jet to formation of secondary droplets", Phys. Rev. E 053022 (2015).

[20] M. V. Gielen, P. Sleutel, J. Benschop, M. Riepen, V. Voronina, C. W. Visser, D. Lohse, J. H. Snoeijer, M. Versluis, and H. Gelderblom, "Oblique drop impact onto a deep liquid pool", Phys. Rev. Fluids **2**, 083602 (2017).

[21] G. Riboux and J. M. Gordillo, "Experiments of drops impacting a smooth solid surface: A model of the critical impact speed for drop splashing", Phys. Rev. Lett. **113**, 024507 (2014).

[22] S.-C. Zhao, R. de Jong, and D. van der Meer, "Raindrop impact on sand: a dynamic explanation of crater morphologies", Soft Matter **11**, 6562 – 6568 (2015).

5

Valorization chapter: How to suppress splashing in the EUV source

In this thesis we studied drop impact for different substrate properties and impact conditions. In this chapter we focus on the implications of our results for the impact dynamics in the EUV source. Here we provide guidelines to overcome challenges in the EUV source based on the results obtained in Chap. 2 to 4, and we discuss the missing knowledge to eliminate sources of tin debris. Next to that, we present additional experiments to specifically assess the conditions of practical relevance.

In Sec. 5.2 we show in what direction and with what droplet size and velocity splashed droplets are created after oblique impact onto liquid-coated substrates such as the side walls or the tin catcher. We then discuss how the temperature of substrates in the source can be used to control and prevent splashing of drops after impact in Sec. 5.3. Finally, in Sec. 5.4 we present a method to determine the impact conditions of a drop from the solidified splat. This provides a way to determine the diameter of the impacting drop, the impact angle as well as the impact velocity, that can be used for diagnostic purposes.

5.1 Tin debris generation in the EUV source

As discussed in Sec. 1.3 there are various origins of liquid tin contamination in the EUV source chamber. First of all, not all drops coming from the drop generator are hit by a laser pulse. These missed drops continue their path and enter the tin catcher

where they impact onto a liquid pool as shown in Fig. 1.5(a). The function of this tin catcher is to trap the drops after impact such that no (parts of the) drops can escape into the source chamber. For the design of the tin catcher it is important to understand in what direction splashed droplets are expected and how splashing can be suppressed.

Second, tin debris is generated when the incoming drops are hit by the laser pulse, since the liquid tin is not fully converted into plasma as shown in Fig. 1.5(c). This tin debris is ejected in all directions and impacts onto the side walls of the source chamber and the collector mirror (see Fig. 1.5). Drops that impact onto the collector mirror solidify during impact since the collector mirror is kept at low temperatures to enhance its performance. The area contaminated by the drop has to be minimal to maximize the EUV reflection. Drop spreading has thus to be minimized. At the same time drop splashing has to be suppressed since the small secondary droplets create another location where tin debris impacts. Side walls might not have a temperature restriction, such that a substrate temperature can be chosen to minimize the contamination. However, one has to take into account that these side walls will be covered with a layer of solidified tin from previous impacts, which may alter the impact behavior.

Once the temperature of these side walls is above the melting temperature of tin, previously impacted drops will form a liquid layer. Soon enough, this liquid layer becomes a deep liquid pool for tiny incoming drops: For a 100 nm-drop, a micron-sized layer is already a deep liquid pool. Depending on the orientation of the side walls new tin debris impacts obliquely onto this deep liquid pool. It is important to understand the direction at which splashed droplets are expected for the design of the side walls.

Third, liquid tin debris can accumulate at the ceiling of the source chamber for substrate temperatures above the melting temperature of tin. When too much tin has accumulated, the liquid tin becomes unstable and drops are dripping because a Rayleigh-Taylor instability develops. These drops fall down under the influence of gravity and are therefore relatively large and slow. They impact onto the lower side walls where the orientation of those side walls determines the direction at which splashed droplets are expected.

And fourth, liquid tin debris is generated when hydrogen radicals recombine in a liquid tin layer and from bubbles. When these bubbles burst at the surface, small droplets are ejected, which is called spitting.

Because of all these effects, the tin drops in the EUV chamber cover a wide range of dimensions and velocities depending on their origin. Tin debris created after laser pulse impact typically are 100 nanometer-sized and have velocities of 100 m/s (Re $\approx$ 40,000 and We $\approx$ 13,000) while tin drops coming from the drop generated are 50 micrometer-sized and have a velocity of 20 m/s (Re $\approx$ 37,500 and We $\approx$ 250). The relatively large drops dripping from the top side walls are typically 3 millimeter in size

and have a velocity of 3 m/s (Re $\approx$ 37,000 and We $\approx$ 350). When solidification does not play a role (Ste < 0, $T_s > T_m$), the fluid dynamic response of a tin drop impact is governed by the Weber and Reynolds number, as discussed in Sec. 1.4.

Exploiting the concept of dynamic similarities (see Sec. 1.4) we can use the results obtained for obliquely impacting water drops in Chap. 2 to learn about the situation in the source chamber. As a consequence, the $D = 100$ μm water drop impacting with $U = 5$ to 25 m/s in our water experiments can be compared to a tin drop of $D = 6.5$ μm and $U = 20$ to 100 m/s which resemble typical drops present in the source. The translation of our results relevant for EUV will be given in Sec. 5.2. To determine the effect of substrate temperature on spreading and splashing we studied tin drop impact in Chap. 3, since the dynamic similarities of water and tin do not hold when thermal properties are important. In Sec. 5.3 we reflect on how our results are of importance for EUV and we study how the impact dynamics are changed when the substrate is coated with a thin, solid layer of tin. We will also use the results obtained in Chap. 3 to provide a post-analysis tool to determine the impact conditions of the drop from the solidifed splat to be able to locate the origin of the impacting drops in Sec. 5.4.

5.2 Suppress splashing by controlling the impact angle *

5.2.1 Conditions for splashing

We now use the results of Chap. 2 to see how the impact angle can be used to control the direction of splashing after impact onto a deep liquid layer. A schematic view of a possible outcome is shown in Fig. 5.1. When a drop impacts a deep liquid pool obliquely, different outcomes of the impact are possible: deposition, single-sided splashing (front-splashed droplets) and omni-directional splashing (front and back-splashed droplets). For experimental examples we refer to Fig. 2.3(a). We measured drop impacts for a wide range of We and impact angles α, as shown in Fig. 2.3(b). Following the theory described in Chap. 2, we find that there is a transition from deposition to single-sided splashing and from single-sided splashing to omni-directional splashing (Eq. (2.4))

$$\mathrm{We}^{1/2}\mathrm{Re}^{1/4}(\cos\alpha)^{5/4}\left[1 \pm c\tan\alpha\right] > K. \tag{5.1}$$

The range where we measured (We $\lesssim 1000$) is relevant for tin drops coming to the tin catcher and for dripping drops. To directly capture the tin debris generated by the laser pulse impact, we extrapolate our model to high We. Then Eq. (5.1) reduces to $(\cos\alpha)^{5/4}\left[1 \pm c\tan\alpha\right] > 0$. The transition to splashing then occurs at $\cos\alpha > 0$,

* The findings in this subsection are used for an internal General Information Document at ASML.

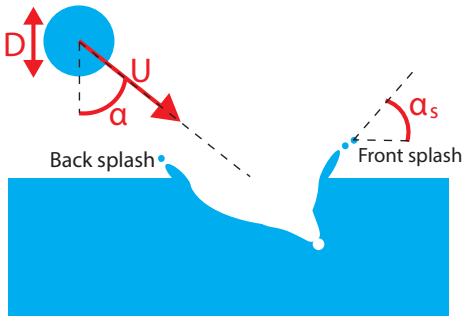

Figure 5.1: Schematic view of an impacting drop. Impact angle α, impact velocity U, drop diameter D and angle of the splashed droplet α_s are indicated in this figure, as well as the front and back splashed droplet(s). Below the water surface a cavity is formed, as studied in detail in Sec. 2.4.

which gives $\alpha < 90^\circ$ for the limit to omni-directional splashing, which corresponds to the case where $\pm$ is a $+$. In the limit to single-sided splashing we find $1 - c\tan\alpha > 0$, which gives $\alpha < \arctan(1/c) \approx 66^\circ$ when $c = 0.44$ is used as found in Sec. 2.3.2. The predicted transitions from this extrapolation are shown in Fig. 5.2.

This extrapolation is based on the same assumptions describe in Sec. 2.3.2. These assumptions imply that splashing is observed once the drop has fully impacted and that the volume of the crown consists of liquid from the impacting drop only. From numerical simulations for perpendicular impact onto a (deep) liquid layer [1, 2] we already observe that the crown consists of liquid of both the drop and the layer. When We approaches very large values, the crown volume may primarily consist of liquid from the pool, rather than from the drop. Once this is the case our extrapolation loses its validity. However, numerical simulations have to reveal the composition of the crown at high We.

If the extrapolation holds at high We, the limiting values show that it is possible to suppress omni-directional splashing for all We by keeping the impact angle above 66° (Fig. 5.2). Complete suppression of splashing is not possible since at $\alpha = 90^\circ$ a drop splashes always on a single side for large enough We ($\mathrm{We} \gtrsim 10^4$) as seen from Fig. 5.2. A schematic view of the outcome of the impact for different impact angles is shown in Fig. 5.3(a). This gives a clear guideline for design within the EUV source. As the origin of the drops can not be altered, the orientation of the substrate has to be adapted to prevent drop impact below $\alpha < 66^\circ$ to exclude omni-directional splashing. The single-sided splash occurs only in the direction away from the impact location (see Fig. 5.1). Therefore these splashed droplets can be disposed away: Namely, when the side walls are covered with structures the front-splashed droplets can be trapped

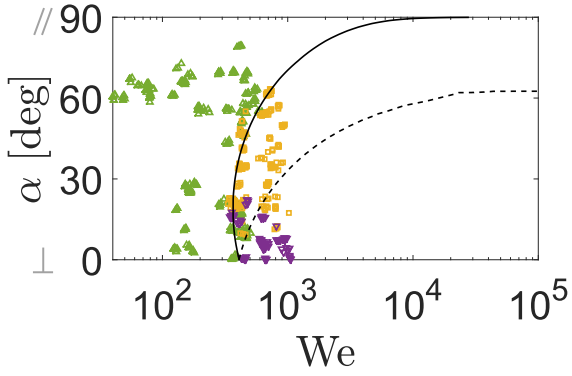

Figure 5.2: Extrapolated phase diagram of the impact behavior as a function of We and α. Upward green triangles represent deposition, yellow squares represent single-sided splashing, and downward purple triangles represent omni-directional splashing. The solid and the dashed lines are derived from Eq. (2.4) with $c = 0.44$, where the solid line represents the splashing threshold from deposition to single-sided splashing (Eq. (2.4) with plus sign) and the dashed line indicates the splashing threshold from single-sided splashing to omni-directional splashing (Eq. (2.4) with minus sign). The single-sided splash results in front splashed droplet(s) only, while the omni-directional splash results in both front and back-splashed droplets. The limit for single-sided splashing is at 90°, while the limit for omni-directional splashing is found at 66°.

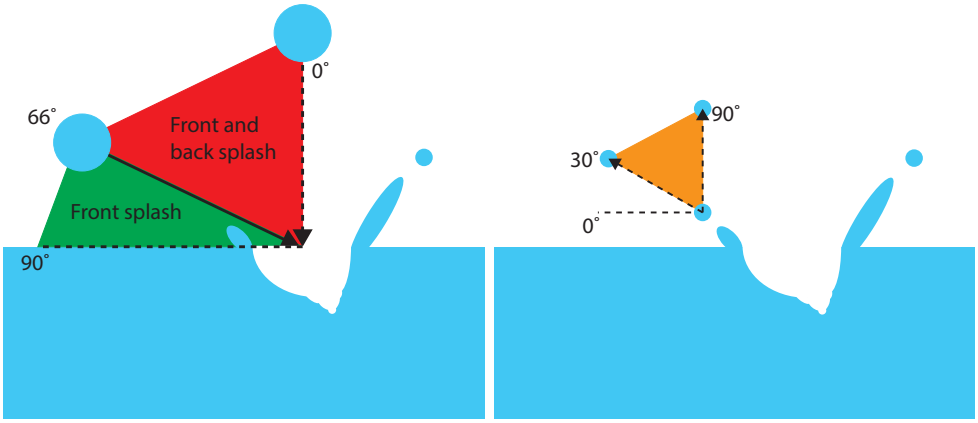

(a) (b)

Figure 5.3: Schematic view of the splashing behavior depending on impact angle. (a) When a drop impacts with an angle larger than 66° (green area) there is no back splash. Drop impacts with an angle less than 66° (red area) may result in a back splash. (b) In our measurement regime we only observe back-splashed droplets with a minimal angle of 30° from the pool surface (orange area).

inside these structures. Front-splashed droplets inside the tin catcher can go deeper into the tin catcher. Both the front-splashed droplets trapped inside the structures at the side walls and the front-splashed droplets trapped in the tin catcher can prevent further contamination of the source chamber.

5.2.2 Characterization of secondary debris

We now turn to the situation where we consider secondary tin debris generated during splashing. When splashed droplets impact and splash again, more small tin debris goes into the source chamber. To prevent this secondary source of tin debris, new impact of the splashed droplets has to be controlled. As discussed above, front-splashed droplets can be trapped inside structures applied at the side walls. Therefore, it is important to know the direction, size and velocity of these droplets. Back-splashed droplets are more difficult to trap, since these droplets go into the direction where the original drop comes from (see Fig. 5.1). These droplets can not be trapped inside structures, but applying (hydrogen) flows in the source chamber can change the direction of the splashed droplets. However, the droplet characteristics have to be known to apply a flow where the droplets will follow the streamlines and can be disposed away.

To this end, we measure the angle of both the front and the back-splashed droplets of the experiments performed in Chap. 2 (as defined in Fig. 5.1) as a function of the impact angle as shown in Fig. 5.4. For the back-splashed droplet we observe a minimal

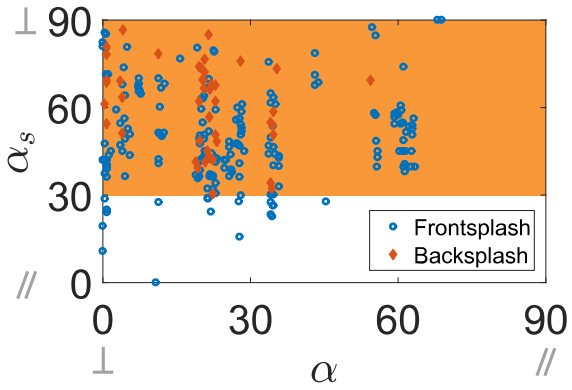

(a)

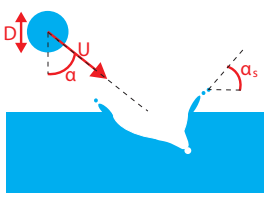

(b)

Figure 5.4: (a) Angle of the splashed drop as function of the impact angle. Blue open circles indicate the front-splashed droplets, red filled diamonds the back-splashed droplets. The back splashed droplet has a minimal ejection angle of 30° in our measurements. (b) Adopted from Fig. 5.1. Schematic view of an impacting drop. Impact angle α, impact velocity U, drop diameter D and angle of the splashed droplet α_s are indicated in this figure.

angle of 30° for our measurement range. By contrast, the front-splashed droplets cover the full range. In other words: no matter what impact angle the impacting drop has, a back splash with an angle less than 30° does not occur, as shown schematically in Fig. 5.3(b). No dependence of the splashing angle on We is found from our measurements. Experiments or numerical simulations have to confirm whether or not a dependence of splashing angle on We exists at high We.

Next we determine the droplet sizes and velocities of the front and back-splashed droplets. In Fig. 5.5(a) we report the size of the splashed droplets D_s as obtained in our measurements. It seems that the size of the splashed droplets for $\alpha \approx 0°$ is smaller than the size for larger α. Most of the splashed droplets are up to 30% of the size of the impacting drop, but a lot of spread in the data is found. Typically the sizes of the back-splashed droplets are smaller (maximal $\approx 15\%$ D) than the sizes of the front-splashed droplets, such that they follow an applied flow more easily. Not all sizes of the splashed droplets could be measured due to focusing issues. Then, we determine the velocity of the splashed droplets U_s as shown in Fig. 5.5(b). The velocity of the splashed droplets is of the same order as the impact velocity, with the velocity of the back-splashed droplets slightly smaller than the velocity of the front-splashed droplet. It seems that for high We the restitution coefficient U_s/U decreases. However, this might be due to the limited data available at high We or to imaging limitations, where the splashed droplet cannot be measured for two consecutive frames.

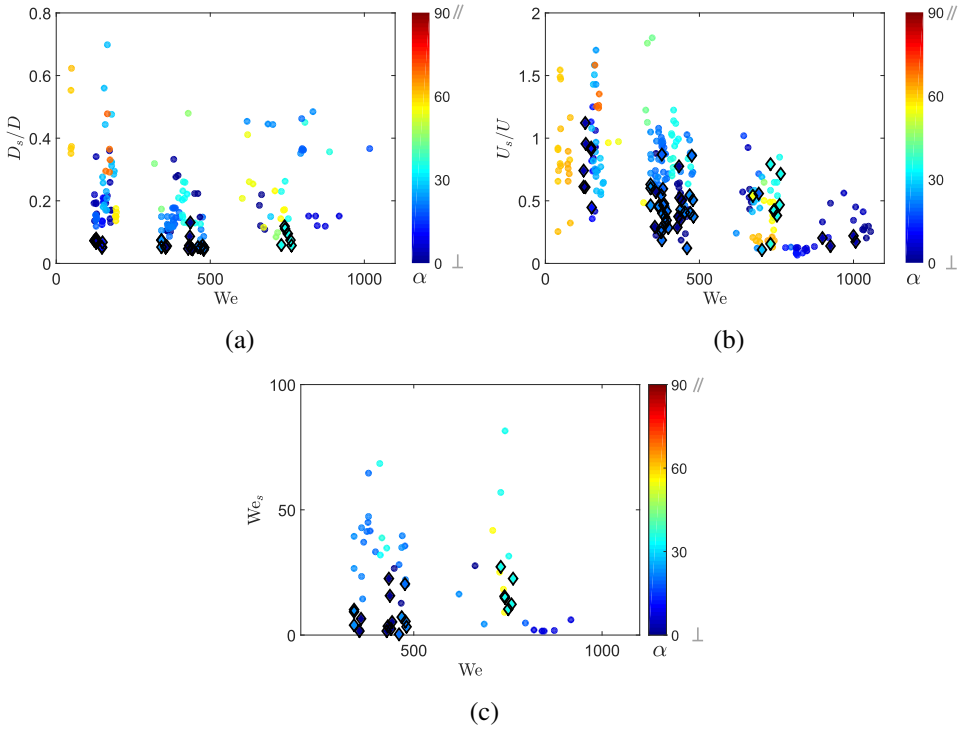

Figure 5.5: The dimensionless diameter (a), dimensionless velocity (b) and the Weber number of the splashed droplets (c) of the splashed droplets as a function of the Weber number of the incoming drop. The front splashed droplets are indicated by circles, the back-splashed droplets by diamonds. The color bar indicates the impact angle. (a) The diameter of the splashed droplet is (much) smaller as compared to the impacting drop. The mean size of the back splashed droplet is smaller than the front splashed droplet. (b) The velocity of the splashed droplets is comparable to the velocity of the impacting drop for all We. The apparent trend of decreasing U_s/U with increasing We might be due to a lack of measurements or imaging limitations in this regime. (c) $\mathrm{We}_s = \rho D_s U_s^2/\gamma$ as compared to We. We_s is around 10 times smaller than We, mostly due to the smaller size of the splashed droplets, as shown in (a). There are fewer data points shown in (c) as compared to (a) and (b), since the droplets have to be in focus for at least two consecutive frames to measure both diameter and velocity accurately.

From the size and velocity of the splashed droplets we can now calculate the Weber number of the splashed droplets $We_s = \rho D_s U_s^2/\gamma$, as shown in Fig. 5.5(c). The number of data points is reduced as compared to D_s and U_s. To calculate We_s both D_s and U_s are needed, while for some experiments only one of the two can be measured as discussed above. In general, we observe that We_s reduces by a factor of around 10 with respect to the original We, which is mostly due to the decrease in droplet size. This reduction of We_s makes it more difficult to splash for the secondary droplet. We note that We_s is typically lower for the back-splashed droplets as compared to the front-splashed droplets, which is a similar trend as observed for D_s.

5.2.3 Summary

Let us summarize our main findings of this section, relevant for the design of the EUV source chamber. For high We it is not possible to completely suppress splashing. However, by controlling the impact angle such that $\alpha > 66^\circ$ back-splashed droplets can be prevented (Fig. 5.3(a)). The front-splashed droplets can be caught further in the tin catcher or deeper into possible structures at the side walls. Since the Weber number for the splashed droplets We_s is approximately 10 times smaller than We (Fig. 5.5(c)), splashing of the secondary front-splashed droplets after impact can be more easily suppressed.

When the impact angle is between $0 < \alpha < 66^\circ$ both front- and back-splashed droplets can be observed depending on We (Fig. 5.2). The back-splashed droplets are the most difficult to catch, since they are ejected towards the origin of the original drop (Fig. 5.1). Since the size of these droplets is less than 15% for our measurements (Fig. 5.5(a)) flows applied in the source chamber can be used to alter the direction at which these droplets are going to prevent these droplets going towards the origin of the impact drop (Fig. 5.3(b)).

5.3 Suppress splashing by controlling the substrate temperature

In Chap. 3 we studied how the spreading and splashing behavior is altered by the substrate temperature. We measured liquid tin drop impact onto a sapphire substrate of controlled temperature and used side and bottom-view imaging to describe the impact dynamics. While we studied a smooth, clean substrate in Chap. 3 during operation the side walls of the source chamber can be contaminated by a tin layer from previous drop impacts. In this section we therefore first discuss the lessons learned on a smooth, clean substrate. Second, we focus on drop impact onto a substrate with a tin coating to mimic the situation at the side walls during operation.

5.3.1 Spreading and splashing on clean substrates

In Sec. 3.4.1 we measured a limited spreading once the substrate temperature is lowered, as shown in Fig. 3.6(a). We modeled the maximum spreading to account for the influence of substrate temperature and we found

$$\frac{D_{max}}{D} \sim 0.9 \left(\frac{DU}{\kappa} \frac{L}{c_p \Delta T} \right)^{1/5}, \tag{5.2}$$

as presented nondimensionally in Eq. (3.6). From this one would conclude that the lower the substrate temperature the more the spreading is limited. At the same time however we showed that at low substrate temperature freezing-induced splashing is promoted (see Sec. 3.4.3 and Fig. 3.8(b)). When a drop splashes another location also gets contaminated, which increases the total area where contamination can be found.

From here we learn that an optimal substrate temperature depends on the exact requirements of the impact location. For impact onto side walls it is critical to prevent the generation of secondary droplets. At intermediate substrate temperature (Ste ≈ 0.3 for our experiments), the Weber number where the first splashing event is observed is at a maximum (Fig. 3.8(b)). For tin drop impact, Ste ≈ 0.3 implies that a substrate temperature of $T_s \approx 150°$C is optimal to suppress splashing. Since splashing depends on the actual substrate properties such as roughness and contact angle, for different substrates the exact values for the first splashing event as function of substrate temperature remain to be tested experimentally.

For impact onto the collector mirror the total area that is contaminated has to be minimal to maximize the EUV reflection. To minimize the spreading the substrate temperature has to be as low as possible, as shown in Fig. 3.6(a). Therefore the area contaminated by impacting drops is minimal for the lowest substrate temperatures. However, there is a complication: At these low substrate temperatures, freezing-induced splashing is promoted. This will not lead to a significant increase in contaminated area of the first impact drop, but it might influence the spreading and splashing dynamics of later impacting drops. As a result, the minimum total area that is contaminated after multiple impacts at locations close to each other might be found at a different substrate temperature.

5.3.2 Spreading and splashing on substrates with a tin coating

During operation previous impacted drops may have formed a layer of tin on top of the side walls. This layer of tin can influence the drop impact dynamics, since the layer can interact with the incoming tin drop. To study whether or not this tin layer is of influence on the drop impact dynamics we perform new experiments of single tin drop impacts onto a stainless steel substrate of controlled temperature with a 10 to 20 micrometer thick tin coating ($h \ll D$). We measure the impact dynamics and we focus

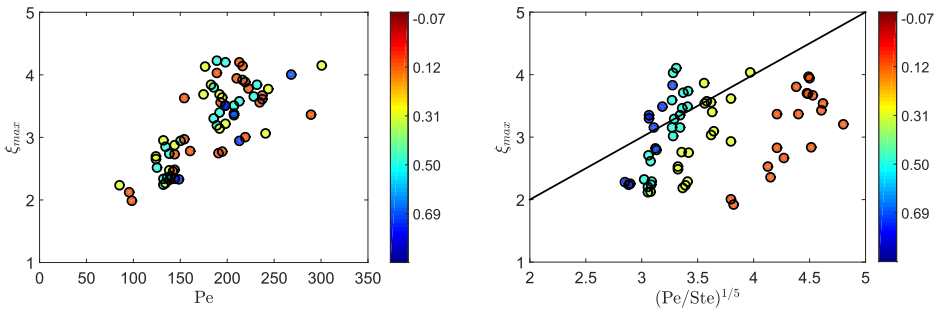

(a) (b)

Figure 5.6: (a) ξ_{max} as function of Pe for different Ste (color bar). The maximum spreading measured increases with increasing Pe, but seems not to depend on substrate temperature. (b) ξ_{max} as function of $\mathrm{PeSte}^{1/5}$ for different Ste (color bar). The solid line corresponds to Eq. (3.6) with prefactor 1. From here it is seen that Eq. (3.6) does not show the right scaling since no data collapse is observed.

on the differences found for impact onto a temperature controlled sapphire substrate and a temperature controlled stainless steel substrate with a tin coating.

We start by measuring the maximum spreading of the drop. Since bottom-view images are obscured from view by the substrates opaqueness spreading can only be measured by side-view imaging. On top of that, the analysis is restricted to bouncing and deposition, as for splashing drops the spreading radius cannot accurately be determined due to formation of ligaments. As a result the range of Pe (U) that can be measured is limited. In contrast to the measurements onto a sapphire substrate, we measure the end of the ligaments and therefore a larger spreading as compared to Sec. 3.4.1, where we measured the equivalent diameter of the spreading drop. The maximum spreading is shown as a function of Pe in Fig. 5.6(a). We observe that the maximum spreading increases with Pe. The substrate temperature does not have an influence on the maximum spreading, since the measurements for different substrate temperature form a cloud.

As a check for the lack of dependence of maximum spreading on substrate temperature we show the same data a function of $\mathrm{Pe/Ste}^{1/5}$, as is found from Eq. (3.6). When the stainless steel substrate with tin coating would show the same maximum spreading as function of temperature as the sapphire substrate this rescaling would give a collapse of all data. However, it is clearly seen that the data does not collapse, so the maximum spreading is altered by the tin coating on top of the stainless steel substrate.

A possible explanation for this deviation is found by considering the tin coating. Since this layer is made of the same material as the impacting drop, the drop can

melt this layer once the energy to melt the tin coating is smaller than the energy coming from the liquid drop that diffuses into the tin coating. The energy to melt the tin coating is given by $E_m \sim (c_p \Delta T + L)M$, which is the energy it takes to heat the tin coating to its melting temperature and the energy to actually melt the tin coating, respectively. Here, $M = \rho h D^2$ the mass of the tin coating that has to melt and $\Delta T = T_s - T_m$ the temperature difference between the tin coating at the substrate and the melting temperature of tin. The diffusive energy to melt this tin coating is provided by the impacting drop. This diffusive energy has to be transported over the thickness of the tin coating with a certain temperature. The thermal diffusivity determines the amount of energy that can be transported, the area and the duration determine where and how long the energy diffuses into the tin coating. This energy is given by $E_d \sim \iint k(\partial T/\partial y) dA dt \sim k(\Delta T/h) D^2 t_i$, with $t_i = D/U$.

By comparing the available energy E_d and the energy necessary to melt the tin coating E_m we see that for every impact experiment we performed $E_d > E_m$. High impact velocity $u = 5$ m/s and high substrate temperature $T_s = 200°$C experiments have the least diffusive energy available $E_d \approx 150$ mJ for a 2-millimeter drop. The energy to melt the tin coating in this case is $E_m \approx 18$ mJ, which is much less than the available energy. From here we conclude that for every impact experiment we performed the diffusive energy in the drop is high enough to melt the tin coating, as shown schematically in Fig. 5.7. By melting this layer the heat transfer for the process is changed, which alters the maximum spreading. Next to that, the substrate properties are changed since an indentation is created by melting the tin coating. Therefore, the maximum spreading is influenced and no dependency on substrate temperature is found, as shown in Fig. 5.6.

Besides the maximum spreading we also measure the splashing threshold for tin drop impact onto a stainless steel substrate with a tin coating. Figure 5.8(a) shows all our experiments. At $T_s = 200°$C we observe (partial) bouncing drops for low We and in a few experiments we observe deposition. When We increases the drops are splashing. For lower substrate temperatures, no bouncing events are observed. At low We the drops are deposited while for increasing We splashing is observed.

From these measurements we measure the transition to splashing by considering the first splashing event and the last bouncing/deposition event as shown in Fig. 5.8(b). In contrast to the transition to splashing on a sapphire substrate (Fig. 3.8(b)) the transition to splashing on a stainless steel substrate with a tin coating does not depend on substrate temperature. The first splashing event is observed for $50 < \mathrm{We} < 135$ and the last bouncing/deposition event is observed for $140 < \mathrm{We} < 175$ for all substrate temperatures. Hence, the transition regime significantly is smaller for all substrate temperatures measured as compared to the impact events on a sapphire substrate, where the last deposition event increased above the limit of our setup for low substrate temperatures. Next to the fact that the transition regime is smaller, the transition to

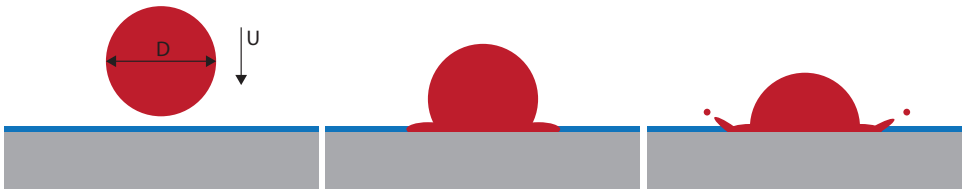

Figure 5.7: Schematic views of tin drop impact onto a tin-coated stainless steel substrate below the melting temperature of tin. The tin coating is visualized as the blue layer. (a) The drop before impact with diameter D and impact velocity U. A thin layer of solid tin (blue) is on top of the stainless steel substrate (gray). (b) During impact the high temperature of the liquid tin drop melts the tin coating. At parts where the drop has impacted this melting results in an indentation at the solid substrate. (c) When the drop spreads further it feels the unevenness of the substrate. The maximum spreading is therefore influenced since the substrate properties change during the impact event. Next to that the indentation might trigger corrugations to grow over time and splashing is promoted.

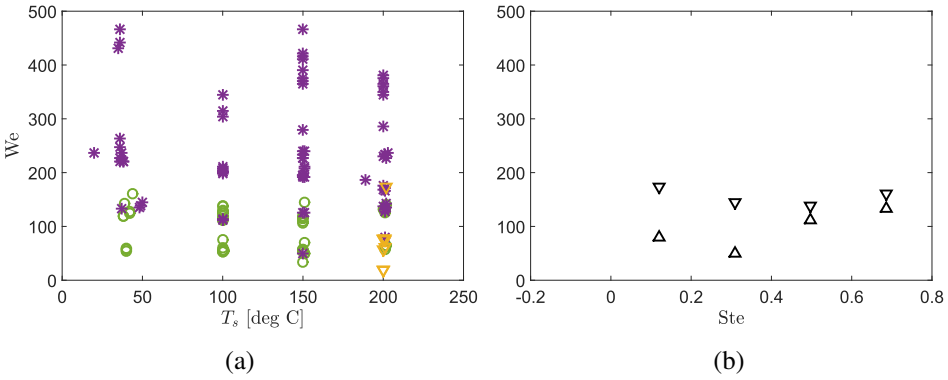

Figure 5.8: (a) Phase diagram of the impact behavior for drop impact onto a tin-coated substrate with varying substrate temperature. The orange triangles denote bouncing events, the green circles denote deposition and the purple stars show splashed drops. (b) Non-dimensional plot of the first splashing event (△) and last non-splashing event (▽) measured as function of We and Ste. Splashing is first observed for relatively low We and shows no significant dependence on substrate temperature.

splashing starts at lower We than for impact on a sapphire substrate.

The fact that the splashing events start at lower We on the stainless steel with tin coating than on the sapphire substrate can be due to substrate properties such as roughness or thermal conductivity. A possible explanation for the missing temperature dependence is found in melting the tin coating, as discussed for the spreading measurements. The substrate temperature does not influence the outcome of an impact event when the tin coating melts during impact. The indentation created by melting of the tin coating can trigger corrugations in the drop to grow (see Fig. 5.7) and therefore splashing is promoted.

These results imply that the temperature of tin-coated side walls of the source chamber can not be tuned to minimize drop spreading or splashing. As long as the substrate temperature is below the melting point of the tin, the impact dynamics are not altered significantly as function of the substrate temperature. However, the influence of the ratio of the thickness of the tin coating and the impacting drop h/D remains to be studied as it may influence the dependence on substrate temperature.

5.4 Determine impact conditions from solidified splat

In the EUV source tin debris is found on different parts of the machine. Often, the origin of these drops (direction, size, velocity) is unclear. However, it is only possible to examine the debris from retrospective analysis, i.e. after operation of the source. This makes it difficult to determine the impact conditions of the drops. In this section, we discuss how a witness sample that collects drops that solidified inside the source at a specified temperature can be used to determine the origin and impact conditions of the drops retrospectively. These results can then be used for engineering purposes to get a better quantification of the debris present in the source. This analysis is only applicable for single drop impact events since the impact behavior of a second drop will be changed by the splat of the first drop.

Once a drop has impacted onto a cold witness sample ($T < T_m$) it forms a solidified splat. The mass of this splat M is related to the size of the original drop by

$$D = \left(\frac{6M}{\pi \rho} \right)^{1/3}, \tag{5.3}$$

assuming that the mass of possible splashed droplets is negligible.

When a drop impacts under an angle the shape of the splat becomes asymmetric, as shown in Fig. 5.9. The eccentricity of the splat can be used to determine the impact angle of the drop. Ligaments may be more pronounced in the direction of the impact as compared to other directions due oblique impact [3, p.36–43]. We decompose the impact velocity in a perpendicular ($\perp$) and a parallel ($\parallel$) component such that $U_\perp = U \cos\alpha$ and $U_\parallel = U \sin\alpha$, with α the impact angle of the drop. We assume that

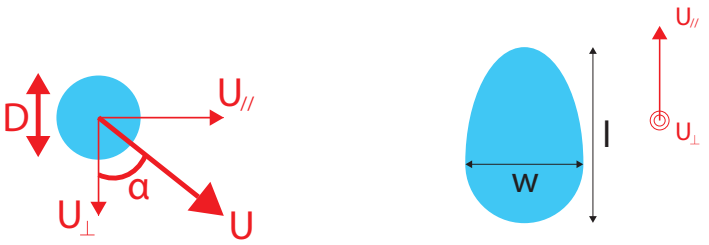

(a) (b)

Figure 5.9: (a) Side view showing the drop impact angle α with diameter D. Impact velocity U is decomposed into a parallel $\parallel$ and a perpendicular $\perp$ component. (b) Top view of the asymmetric splat after impact. The width of the splat w is determined by $U_\perp$, while the length of the splat l is set by U.

the width of the splat w is determined by the perpendicular velocity $U_\perp$ only and the length of the splat l is determined by the impact velocity U, in analogy to the cavity formation as discussed in Sec. 2.3.3. Furthermore, we assume solidification limits the drop spreading in the same way in all directions as given by Eq. (3.6). We then find [3, p.36–43][4–6]

$$\frac{w}{l} \sim \frac{U_\perp^{1/5}}{U^{1/5}} \sim (\cos\alpha)^{1/5}. \tag{5.4}$$

The impact velocity is determined from the splat size. We use the model of Eq. (3.6) where the maximum spreading diameter is related to the impact velocity and the substrate temperature. Since the drop solidifies during impact and no retraction is observed $w = D_{max}$, which gives $w/D \sim 0.9(\mathrm{Pe}_\perp/\mathrm{Ste})^{1/5}$ and thus, using $U_\perp = U\cos\alpha$,

$$U_m \sim \frac{1}{\cos\alpha}\frac{1}{0.9^5}\frac{\kappa}{D}\frac{c_p\Delta T}{L}\left(\frac{w}{D}\right)^5, \tag{5.5}$$

with U_m the impact velocity calculated by the model of Eq. (5.5) and 0.9 the prefactor as used in Eq. (3.6).

We now test the retrospective analysis described above. We collect several splats after impact onto a sapphire substrate. These splats can be removed from the substrate and no additional material is attached to the splat. Drops impacting onto the stainless steel substrate with tin coating are not used, since the drops stick to the substrate. Next to that, part of the tin coating might adhere to the splat therefore altering the size and velocity found by the model. Since oblique impact onto cold substrates was not studied we cannot validate Eq. (5.4).

For a few measurements, the analysis is shown in Tab. 5.1. The velocity calculated from the model is compared to the experimental velocity and shows relatively good

Table 5.1: Experimental parameters and model predictions of three splats. The images are not shown to scale. The model gives a reasonable estimate for the impact velocity, but the uncertainty is quite large.

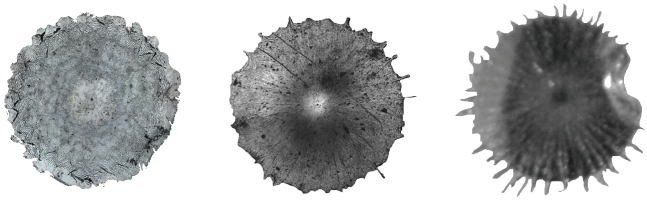

Measured parameters			
U [m/s]	2.49	3.49	3.63
T_s [°C]	40	100	150
Mass [mg]	15	45	64
D_{max} [mm]	4.0	7.7	9.6
Model predictions			
D [mm]	1.7	2.4	2.7
U_m [m/s]	2.13	3.89	3.99
Comparison			
$U_m/U \cdot 100$ [%]	86	111	110

agreement for these examples. The measured velocity is found from the impact height at which the drops are generated, which is known for the collected splats.

The comparison of U_m with U for more analyzed splats is shown in Fig. 5.10, where U_m varies from 86 to 143% of U. We observe reasonable agreement between model and experiment. For $T_s > 50$°C (Ste < 0.6) only a few data points could be obtained due to sticking of the drop to the substrate (no self-peeling). For low substrate temperatures and high impact velocities the model overestimates the impact velocity. This overestimation can be accounted for when the impacting drop splashes violently and a lot of secondary droplets are ejected. The mass of the ejected droplets can become so high that it is no longer negligible to the total mass of the impacting drop. The measured mass of the drop is thus too low resulting in a smaller drop diameter, which gives an overestimation of U_m. To check whether the splashed droplets are causing the deviation from the model imaging of the impacting drops has to be done to measure the size before impact and to observe the outcome of the impact.

In summary, the retrospective analysis performed in this section can be a very powerful tool to determine the impact conditions from the remaining splat once the substrate temperature is known. The drop diameter is calculated from the mass of the splat (Eq. (5.3)). The mass of a splashing drop is underestimated because

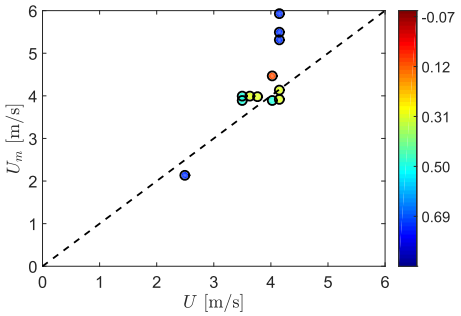

Figure 5.10: Validation of the retrospective analysis of Eq. (5.5) by the maximum spreading model of Eq. (3.6). U is compared to the velocity given by the model of Eq. (5.5) U_m for different Ste (color bar). The dashed line has slope unity. The measured points deviate from the model, but a rough estimate of the impact velocity can be made.

the secondary droplets are detached and thus not measured. Since we only study perpendicular impact we cannot confirm Eq. (5.4). The velocity of the impacting drop is calculated (Eq. (5.5)) using the spreading model on a cold substrate discussed in Sec. 3.4.1. By comparing the velocity found from the analysis by the velocity found from the measurements itself we find reasonable agreement. For drops impacting with a high velocity onto a cold substrate the analysis overestimates the impact velocity, since these drops might loose a significant amount of mass via splashed droplets. As a results, a smaller drop diameter is calculated, which gives an overestimation of the calculated impact velocity. Therefore it is difficult to extract the exact impact conditions of the drop, but a reasonable estimate is obtained. As such, this method can serve as a very promising diagnostic to quantify key aspects of tin debris in the EUV source, in particular their direction, sizes and velocities.

5.5 Conclusion and outlook

In this chapter, we studied the suppression of the generation of splashed droplets for oblique drop impact (Sec. 5.2) and solidification during impact (Sec. 5.3). We also measured the direction, size, and velocity of the splashed droplets after oblique impact to control where these droplets go. Finally, in Sec. 5.4 we determined the impact conditions of liquid tin drops from the solidified splats.

While here we focused on preventing secondary droplets by suppression of splashing, let us briefly comment on other possible sources of tin debris generated after impact that need to be prevented. After a drop impacts onto a liquid pool, closure of the induced cavity can lead to the formation of a (Worthington) jet from which

secondary droplets may detach. The impact conditions of these secondary droplets remain to be quantified. Next to that, during operation multiple drops will impact shortly after each other and the drop impact dynamics are not isolated. The effect on spreading and splashing of multiple drop impacts remains to be studied in future work.

Let us close by some further remarks based on the findings in this thesis. To enhance the in-situ cleaning of the collector mirror, it might be beneficial to keep the substrate temperature low. When the drop solidifies quickly after impact stresses inside the bulk may cause the drop to peel from the substrate [7], which makes it easy to remove the drop from the substrate. The exact conditions for peeling at the collector mirror have to be studied, as well as an in-situ method to remove those splats. Finally, having seen the influence on splashing of all these parameters individually, it would be of interest to study the combined effect on splash suppression. One can think of using an elastic material at low temperature where the drops impact obliquely to study how splashing is suppressed. However, it is a challenging task to find a material with these properties that can be used due to the extreme conditions in the source chamber, such as high vacuum, high temperature and the presence of (liquid) tin.

References

[1] S. Yang, Y. An, and Q. Liu, “Effect of viscosity on motion of splashing crown in high speed drop impact”, Appl. Math. Mech. (2017).

[2] G. Agbaglah, M.-J. Thoraval, S. T. Thoroddsen, L. V. Zhang, K. Fezzaa, and R. D. Deegan, “Drop impact into a deep pool: vortex shedding and jet formation”, J. Fluid Mech. **764** (2015).

[3] S. H. James and W. G. Eckert, *Interpretationn of bloodstain evidence at crime scenes*, 2nd edition (CRC Press, New York) (1999).

[4] D. Attinger, C. Moore, A. Donaldson, A. Jafari, and H. A. Stone, “Fluid dynamics topics in bloodstain pattern analysis: Comparative review and research opportunities”, Forensic Sci. Int. **231**, 375 – 396 (2013).

[5] C. D. Adam, “Fundamental studies of bloodstain formation and characteristics”, Forensic Sci. Int. **219**, 76 – 87 (2012).

[6] C. Willis, A. K. Piranian, J. R. Donaggio, R. J. Barnett, and W. F. Rowe, “Errors in the estimation of the distance of fall and angles of impact blood drops”, Forensic Sci. Int. **123**, 1 – 4 (2001).

[7] J. de Ruiter, D. Soto, and K. K. Varanasi, “Self-peeling of impacting droplets”, Nat. Phys. (2017).

6 Summary and Outlook

As discussed in Sec. 1.1 many parameters influence the outcome of a drop impact event. In this thesis we showed how the drop's impact angle (Chap. 2), the substrate's temperature (Chap. 3) and the substrate's elasticity (Chap. 4) influence the impact behavior of the drop. In Chap. 5 we described the practical application of our work for the design of the EUV source chamber. Tin debris that impacts and subsequently splashes causes undesired contamination of the hardware in the source chamber. To prevent this contamination we studied how substrate properties can be used to suppress splashing. In this chapter, we briefly summarize our findings and discuss further possible implications and open questions.

6.1 Summary

6.1.1 Oblique drop impact onto a deep liquid pool

In Chap. 2, we studied oblique water drop impact onto a deep liquid pool and distinguished three different outcomes: deposition, single-sided splashing and omni-directional splashing. A model was developed to account for these different impact behaviors. In this model, it is assumed that the velocity component parallel to the liquid pool induces an asymmetric distribution of liquid mass over the crown. This asymmetric mass distribution in turn induces asymmetric (i.e. single-sided) splashing when the impact angle is far from perpendicular. In Chap. 5 we extrapolated our model and found impact angles at which omni-directional splashing does not occur. This information can be used in the design of the side walls and the tin catcher in the

EUV source.

Next to the splashing behavior, we also measured and modeled the cavity dynamics in Chap. 2. Our model revealed that the depth of the cavity depends on the perpendicular impact velocity only, while the cavity displacement depends solely on the parallel impact velocity. Our measurements confirmed this dependency. After the cavity has reached its maximum dimensions it collapses. During this collapse small secondary droplets may be ejected or an air bubble can be entrapped below the water surface. As discussed in Chap. 5, this collapse can be another source of tin debris formation in the EUV source chamber.

6.1.2 Solidification during tin drop impact

We studied the influence of substrate temperature on the impact behavior by measuring tin drop impact onto a sapphire substrate of controlled temperature in Chap. 3. Solidification of the impacting drop was found to strongly alter the impact dynamics. The maximum spreading is reduced and the number of ligaments formed by instabilities of the deforming drop decreases for impact events where the substrate is so cold that the liquid solidifies. Next to that, the transition to splashing is altered. On the one hand, the last deposition event observed rapidly increases to higher Weber numbers with decreasing substrate temperature. On the other hand, the first splashing event is measured at lower Weber number when the substrate temperature decreases.

When the substrate was changed to a stainless steel substrate with a tin coating, as shown in Chap. 5, we observed different outcomes of the impact event for similar impact conditions. The maximum drop spreading and the transition to splashing were found to be independent of the substrate temperature. A possible explanation was found in the melting of the tin coating during impact.

Furthermore, in Chap. 5 we demonstrated how the drop solidification during impact can be used for diagnostic purposes in the EUV source chamber. We provided a retrospective analysis tool to determine the drop impact conditions from the solidified splat. This tool allows one to determine impact angle, size and velocity when there is no optical access for high-speed imaging, such as in the EUV source.

6.1.3 Suppressed splashing on elastic membranes

We studied the influence of the elasticity of a substrate on drop splashing in Chap. 4. To this end, drops were impacted onto an elastic membrane that was placed under tension. We found an increase of the splashing threshold when the tension applied to the membrane was lowered such that the membrane could deform. We quantified the membrane deformation as a function of the tension and the impact velocity by profilometry measurements and we provided a model for this deformation. It was

found that the membrane deformation delays the formation of an ejecta sheet. As a result the ejecta is slowed down, which leads to splash suppression.

6.2 Outlook

In this thesis, we focused on the transition from deposition to splashing. Thereby we did not discriminate between the different kinds of splashes that exist: the prompt and corona splash (see also Chap. 1), while the characteristics of the splashed droplets depend on the kind of splashing behavior. When drops detach from an upward moving rim the splash called corona splash, while prompt splashing occurs earlier in time when droplets detach from the ejecta sheet [1, 2]. Depending on the exact time of ejection, the droplets will have different sizes, velocities and directions of motion. For a more detailed understanding of the characteristics of the splashed droplets it is therefore important to distinguish between the two different splashing mechanisms. How are the prompt and corona splash affected by the substrate elasticity or solidification?

The characteristics of the ejecta sheet determine whether a drop splashes from this ejecta sheet after impact or not. However, only few studies focused on the dynamics of the ejecta sheet as a function of the drop properties, such as drop size, viscosity or surface tension [3–5]. In Chap. 4, we assumed that the time at which the ejecta sheet is generated is delayed on elastic substrates, which leads to splash suppression. Despite the fact that our simple modification to the ejection time described the change in splashing threshold relatively well, it remains to be studied how the exact dynamics of the ejecta sheet depends on substrate elasticity. On cold substrates (Chap. 3) we observed that the last deposition event increases rapidly when the substrate temperature is lowered, which we attributed to solidification of the ejecta sheet. Next to the suppression of the splashing, we also observed that early solidification of the ejecta sheet reduces the maximum spreading and the number of ligaments. A more detailed experimental visualization and modeling of the solidifying ejecta sheet remains a challenge for future work.

All experiments carried out in this thesis were performed at ambient pressure. For impact onto rigid substrates, it is well known that reducing the ambient pressure helps to suppress splashing [6, 7]. In such case, the lift force on the ejecta sheet generated by the lubricating air layer below is reduced [5], thereby preventing the ejecta sheet to break up into secondary droplets. For drops impacting onto an elastic membrane (Chap. 4) a similar mechanism is expected to suppress splashing when the surrounding pressure is reduced. In contrast, splashing during impact on a liquid pool (Chap. 2) and freezing-induced splashing (Chap. 3) are expected to be unaffected by ambient pressure reductions. In particular, for solidifying drops splashing at low Weber number is triggered by the already solidified liquid that perturbs the remaining liquid. The splash formed during impact on a liquid pool (Chap. 2) is created by the

upward flow of liquid originating from the impact event, which is not affected by the ambient pressure [8]. However, the direction of the splash is affected by the density of the surrounding gas [9]. The investigation of the splash direction as a function of the surrounding pressure remains an important topic for future research, not only from a fundamental point of view, but also for application in the low-vacuum EUV source.

When splash suppression is successful, the transition moves to higher Weber numbers. Due to experimental limitations, such as encountered in Chap. 3, it therefore becomes harder to determine the splashing threshold experimentally. Numerical simulations can be of added value in these regimes. Next to their use for studying impact events outside the measurement range, numerical simulations can also provide a full three-dimensional view of the impact event. This 3D view enables measurements of splash characteristics at the full perimeter instead of in a two-dimensional field of view only. For example, in [10] the three dimensional splashing and cavity development during oblique impact were studied numerically and compared to the experimental results in Chap. 2, thereby providing a clear view on the transition from single-sided to omni-directional splashing. Numerical simulation also can reveal velocity profiles inside the drop or, in case of impact experiments on cold substrates, could potentially be used to study the growth of a solidification front.

In this thesis, we isolated three parameters and studied their influence on the splashing behavior of an impacting drop: the impact angle, the substrate temperature, and the substrate elasticity. One can also consider to combine some of the parameters to study their combined effect on splashing. We have seen that impact on a cold substrate promotes splashing, while less tension applied to an elastic membrane suppresses splashing. What happens when a liquid tin drop impacts onto an elastic membrane at temperatures below the melting temperature of tin? And can splashing and solidification in specific directions be suppressed by altering the impact angle on cold substrates? The control parameter space of drop impact is multidimensional and any thesis can only scratch at its surface.

References

[1] R. Rioboo, A. Tropea, and M. Marengo, “Outcomes from a drop impact on solid surfaces”, Atomization Spray **11** (2001).

[2] A. Yarin, “Drop impact dynamics: Splashing, spreading, receding, bouncing…”, Annu. Rev. Fluid Mech. **38**, 159–192 (2006).

[3] S. T. Thoroddsen, “The ejecta sheet generated by the impact of a drop”, J. Fluid Mech. **451**, 373–381 (2002).

[4] L. V. Zhang, J. Toole, K. Fezzaa, and R. D. Deegan, “Evolution of the ejecta

sheet from the impact of a drop with a deep pool", J. Fluid Mech. **690**, 515 (2012).

[5] G. Riboux and J. M. Gordillo, "Experiments of drops impacting a smooth solid surface: A model of the critical impact speed for drop splashing", Phys. Rev. Lett. **113**, 024507 (2014).

[6] L. Xu, W. W. Zhang, and S. R. Nagel, "Drop splashing on a dry smooth surface", Phys. Rev. Lett. **94**, 184505 (2005).

[7] A. Latka, A. Strandburg-Peshkin, M. M. Driscoll, C. S. Stevens, and S. R. Nagel, "Creation of prompt and thin-sheet splashing by varying surface roughness or increasing air pressure", Phys. Rev. Lett. **109**, 054501 (2012).

[8] L. Zhang, J. Toole, K. Fezzaa, and R. Deegan, "Splashing from drop impact into a deep pool: Multiplicity of jets and the failure of conventional scaling", J. Fluid Mech. **703**, 402–413 (2012).

[9] S. T. Thoroddsen, M.-J. Thoraval, K. Takehara, and T. G. Etoh, "Droplet splashing by a slingshot mechanism", Phys. Rev. Lett. **106**, 034501 (2011).

[10] B. Liu, "Numerical simulation of oblique droplet impact onto a deep liquid pool", Master's thesis, Delft University of Technology (2017).

Samenvatting

We zijn allemaal bekend met vallende regendruppels op verschillende soorten oppervlakken. Wanneer een regendruppel inslaat op een oppervlak zijn er verschillende uitkomsten mogelijk afhankelijk van de eigenschappen van zowel de druppel als het oppervlak. Ook in industriële toepassingen komen inslaande druppels voor, bijvoorbeeld in de extreem ultraviolet (EUV) lithografiemachines geproduceerd door ASML. In deze toepassing is het uiteenspatten van druppels na inslag een ongewenst effect, omdat dit vervuiling veroorzaakt. Daarom is er in dit proefschrift gekeken naar manieren om het oppervlak zodanig aan te passen dat het uiteenspatten van inslaande druppels beperkt wordt.

In hoofdstuk 2 is experimenteel onderzocht op wat voor manier de hoek waaronder een druppel inslaat op een vloeistofbad het uiteenspatten van deze druppel beïnvloedt. We maken hierbij onderscheid tussen drie verschillende gedragingen na inslag: het opgaan van de druppel in het vloeistofbad, het uiteenspatten met de richting van de inslag mee en het uiteenspatten in alle richtingen. De overgangen tussen deze verschillende gedragingen kunnen beschreven worden met een schalingsargument waarbij de eigenschappen van de druppel en de hoek van de inslag bepalend zijn. Naast het uiteenspatten van de druppel verandert ook de holte die de druppel in het vloeistofbad maakt van vorm als de inslaghoek verandert. Aan de hand van een energiebalans kunnen we achterhalen dat de diepte van deze holte bepaald wordt door de loodrechte component van de inslagsnelheid, terwijl de verplaatsing van het diepste punt van de holte bepaald wordt door de parallelle component van de inslagsnelheid.

Een druppel stolt tijdens inslag wanneer deze druppel inslaat op een oppervlak met een temperatuur onder de smelttemperatuur van de vloeistof. De invloed van het stollen van tindruppels tijdens inslag is experimenteel onderzocht in hoofdstuk 3. De maximale spreiding van een druppel wordt beperkt wanneer de druppel stolt tijdens de inslag. Onze experimentele resultaten kunnen goed worden verklaard met een model waarbij de druppel stopt met spreiden wanneer de dikte van de spreidende druppel gelijk is aan de dikte van de gestolde laag die tijdens de inslag groeit vanaf het koude oppervlak. We vinden een tweeledig effect van de oppervlaktetemperatuur op het uiteenspatten van de druppel. Aan de ene kant wordt het voor de druppel moeilijker om uiteen te spatten, omdat een deel van de druppel bevriest. Dit deel komt tot stilstand waardoor de kinetische energie van de druppel als geheel afneemt, en het

uiteenspatten wordt bemoeilijkt. Aan de andere kant wordt het uiteenspatten van de druppel bevorderd, omdat de gestolde laag onregelmatigheden op het oppervlak vormt die het uiteenspatten van de spreidende druppel vergemakkelijken.

In hoofdstuk 4 hebben we bekeken hoe het vervormen van een elastisch membraan het uiteenspatten van de inslaande druppel verandert. Hiervoor hebben we membranen van verschillende spankrachten gebruikt en hebben we de benodigde inslagsnelheid voor uiteenspatten bepaald. Daarnaast hebben we de bijbehorende membraanvervorming gemeten. We stellen een model op voor de membraanvervorming en gebruiken dit resultaat om het uiteenspatten van de druppel te beschrijven. Door het vervormen van het membraan wordt het tijdstip waarop het uiteenspatten van de druppel geïniteerd wordt, uitgesteld. Hierdoor is de snelheid van de spreidende druppel afgenomen, wat ervoor zorgt dat meer kinetische energie bij de inslag nodig is om deze uiteen te laten spatten.

In hoofdstuk 5 hebben we de focus gelegd op de toepassing van het eerder beschreven werk in de stralingsbron van de EUV lithografiemachines van ASML. Door de oriëntatie van een met vloeistof bedekt oppervlak aan te passen (hoofdstuk 2) kan het uiteenspatten van druppels in bepaalde richtingen onderdrukt worden. We extrapoleren ons model en leren dat het uiteenspatten in de richting waar de druppel vandaan komt onderdrukt kan worden wanneer de druppel parallel genoeg inslaat, hetgeen gebruikt kan worden als ontwerpregel voor de wanden van de stralingsbron. Daarnaast hebben we gezien dat de energie van de uiteengespatte druppels is afgenomen. Wanneer deze secundair gevormde druppels opnieuw inslaan, wordt het moeilijker om een tweede keer uiteen te spatten. Wanneer het oppervlak onder de smelttemperatuur van tin wordt gehouden, zal de druppel inslaan op een hard oppervlak met een dun tinlaagje van eerder ingeslagen druppels. De aanwezigheid van dit tinlaagje verandert de spreidingsdynamica en het gedrag van uiteenspatten aanzienlijk: waar in hoofdstuk 3 een duidelijk verband gevonden wordt tussen de oppervlaktetemperatuur en het spreiden of uiteenspatten, lijkt deze afhankelijkheid verdwenen wanneer het oppervlak bedekt wordt met een dun laagje gestold tin. Een verklaring hiervoor kan gevonden worden in het smelten van het dunne tinlaagje door de inslaande druppel, waardoor de eigenschappen van het oppervlak tijdens het inslaan veranderen. Als laatste hebben we gekeken of we kunnen achterhalen wat de eigenschappen van de inslaande druppel zijn geweest wanneer we de gestolde, gespreide druppel na inslag analyseren. De massa van de gestolde druppel geeft de grootte van de inslaande druppel en wanneer de oppervlaktetemperatuur bekend is, kunnen we aan de hand van de maximale spreiding van de druppel de inslagsnelheid achterhalen. We hebben een model opgesteld om de inslaghoek van de druppel te bepalen. Dit geeft een leidraad om te bepalen waar druppels vandaan komen en welke grootte en snelheid deze hadden, om zo de bron van de druppels te achterhalen en te karakteriseren.

Acknowledgements

Dit is misschien wel het meest gelezen hoofdstuk van dit proefschrift, en daarom ook de ideale gelegenheid voor mij om te benadrukken dat ik dit niet alleen voor elkaar heb gekregen. De afgelopen vierenhalf jaar heb ik in een leuk academisch team bij ASML gewerkt en hierdoor veel contact gehad met zowel de academische als de industriële wereld. Ongetwijfeld ben ik hieronder een aantal mensen vergeten te bedanken die wel een bijdrage hebben geleverd aan deze thesis: bij dezen alsnog bedankt!

Hanneke Gelderblom, tijdens mijn afstuderen benaderde je mij met de vraag of ik als PhD-student deel uit wilde maken van het project. Op dat moment had ik hier nog niet goed over nagedacht, maar ik kreeg hier de tijd voor en mocht ook een keer bij ASML kijken en kennis maken. Dit heeft er voor gezorgd dat ik met goede moed aan dit project ben begonnen en het eindresultaat hiervan zie je in dit proefschrift. Ik vond het inspirerend om met je samen te werken en hierdoor ben ik meer dan ik had gedacht bezig geweest met schalingsargumenten. Dit heeft mij meer vertrouwen gegeven buiten de experimentele opstellingen, waar ik ongetwijfeld nog veel profijt van ga hebben. Bedankt voor alles.

Alexander Klein en Sten Reijers, you complemented the team we formed at ASML. I always enjoyed working with you, the tea breaks we had at our office and the group dinners! Alexander, your experimental expertise helped me a lot in setting up my experiments. We also had several students in our team for an internship or a graduation project. Yiyuan, Koen, Bo and Martijn, it was a pleasure working with you. It was particularly nice to see the results of the numerical project of Bo come so close to the experimental study of oblique drop impact as shown in chapter 2.

Pascal Sleutel, wij begonnen aan een uitdagend experimenteel onderzoek en wat is hier iets moois uitgekomen! Het was enorm fijn om met je samen te werken, door onze verschillende manieren van werken vulden we elkaar goed aan. Het was leuk om in het lab samen met jou ‘te winnen’ (helaas nadat we soms ‘episch hadden verloren’) en fijn om de vele Skype-gesprekken te hebben om te overleggen. Het heeft uiteindelijk geresulteerd in een publicatie om trots op te zijn.

Riëlle de Ruiter, je bent als postdoc begonnen in onze groep en hebt mij goed geholpen bij mijn experimenten. Op momenten dat ik even vast zat heeft jouw systematische aanpak ervoor gezorgd dat ik weer verder kon. Daarnaast was het voor mij erg fijn dat jij, samen met Robin Koldeweij, het ontwerp van de tinopstelling voor

je rekening hebt genomen. Helaas heb je daar zelf niet mee kunnen werken, maar ik hoop dat de resultaten die er uit gekomen zijn dit een beetje goed maken.

Jacco Snoeijer en Detlef Lohse, als promotoren in Enschede was het fijn om jullie betrokken te hebben bij het project. Ik heb veel geleerd van de meetings waarin we de interpretatie van de metingen bespraken en de manier hoe jullie hiernaar kijken. Ook was het fijn om Michel Riepen betrokken te hebben bij dit project. Met zijn ervaring binnen ASML kon hij vaak de juiste vragen stellen en nieuwe ideeën voor onderzoek aandragen.

I would also like to thank the rest of my promotion committee for reading the entire thesis. Thank you professors Van Swaaij, Venner, Lemay, Tropea and Dahruber.

The experiments done in chapter 4 were not possible without hte input of Rianne de Jong and Song-Chuan Zhao. They helped me in starting the experimental setup and in providing guidelines for the data analysis. Due to your help, the measurements could be done and analysed and the interpretation lead to nice insights in the splashing behavior of impacting drops.

De groepsleiders binnen ASML Research die betrokken zijn geweest bij dit project wil ik ook bedanken: Ramin Badie, Ben de Smet, Joep Pijnenburg en Wim van der Zande. Jullie hebben het project gesteund en geholpen waar nodig en ook de nodige input geleverd, waar ik weer mee verder kon. Ook de mensen binnen ASML Research, met name de Flow and Temperature groep, wil ik bedanken. Van de presentaties tijdens de GWO's heb ik veel opgestoken over de bredere aspecten van de EUV source, maar ook waren de lunchwandelingen altijd gezellig en goed voor een frisse neus. Daarnaast wil ik de Modelshop bedanken voor de hulp, met name Rob de Kater, die vanuit ASML mijn aanspreekpunt was voor problemen met de tinopstelling.

Wanneer ik in Enschede was, was het altijd leuk om de andere POF'ers weer te zien. Bijna elke keer dat ik er kwam, waren er weer nieuwe studenten, PhD's of PostDocs begonnen, wat zorgde voor een goede atmosfeer om te overleggen en ideeën te verzamelen. Ook de lunches aan de lunchtafel bij de vakgroep en de leuke vakgroepuitjes droegen hier aan bij. Daarnaast wil ik ook Joanita Leferink, Bas Benschop, Martin Bos en Gert-Wim Bruggert bedanken. Voor de (technische) ondersteuning zijn jullie onmisbaar, en gelukkig maakt het jullie niets uit dat ASML zo ver weg is! Ook wil ik TCO, en dan met name van Rindert Nauta en Geert Mentink, hier bedanken voor het maken en ondersteunen van de tinopstelling, gebruikt voor de experimenten in hoofdstuk 3. Wanneer ik voor meerdere dagen achtereen naar Enschede moest, kon ik bijna altijd verblijven in mijn "eigen" Bed&Breakfast "*The Ladies of Jazz*". Dank jullie wel Arris, Marieke en Jolan voor mijn tweede thuis in Enschede.

Naast alle collega's met wie ik heb samengewerkt, heb ik buiten het werk ook veel gehad aan vrienden. Allereerst Bram en Rob, bedankt dat jullie aan deze bijzondere dag voor mij willen bijdragen als paranimfen. De steeds terugkerende en inmiddels

befaamde “bestuursetentjes” zijn leuke weekenden om naar uit te kijken en weer gezellig bij te praten met Ellis, Bart, Kay, Rob, Hidde, Robin en Oscar. Als laatste wil ik hier Daphne, Daniëlle, Lizet, Margot en Mirthe, de “Norbertusmeiden”, bedanken voor de altijd gezellige uitjes.

Na mijn verhuizing naar Veldhoven ben ik verder gegaan met hardlopen bij G.V.A.C., de Groot Veldhovense Atletiek Club. Ik ga hier altijd met heel veel plezier naar toe: het lopen is voor mij de ideale manier om te ontspannen en even weg te zijn van alles. De gezelligheid die bij het lopen in een groep hoort bevalt mij ook erg goed: heel erg bedankt “Groep 4”, de marathongroep en alle anderen! Evert, bedankt voor de leuke trainingen - deze hebben mij snel overtuigd om een hele marathon te gaan lopen, maar ook om mijn bijdrage te gaan leveren als assistent-trainer!

Het is natuurlijk cliché, maar als laatste wil ik mijn familie bedanken. Herman, Marian en Simone, maar natuurlijk ook Elly, Frank, Lonneke, Willem en Naomi: heel erg bedankt voor jullie steun de afgelopen vierenhalf jaar. Jullie interesse in mijn werk, en begrip wanneer het even tegen zat, zijn erg belangrijk voor mij geweest. Bart, zonder jou (en je lekker flauwe humor ☺) had ik dit niet kunnen doen. Je hebt me gesteund en geholpen zoveel je kon, dit zal ik nooit vergeten. Ik hou van je ♡!

About the author

Marise Vera Gielen was born on January 18^{th}, 1989 in Eindhoven, The Netherlands. During her first years, she grew up in Dommelen in the municipality of Valkenswaard. At the end of primary school, she and her family moved to Roosendaal. There she graduated from secondary school (*Gymnasium*) at Het Norbertus Lyceum in Roosendaal in 2007. In the same year she started her studies in Applied Physics (*Technische Natuurkunde*) at the University of Twente in Enschede, and she also moved to Enschede. In 2009 she was treasurer of the Study Association 'Arago' and she was a member of several committees during her entire time as a student. Her bachelor assignment was performed at the Physics of Fluids group on "First observations of coherent structures in highly turbulent Taylor Couette flow" in 2011. After this assignment, she started the master program Fluid Physics. Her internship was performed at The Chinese University of Hong Kong in 2012 under supervision of Prof. Xia, which resulted in a report titled "Rayleigh-Bénard convection in a vertical soap film". In July 2013 she received her Master's degree cum laude in the Physics of Fluids group on "Cell detachment by a submerged microjet", supervised by Claas Willem Visser and Chao Sun and resulting in a publication in the "Biophysical Journal". In October 2013 she started her PhD research in the Physics of Fluids group, under supervision of Hanneke Gelderblom, Jacco Snoeijer and Detlef Lohse and in close collaboration with ASML. The results of this research are presented in this thesis.

During her time as a student, Marise worked as teaching assistant for a first year practical course and she helped during days where students about to start their study were visiting. During her PhD she was working-class assistant at the Physics of Fluids group for the first year master course "Advanced Fluid Mechanics" in 2014/2015 and at ASML she taught guest lessons to secondary school students to promote a technical study in general. These experiences led her to continue studying during her PhD to become a teacher at secondary school. In 2016 she finished this study and obtained a degree in teaching (*docent natuurkunde, eerstegraad*) with an internship at Het Sondervick College in Veldhoven and a graduation on "Het werven van meisjes voor technische functies".